Design and Qualification of a Test Fixture to Experimentally Determine Global Tire Force Properties

Rea Kimbrell Cauthen III

Thesis submitted to the faculty of the Virginia Polytechnic Institute and State University
in partial fulfillment of the requirements for the degree of

Master of Science
In
Mechanical Engineering

Robert L. West Jr. Chair
Norman E. Dowling
Saied Taheri

February 21, 2014
Blacksburg, VA

Keywords: tire, suspension, force and moment properties, fixture,
finite elements, Formula SAE

Design and Qualification of a Test Fixture to Experimentally Determine Global Tire Force Properties

Rea Kimbrell Cauthen III

ABSTRACT

The advent of finite element methods has changed the tire industry's design process over the past three decades. Analyses, previously impractical using analytical methods and physically limited by experimental methods, can now be performed using computational methods. This decreases the cost and time associated with bringing a new design to the marketplace; however some physical testing is still required to validate the models.

The design, fabrication, installation, and operation of a tire, suspension, and chassis test fixture (TiSCTeF) is detailed as part of this study. This fixture will support the validation of effective, parametric finite element models currently under development, as well as the design and testing of suspension and chassis components for the Virginia Tech Formula SAE team. The fixture is designed to use the Formula SAE race car as the test platform. Initially, the fixture is capable of performing static load-deflection and free-rolling tire tests. Provision has been made in the design for incremental upgrades to support cornering tests and additional instrumentation.

An initial load-deflection test has proven that the fixture is capable of creating reproducible data sets. Specific recommendations are made concerning the improvement of data quality for future tests.

This study also presents a process for analyzing existing tire cornering data and eliminating anomalies to improve the effectiveness of normalization techniques found in the literature. The process is shown to collapse tire cornering data, which is partially ill-conditioned, onto master curves that consistently display the effect of inclination angle and tire inflation pressure on tire response.

Acknowledgements

Vinny Sorrento, FSAE Team Leader 2013, for access to vehicle and resources
Brice Collamer, FSAE Team Leader 2012, for access to vehicle and resources
Jake McDermott, FSAE 2013 Team, for machining and design support
Xikai Zhao, undergraduate researcher, for treadmill CAD
Herb Roy, Vishay Micro-Measurements, for instrumentation support
Mac McCord, ESM Mechanics Lab, for load frame support
Robin Roston, undergraduate researcher, for testing setup assistance
Mike Lane, undergraduate researcher, for testing setup assistance
Yi Li, graduate researcher, for testing assistance
Sam Wood, for testing assistance
Michael Craft, CVESS Lab Manager, for access to machining equipment
Patrick Summers, EXTREME Lab, for load frame support
Stevie Young, FSAE 2013 Team, for treadmill carbon fiber layup

FSAE TTC and Calspan, for global tire force and moment data

Prof. West, for invaluable knowledge, guidance, and support
Prof. Taheri, for CenTiRe leadership and research opportunity
Prof. Dowling, for deformation fundamentals and project guidance

CenTiRe (Center for Tire Research), an Industry & University Cooperative Research Program (I/UCRC) for tire related research created by Virginia Tech, The University of Akron, the National Science Foundation, and industry sponsors, for providing partial funding for this work under the 'Effective Parametric Finite Element Tire Models for Simplified Transient Response' project

All pictures made by author unless otherwise noted.

Table of Contents

List of Figures

List of Tables

Glossary

CenTiRe	Center for Tire Research
CMM	Coordinate Measuring Machine
DIC	Digital Image Correlation
FEA	Finite Element Analysis
FL	Front Left
FR	Front Right
FSAE	Formula Society of Automotive Engineers
IA	Inclination Angle
I/UCRC	Industry & University Cooperative Research Center
SSE	Sum of Squared Errors
RL	Rear Left
RMSE	Root Mean Square Error
RR	Rear Right
TIRF	Tire Research Facility
TiSCTeF	Tire, Suspension, and Chassis Test Fixture
TR	Treadmill
TTC	Tire Test Consortium

Nomenclature

A	Area
B	Stiffness Factor (Magic Formula)
C	Cornering Stiffness
C	Shape Factor (Magic Formula)
D	Peak Factor (Magic Formula)
E	Curvature Factor (Magic Formula)
E	Young's Modulus
F	Force
$\overline{F}$	Normalized Lateral Force
F_x	Longitudinal Force
F_y	Lateral Force
F_z	Normal Force
F_{Z_Nom}	Nominal Normal Force
FN	Normalized Force for Combined Slip
G	Camber Stiffness
I_x	Area Moment of Inertia
P	Load
P_{cr}	Critical Load
S_h	Horizontal Shift (Magic Formula)
S_v	Vertical Shift (Magic Formula)
SF	Safety Factor
T	Temperature
Z	Vertical Load
f	Frequency
l_e	Effective Column Length
n	Number of Data Points
p	Pressure
r_g	Radius of Gyration
r_i	Internal Radius
r_o	Outer Radius
w	Curve Fit Weight
α	Slip Angle
$\overline{\alpha}$	Normalized Slip Angle
β	Normalized Slip and Inclination Angle
γ	Inclination Angle
$\overline{\gamma}$	Normalized Inclination Angle
ε	Strain
μ	Coefficient of Friction
$\mu\varepsilon$	Microstrain
σ	Stress
σ_Y	Yield Stress

1. Introduction

This chapter provides an overview of the current state of pneumatic tire testing, the developed research concept, and research objectives. The chapter concludes with the definition of scope for this thesis and its structure.

1.1. Overview

Tires are complex structures that provide the interface between a vehicle and the road surface that it is traveling over. The area of the tire that is in contact with the road surface (contact patch) must support the weight of the vehicle and produce the friction forces necessary to move the vehicle around corners and to speed up and slow the vehicle. Pneumatic tires are of particular interest, as they also act as a dynamic system to isolate road vibrations. As a result, pneumatic tires dominate the passenger vehicle, motorsport, and commercial markets.

Tire force and moment data is required to perform analytical vehicle dynamics simulations. These simulations are used to quantify and objectively evaluate the stability, handling, and ride-comfort of a vehicle. Establishing tire force and moment relationships is not a trivial task. This data is dependent on non-linear relationships that vary based on speed, temperature, geometry, boundary conditions, and construction of the tire. The resources and time required to fully characterize the behavior of a tire over the expected range of conditions are quite expensive [1]. According to Radt and Glemming [2], approximately 500 tests would be required to fully characterize a typical tire.

Finite element analysis (FEA) codes became increasingly popular in the tire industry beginning in the 1980s. Increased computational efficiency and improved codes allowed engineers to begin analyzing stresses in the tire structure [1]. More recently, FEA has been incorporated into the product development cycle. This has served to reduce the number of physical tests and costs required to design a tire. According to Gall, et al. [3], "Examples for some of the computed values are deformations due to inflation, stresses due to inflation, the load-deflection curve, footprint shape, global forces and moments, natural frequencies, etc." Recently parameterized finite-element models have been developed to explore the effects of material and geometric parameters on the dynamic response of the tire. Despite advances in computational power, these types of models can still be computationally expensive [4].

Need exists to further improve the quality and fidelity of these nonlinear finite element models in the public domain. Due to the competitive nature of any industry, the models developed by tire manufacturers are proprietary. Additional users of tires, particularly small racing teams, manufacturers of off-road vehicles, and trailers will benefit from the advance of tire modeling in the public domain. As the accuracy and computational efficiency of these models improve, the smaller industries will be able to save both time and resources by continuing to utilize more virtual testing. This will not entirely eliminate physical testing, however, as these models must be validated using experimental data to ensure their accuracy.

1.2. Research Concept

The goal of this project is to create a finite element tire model that captures the dominant mechanics of the tire for the purposes of vehicle dynamics and durability studies and is efficient in terms of model preparation and run-times. The tire models will be parameterized so that adjustments to the geometry/construction of the model are easily updated. Results from these models are intended to support operational analysis of the tire design, for use in vehicle dynamics and load transfer models, and durability studies for suspension and chassis components. Tire users in smaller industries and potentially vehicle manufacturers will benefit from the results of these models.

In addition, manufacturers of agricultural, turf, and off-road equipment will benefit, as tires sold for these applications are typically not accompanied with representative global force and moment data. Dynamic simulations for these vehicles cannot be conducted without first acquiring expensive tire force and moment data. This project intends to outline a method to obtain the required geometric and material parameters from a tire to create a representative finite element model. Global tire force and moment data can then be determined through a validated simulation.

The test vehicle platform for this project is the 2012 Virginia Tech Formula SAE race car. This car runs the Hoosier LC0 tire. Material properties for this tire will be determined from experimental data using specimens extracted from a cured tire. Experimental validation of the model will require the fabrication of a test fixture to roll the tire under various loading scenarios. Digital image correlation (DIC) optical techniques will be used to capture the full-field deformations and strains of the tire on the test fixture. Since performing durability studies on suspension members is one of the project outcomes, it is necessary that the test platform accommodate the entire FSAE (Formula Society of Automotive Engineers) race car.

This thesis presents a concept solution and testing platform for validating the models along with supporting the development of suspension and chassis models for the Virginia Tech FSAE team. Inspiration for the concept solution comes from an 8-post shaker designed for suspension tuning, durability, and acoustic testing. This type of machine uses four hydraulic rams to independently actuate each wheel of the vehicle, while 4 additional actuators are used to independently push or pull the sprung mass, simulating varying aerodynamic and inertial loads that the vehicle experiences on the track or road.

The solution concept presented in Figure 1 utilizes four independent actuators to control the vertical loading of the vehicle. The Internal Combustion Laboratory in Randolph Hall on the campus of Virginia Tech was chosen as the facility to house this test platform because it has a slotted steel base for use as anchoring points. Due to the limited size of the steel base, the floor and walls of the laboratory must be used as additional anchoring points.

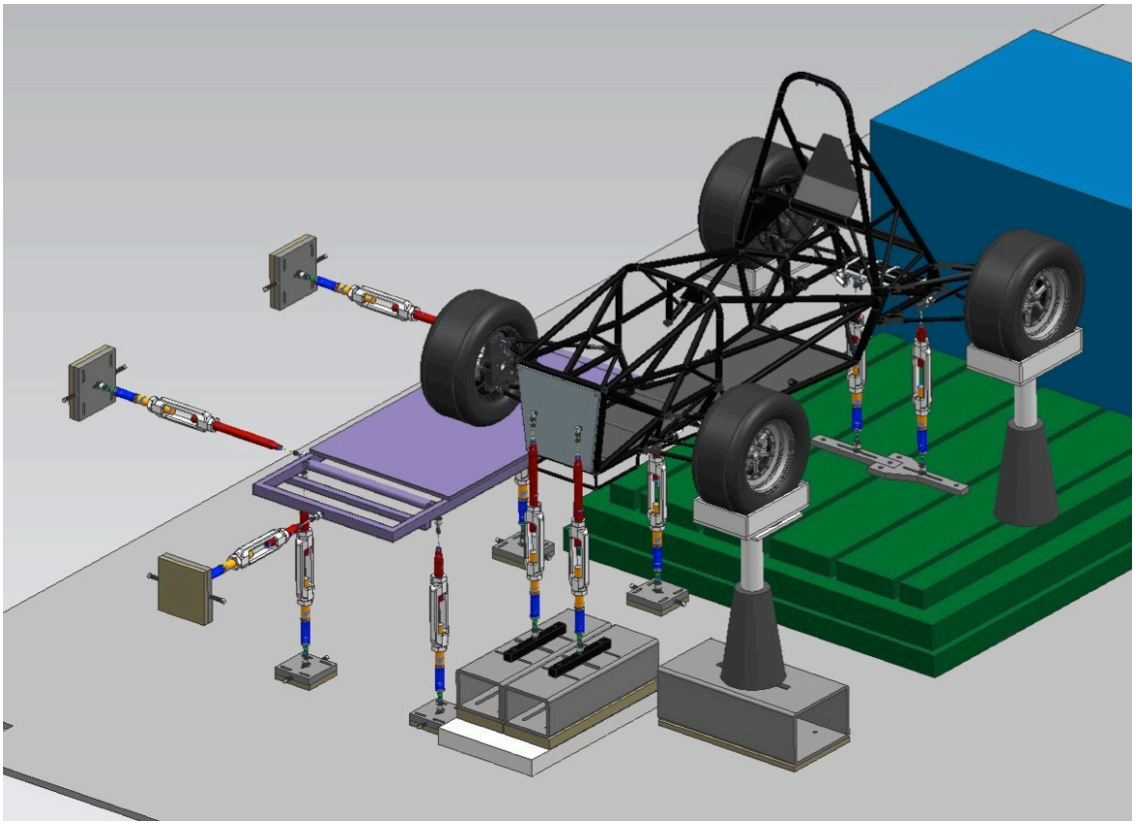

Figure 1: CAD Model of Test Fixture

A basic treadmill is used as the conveyor system to roll the right-front tire. The treadmill provides a flat surface on which to roll the tire, and is capable of rolling the tire at low speeds without any modifications. The treadmill is supported by seven support columns, configured to create a kinematically stable structure. Each actuator and support column includes a gage section where strain gages are mounted to measure the axial loads. An off-the-shelf load cell design was integrated into the actuator and support column designs as a means of calibration for the strain gages. The remaining three corners of the vehicle are supported and constrained to prevent vehicle movement. Vertical (normal) loads are also measured at the untested corners for load-distribution verification purposes.

1.3. Research Objectives

This section presents the research objectives that the research concept seeks to meet. The work done here is pursuant to the research concept outlined in the previous section.

1.3.1. Compare Experimental Data With Tire Test Consortium Data

Some established cornering load data exists for the tire used in this test platform as part of the FSAE Tire Test Consortium (TTC). The intent of studying the TTC tire data is to develop a process for analyzing cornering data, utilize the existing data for comparison purposes with data obtained from the concept fixture presented herein, understand the appropriateness of using the Calspan test machine for these smaller tires, and to gain insight into the limitations of these types of tests.

It is not expected that data from the Virginia Tech test fixture will identically match the data from the TTC. The machines will certainly have different friction coefficients, test speed ranges, and instrumentation. However, Pottinger et al. [6] has suggested that a simple correlation can be determined to transform data sets between two flat surface machines. It is also not expected that the Virginia Tech test fixture will have the same capabilities as a multi-million dollar commercial test machine. However, the test fixture should be able to provide precise and accurate data sets for static and low speed quasi-static tests under loads appropriate for FSAE-type tires.

1.3.2. Create a Test Fixture to Roll the Tire

The primary goal of this research is to design, fabricate, install, and calibrate the test fixture to roll a tire. This platform, coupled with the DIC system, will be capable of determining the deformation and strain field of the tire under static and dynamic conditions. This information can be used to reconcile and validate the developed finite element model for the tire. The fixture must be able to apply known normal loads to the tire, and support free rolling lateral dynamics. The test fixture should be extendable where possible, so that future upgrades can increase the capability of the fixture.

1.3.3. Measure Wheel Center Loads

The test fixture should also be capable of measuring the global loads created in the contact patch of the tire. This information will be used to validate models that determine lateral and drive/braking force characteristics. This data will be normalized as appropriate and described in later sections.

Quantification of these loads is also important to perform durability studies for suspension members. The need for such a test fixture was outlined by Borg [5] as a way to validate a finite element model for suspension arms. Once a relationship has been determined between the wheel center loads and the control arm strains, a racing team can use strain gage data from the control arms during testing to accurately predict the observed wheel center loads. Then, the observed wheel center loads can be compared with the established tire characteristics to determine if the suspension setup is operating as designed and best utilizing the available force capability in the tire [5].

1.4. Research Scope

The research scope presented in this section provides the limits for this thesis. The scope is defined in reference to the research objectives of Section 1.3.

1.4.1. Analyze Tire Test Consortium Data

Data for the cornering tests performed by Calspan as part of the TTC will be analyzed and normalized in this work. The traction/braking and combined cornering tests conducted by the TTC are not considered. Static and dynamic spring rates conducted by the TTC are also not considered. Only positive slip angle sweeps are analyzed due to the large volume of data provided by the TTC.

1.4.2. Create a Test Fixture to Roll the Tire

Base design of the TiSCTeF (Tire, Suspension, and Chassis Test Fixture) and its associated instrumentation is included in the scope of this thesis. The fixture design supports static load-deflection tests and dynamic rolling tests with no induced slip angle. The design is limited to speeds of 10 mph and static loads of 450 lbf per corner. Additional design will be required to increase the fixture load capacity, increase the maximum wheel speed, or to accommodate cornering or traction/braking tests. Fabrication, installation, and calibration of the base fixture have been completed at the time of publication. Integration and use of the DIC system will be conducted under a separate study.

1.4.3. Measure Load-Deflection Relationships

Testing using the fixture is limited to static load-deflection studies for this thesis. The application method for loading the chassis has not been completed at the time of publication. Weights placed in the chassis were used as load for the load-deflection tests. Comparison to load-deflection tests carried out on a system level and load-deflection finite element models will be conducted under a separate study.

1.5. Thesis Structure

Chapter 2 provides relevant background information regarding tire mechanics, methods for tire development, equipment used to test tires, and the Formula SAE car platform. Chapter 3 contains the processing and normalization of the TTC cornering data for the Hoosier LC0 tire. Chapter 4 contains the TiSCTeF design requirements, subassembly design, and instrumentation selection. Chapter 5 describes the calibration of the TiSCTeF instrumented sections. Chapter 6 contains the results from the load-deflection test of the Hoosier LC0 and 2012 Virginia Tech FSAE race car on the TiSCTeF. Chapter 7 includes conclusions and recommendations related to processing of cornering data and use of the TiSCTeF.

1.5.1. Use of Non-SI Units

Due to the history and nature of the tire industry, publications in the References chapter of this thesis use U.S. customary units of measure. Information in this thesis will be presented in U.S. Customary units to align with the norms of the tire industry. In an effort to support the ASME and SAE goals of utilizing SI units of measure, a list of values commonly used in this thesis and their SI equivalents are provided in Table 1.

Table 1: SI Equivalents for Commonly Used Values

U.S. Customary Units	SI Units
8 psi	55.16 kPa
10 psi	68.95 kPa
12 psi	82.74 kPa
14 psi	96.53 kPa
50 lbf	222.4 N
100 lbf	444.8 N
150 lbf	667.2 N
200 lbf	889.6 N
250 lbf	1112 N
450 lbf	2002 N
1 deg	0.01745 rad
2 deg	0.03491 rad
3 deg	0.05236 rad
4 deg	0.06981 rad
15 deg	0.2618 rad
120 °F	48.89 °C

1.5.2. Use of Tire Test Consortium Data

The membership terms of the FSAE TTC do not allow the data to be posted for public use. Only examples that are representative of observed trends will be provided in this document to comply with the TTC proprietary agreement.

Information about joining the TTC can be found at
http://www.millikenresearch.com/fsaettc.html

2. Background

The intent of this chapter is to orient the reader to the relevant tire mechanics and tire development history to understand the motivation for this study. Additional information about tire construction, manufacturing, vehicle dynamics, tire vibration, tire wear, and other characteristics can be found in the listed References. It should be noted that all figures presented in this chapter are notional or nominal and represent the commonly observed tire response.

2.1. Tire Mechanics

The universal coordinate system used to describe a vehicle's components and motions of the vehicle is shown in Figure 2. This is a fixed coordinate system that moves with the vehicle so that its orientation does not change relative to the orientation of the vehicle. Note that side velocity is also commonly referred to as 'lateral' velocity.

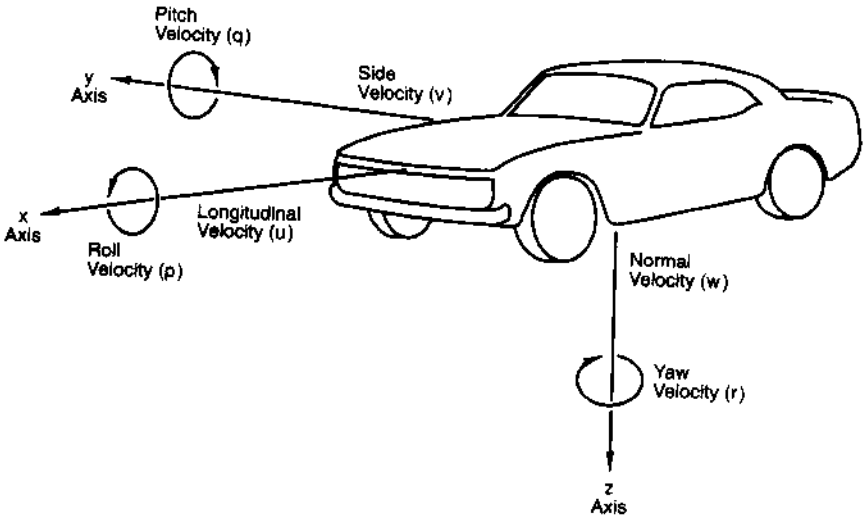

Figure 2: Vehicle Coordinate System. Milliken, W. F., and Milliken, D. L., 1995, "Race Car Vehicle Dynamics," Society of Automotive Engineers, Warrendale, Pa. Used with permission from SAE publication *Race Car Vehicle Dynamics* by Milliken and Milliken, Figure 4.2

The steering wheels on a vehicle are designed to rotate relative to a defined (kingpin) axis. It is important to define some additional terms to describe the position of the tires relative to the car as the driver rotates the steering wheel. Figure 3 displays the coordinate system for a tire. Important parameters relative to this study include lateral force, normal force, inclination angle, and slip angle. Lateral force describes the force generated by the tire in the y-direction that is created due to a finite slip angle. Slip angle is the angle between the heading of the wheel and the direction of wheel travel. A slip angle is created due to driver input into the steering system. Normal force is the load on the tire in the z-direction due to the weight of the sprung and unsprung mass, inertial forces, aerodynamic loads, and load transfer due to roll or pitch of the sprung mass during cornering, braking, or traction. The inclination angle is the angle between the wheel plane and the x-z plane. The inclination angle is allowed to change during vehicle operation, and load transfer causes the change.

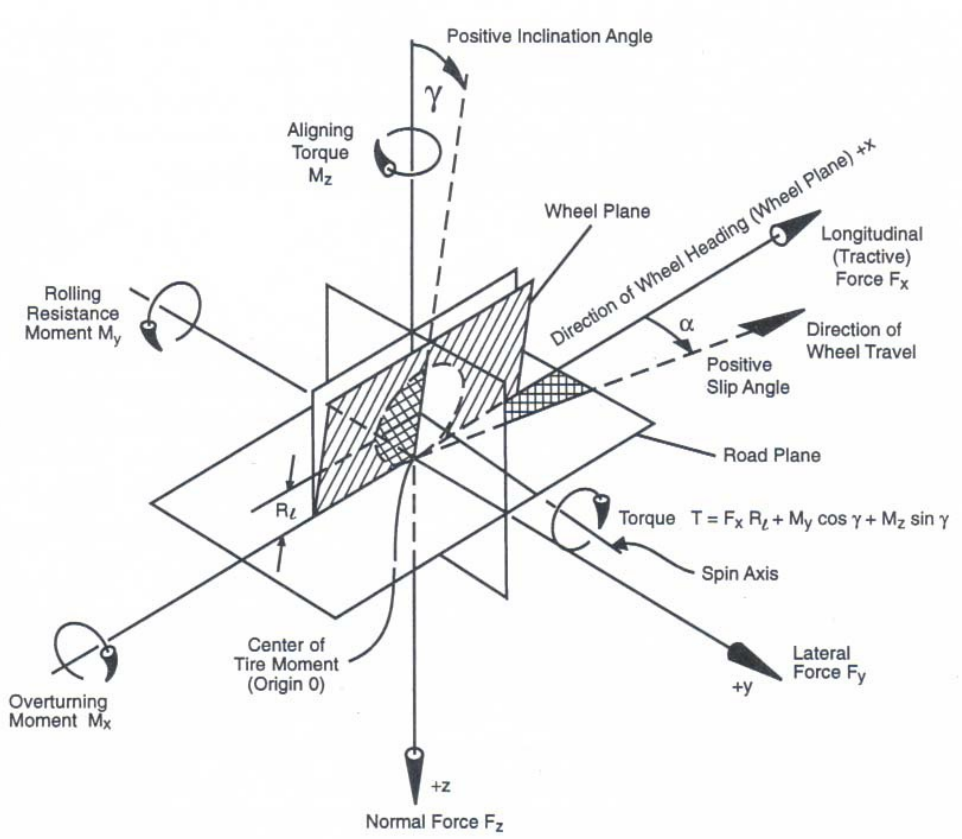

Figure 3: Tire Coordinate System and Nomenclature [7] Reprinted with permission from SAE publication *Race Car Vehicle Dynamics* by Milliken and Milliken, Figure 2.23

Tires under normal operation exhibit a state behavior, where the output can be reliably predicted for a given set of input conditions. The lateral force generated in the contact patch of the tire is defined by the slip angle, inclination angle, and normal load on the tire. Figure 4 shows the typical lateral force behavior of a tire. At low slip angles, a linear relationship is observed between slip angle and lateral force. As the slip angle increases, the curve becomes nonlinear and a maximum lateral force is frequently observed. Note that although increasing the normal load at a given slip angle increases the lateral force generated by the tire, the increase in lateral load is not proportional to the change in normal load. Figure 5 is used to demonstrate this phenomenon, where the data from Figure 4 is plotted in a different configuration to better observe this nonlinearity. This typical tire exhibits an asymptotic approach to a linear relationship at increasing slip angles. Note that the data in both of these figures is specific to an inflation pressure of 31 psi.

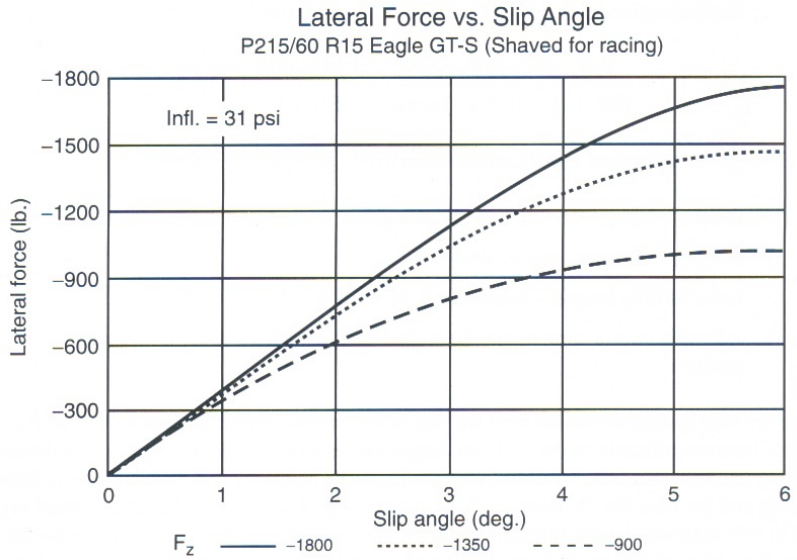

Figure 4: Typical Tire Friction Curves [7] Reprinted with permission from SAE publication *Race Car Vehicle Dynamics* by Milliken and Milliken, Figure 2.42

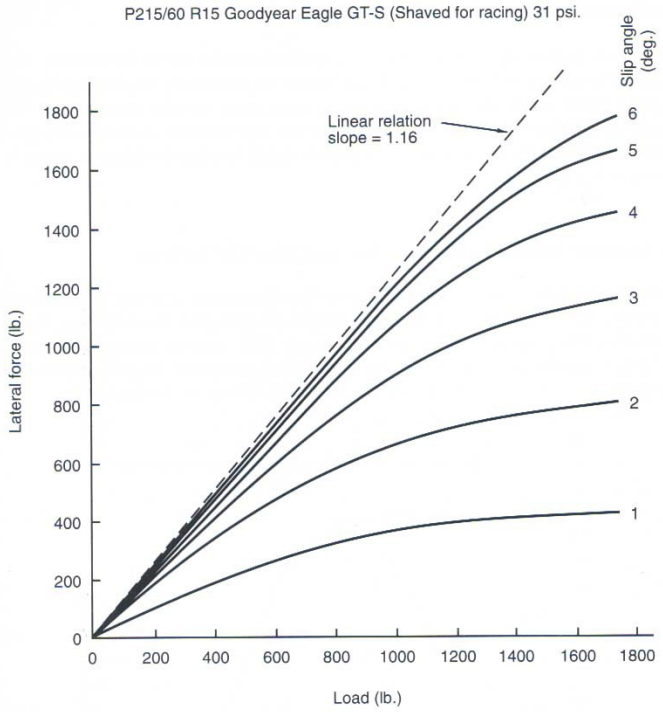

Figure 5: Typical Tire Friction Curves Continued [7] Reprinted with permission from SAE publication *Race Car Vehicle Dynamics* by Milliken and Milliken, Figure 2.10

Figure 6 demonstrates the effect of inclination angle on a lateral force relationship. A finite camber creates a lateral force in the tire without an induced slip angle and affects the end behavior of the lateral force and slip angle relationship.

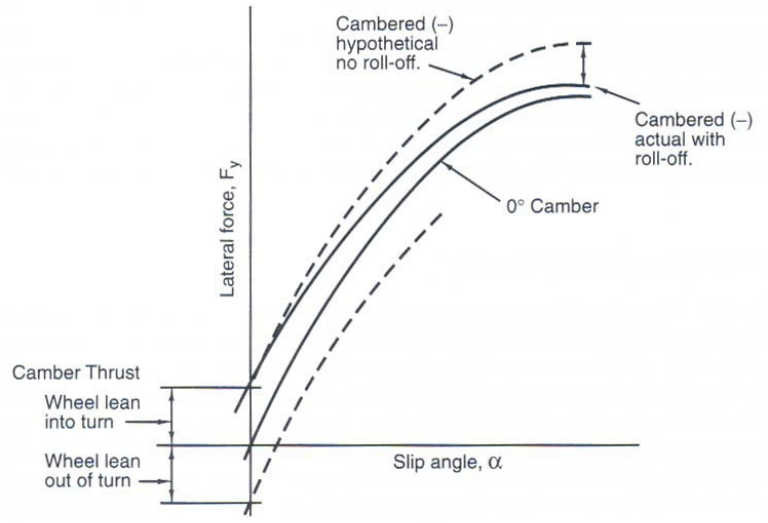

Figure 6: Camber Effect on Lateral Force [7] Reprinted with permission from SAE publication *Race Car Vehicle Dynamics* by Milliken and Milliken, Figure 2.24

A universal, semi-empirical relationship exists to represent the tire lateral force behavior, called the 'Magic Formula.' This relationship was developed to simplify the input to vehicle dynamics simulations, where a table lookup and interpolation routine would have been needed. The Magic Formula is shown in Eq. (1), where F_y is the lateral force, α is the slip angle, B is the stiffness factor, C is the shape factor, D is the peak factor, E is the curvature factor, S_h is the horizontal shift, and S_v is the vertical shift [8].

$$F_y = D\sin(C\arctan\{B(\alpha + S_h) - E[B(\alpha + S_h) - \arctan(B\{\alpha + S_h\})]\}) + S_v \quad \textbf{(1)}$$

The product BCD equals the cornering stiffness at zero slip. The Magic Formula has been validated to accurately describe the steady-state force and moment behavior for traction/braking, cornering, and combined traction and cornering conditions for representative data sets [8]

2.2. Tire Development

Tire design engineers must evaluate hundreds of design characteristics including the inflated shape, bead fitment, vertical stiffness, contact patch size, internal stresses and strains, rolling resistance, vibration characteristics, cornering characteristics, and impact analyses. Although very few of these characteristics could be evaluated when the pneumatic tire gained popularity in the early 20th century, techniques have evolved and are still improving to better understand how the tire structure operates [1]. This section will outline some of the traditional analysis and experimental methods used in tire design and the advancements achieved though the use of finite element analyses.

2.2.1. Analytical Methods

Initially, classical mechanics approaches were used to determine the inflated shape of bias-ply tires and properly design the curing mold to achieve this shape. These approaches also included an estimate of the force distribution in the cord sections. Due to the construction differences, no classical mechanics approach currently exists to determine the inflated shape and cord load distribution in radial-ply tires. Through simplifications, the cord tension at the centerline of the tire can be estimated. Radial tires also contain cords in the sidewall sections of the tire. The cord tensions in this region can be estimated if the curvature of the sidewall is known, however this quantity is not directly measureable. The load in the bead section due to the interference fit with the rim can be estimated if the bundle cord tensions are known, however published data for estimating cord tensions in the bead bundle does not exist [1].

Micromechanical theories for composite laminates were developed to capture the orthotropic behavior of cord-rubber layups. These theories provide the 3D stress-strain relationships for infinitesimal composite elements and retain the mechanics specific to both the cord and rubber. Due to the complex nature of these relationships, simulation beyond the elemental scale is not practical. Macromechanical theories were developed to simplify the relationships by "smearing" or creating an effective set of representative properties to describe the mechanical behavior of the combined cord and rubber. Macromechanical theories can be reasonably extended to model simple geometries, such as plates or beams. Finite element analyses, however, are still required for modeling of complex structures such as tires [1].

2.2.2. Experimental Methods

Since analytical methods could not provide significant insight into radial designs (and finite element methods were still being developed at the time), tire designers focused on developing experimental methods to better understand tire behavior. Interest was focused on understanding strain patterns in the rubber regions, cord loads, pressures at the interference fit between the bead and the rim, and contact patch geometry, forces and displacements [1].

Knowledge of the strains experienced by the tire is important to predict and improve the fatigue life of the rubber compound. From an experimental approach, it is important to select a strain gage that will accurately capture local strains rather then the average strain over a larger area. If the strain gradients are high, smaller gages are required. Unfortunately, surface sections of the rubber region experience a very large strain range, and larger strain ranges require larger gages. Thus, an inherent conflict of design goals exists to create a gage for this application [1].

Measurements of cord loads require a test assembly be built into the tire and cured. Two types of test assemblies were used: billets that attached to a cord and cylinders that fit around a cord. Strain gages attached to the test assemblies were used to determine the cord loads [1]. Performing this type of measurement requires considerable set-up and only provides information at one discrete location.

Specialized pressure transducers were developed to measure the pressure at the bead and rim interface. The transducer is mounted on the outside of the rim and sits flush with the inside surface of the rim where the bead is seated [1].

Several methods were developed to capture the contact path geometry. Initial methods included loading the tire statically and using carbon paper and ink or paint to indicate the contact locations. The contact patch geometry changes under dynamic conditions however, and glass plate visualization was developed to capture this information. The tire is rolled over a glass plate at low speeds, and imaging software is used to calculate the footprint geometry.

A variety of test machines have been developed to quantify local contact patch forces. Quantifying this information is important to understanding wear and cornering characteristics of the tire design. Pressure sensitive film, where the image intensity is related to the normal force applied to the film, provides high-resolution data for the normal force distribution in the footprint. The film is applied to the road surface, and imaging equipment and software calculate the normal force distribution under static or dynamic conditions. Note that this method is not capable of measuring shear forces in the footprint. Another approach involves one or multiple load cells designed to measure surface stresses. The transducers were installed level with a test surface, and the tire would then be rolled over the test surface multiple times to capture the force profile across the entire contact patch. Careful set up is required to ensure the accuracy of the test results for this type of test. If the transducer is not installed flush with the road surface, it will either over- or under-support the tread above the transducer, leading to inaccurate measurements. The transducer must also be installed with a small insulation gap to prevent a parallel load path around the transducer. This gap must be kept clean and clear to ensure accurate measurements. The transducers themselves must minimize coupling between the measurement channels and be designed to eliminate an applied moment. Finally, data from transducers that are partially covered by a tread element must be rejected. Thus, the measurement machine must accurately control the wheel location relative to the transducers in order to know the location in the footprint where data is being collected. These types of tests were usually limited to low speeds, costly due to the set-up time for each test, and many of the transducers were limited to a single use [1].

Displacement in the contact patch is related to the slip and subsequent shear forces that are generated in the tire. This measurement provides information about the wear characteristic of the tire, but is not usually performed due to experimental and cost limitations. Initial tests were conducted using instrumented needles that were embedded in the road surface. This approach faces many of the same challenges as the embedded transducers previously described. The gap around the needle must be small to ensure that the footprint mechanics are unchanged, however this limits the displacement range of the needle. Optical methods were later developed to measure slip displacements by rolling the tire over a glass plate. Motion analysis, where optical targets are tracked using a camera and appropriate imaging software, works well under a variety of operating conditions. Line scan analysis uses a camera and a laser line to track the edges of the tread blocks as they pass through the contact patch. Both of these methods are limited to modest speeds [1].

2.2.3. Finite Element Methods

The traditional tire design processes started with an initial tread design and construction of a prototype. After extensive testing, improvements were identified, and new molds were manufactured to create updated prototypes. This cycle would typically be repeated two to three

times until the tire met the desired specifications. This process required multiple years of development time and a large investment of capital [9].

Due to the complexity of the tire structure and the limitations of the analytical and experimental methods available for tire analysis, finite element analyses were gradually adopted to solve design problems that were previously unanswerable. Tire companies initially created tailored in-house codes to visualize the stress/strain distributions and solve durability problems that were identified during testing [10].

More recently, however, structural finite element analyses have been incorporated earlier into the design process before prototyping. Using selected design parameters, constraints, design goals, and optimization routines, an optimized design is created from the beginning of the design process. As a result, tire shapes have changed significantly in pursuit of a longer fatigue life, improved handling and stability, and improved traction in wet/snow and off-road conditions. On-road testing has confirmed that the optimized designs perform as intended [10]. Incorporation of virtual testing and optimization into the design process is not meant to completely replace physical testing. According to Nokian Tyres [9], "we will just be able to provide more information for designers, make better trials for physical testing and therefore provide safer tires with improved performance for consumers needs." Currently, it is common for a tire company to send hundreds of finite element runs to their computation platform per week.

The tire profile and material model must be given as input to the finite element code that is chosen. Due to the confidential nature of a competitive marketplace, tire manufacturers are typically reluctant to provide proprietary information about the tire geometry and mechanical properties of the individual compounds and components. As a result, tire modeling in the public domain requires that these parameters be extracted from appropriate tire samples. A radial section cut from a tire can be used to determine the profile geometry. Olatunbosun and Bolarinwa [4] also used a Coordinate Measuring Machine (CMM) to measure the uninflated profile of the tire mounted on a rim.

The material model used must capture the dominant mechanics that are relevant to the study being conducted. Rubber is a highly non-linear material that exhibits large strains (hyperelastic), temperature dependence, viscoelasticity, hysteresis, and damage (Mullins and Payne effects). When cords and belts are introduced to the structure, these composite areas of the structure become orthotropic [1]. Laminated composites or rebar reinforcement elements are used to represent an effective orthotropic layer for modeling purposes.

Nakajima predicts that tire finite element analyses in the future will be increasingly applied to reduce rolling resistance, noise and wear. Also, as computational power and the capability to handle more complex phenomena continue to increase, the mechanics will be able to be simulated on a micro/nano scale in addition to the macro scale [10].

2.3. Tire Testing Equipment

This section describes the basic operational design of selected tire testing equipment as related to the objectives of this project. Included are global tire force and moment machines and digital image correlation systems.

2.3.1. Global Tire Force and Moment Machines

Current testing methods and equipment for the purposes of tire modeling are described in this section. Indoor testing systems include the drum-type configuration shown in Figure 7 and the flat surface configuration shown in Figure 8. The wheel rotates on a semi-static fixture while the drum or belt moves. The drum-type configuration is the simplest to implement, as the steel drum directly supports the loads applied by the tire. The drum is driven directly by an electric motor. A disadvantage of the drum-type configuration is distortion of the contact patch due to the curvature of the drum. When the tire rotates along the outside of the drum, the contact patch area is reduced relative to a flat surface, and the contact patch area is increased when the tire rotates along the inside of the drum. Changes in the contact patch affect the stress distribution and force capability of the tire. Larger drums reduce the distortion in the contact patch, however there is a practical limit to the drum size and driving motor. Pottinger [6] suggests that an 84-foot diameter drum would be required to reproduce a footprint with only 1% error in footprint length.

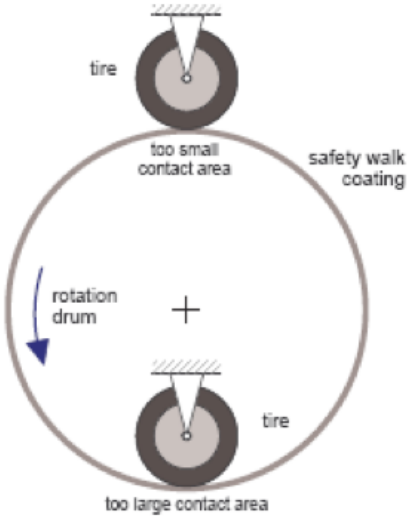

Figure 7: Drum-type Test Configuration. Taheri, S., 2012, "Tire Modeling," ME 5674 Lecture, Virginia Tech, Blacksburg, VA. Used with permission from S. Taheri

The flat surface system attempts to more accurately approximate the interface between the tire and the road surface. A steel belt is used as the road surface, and large diameter drums rotate the belt. This type of system requires a hydrodynamic or pneumatic bearing to reduce the friction between the belt and the vertical load support. An emery-cloth like coating on the steel belt or drum increases the friction coefficient to better approximate that of a road surface. The relatively constant friction coefficient of these machines is an advantage over on-road testing, where the road surface cannot be controlled. A well-known type of commercially available flat surface machine is the MTS Flat-Trac® Tire Testing System.

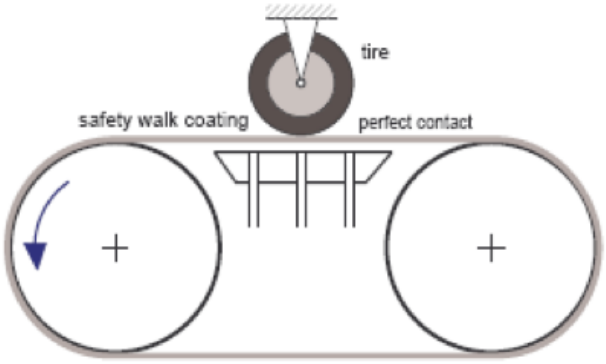

Figure 8: Flat Surface Test Configuration [11], reprinted with permission from S. Taheri

As described by Pottinger [6], the same tire under the same measurement conditions and speed behaves differently on the drum and flat surface machines. Data collected on the Calspan machines does not suggest that a universal correlation exists between the drum and flat surface data. As a result, the authors suggest that curved surface experimental data has a limited usefulness for vehicle handling modeling [6].

A test trailer shown in Figure 9 can be used for dynamic on-road testing. The test trailer is pulled behind a tow vehicle. A compensation tire is steered at an equal but opposite angle as the test tire to balance the lateral forces exerted on the trailer. The test speed in this configuration is practically limited by the tow vehicle and the available road space. A force hub is typically used in all three presented configurations to measure the generated tire forces and moments.

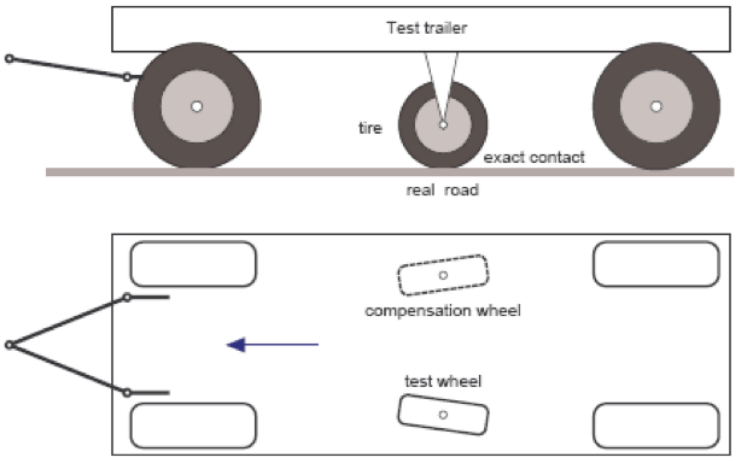

Figure 9: Trailer Type Dynamic Test Configuration [11], reprinted with permission from S. Taheri

Tire speed also has an influence on the force and moment properties of a tire. Pottinger [6] investigated the effect of tire speed on vehicle handling simulation results. Although the response times were similar using tire data from varying speeds, the steady state values for yaw velocity and lateral acceleration are highly speed dependent. Thus, the speed dependency of tire data should be considered when studying transient responses [6].

The fixture designed in this study is a flat surface type system due to the inherent advantage of a flat system to reproduce the on-road footprint of the tire. The trailer type configuration was considered, but the hub for the available trailer could not accommodate the selected tire.

2.3.2. Digital Image Correlation

Moser, et al. [12] has shown how digital image correlation (DIC) techniques can be successfully applied to measure surface displacements and strains on tires. DIC is a robust and repeatable noncontact method for measuring three-dimensional deformations of an object. The area of interest is randomly speckled with a paint to provide reference markers for the system. Two cameras, placed a known distance apart, capture images of the area of interest while the object is deformed. Using the triangulation principle, the deformation shapes and subsequent surface strains are calculated from the captured images [12]. Considering the historical experimental methods for tire development described in Section 2.2.2, this technique is currently the most practical method for determining full-field, dynamic tire strain measurements.

After validating their DIC system, Moser, et al. [12] sought to prove the versatility of the DIC system as a tool for tire development. Sidewall strains in a passenger tire were measured on a static fixture, biaxial loading data from a tire specimen was measured to supplement uniaxial loading data in a material model, strain distributions in the sidewall of agricultural tires were measured to show the variations due to tread patterns, and sidewall deformations in a passenger tire were measured at high speed on a rolling drum to capture a standing wave deformation in the tire. Where appropriate, the results were used to validate and improve finite element models [12].

A DIC system will be integrated as part of the test platform developed herein. An important consideration when designing a test using a DIC is that the cameras should be isolated from the test fixture. Varying loading scenarios could cause camera movement, resulting in erroneous deformation calculations [12].

2.4. Formula Car Platform

The test platform used for these purposes is the 2012 Formula SAE car. Each year SAE International hosts student design competitions, open to universities across the world, to design, build, and race small Formula-style (open-wheeled, one seat) race cars. These vehicles are typically capable of speeds up to 70 mph and 2g's of lateral acceleration. Dynamic events at the competition include a skid pad, acceleration, autocross, efficiency, and endurance events. Virginia Tech has participated in this competition since 1988.

The 2012 FSAE team chose to design their vehicle around the Hoosier LC0 tire mounted on 7"-wide wheels. This tire offers reduced cost, size, and rolling resistance, increased peak lateral acceleration, and a lower operating temperature compared to tires selected in previous years [13]. The 2012 car fitted with the Hoosier LC0 tires is shown in Figure 10.

Figure 10: 2012 Virginia Tech FSAE Race Car, picture courtesy of VT Motorsports

The FSAE race car was chosen as the platform for testing because of its reduced size and complexity. The vehicle and tires are smaller than passenger vehicles and tires, and are thus subject to lower loads. As a result, the size and cost of the test fixture and associated instrumentation should be more cost effective. Since the Hoosier tire is meant for racing purposes, it does not have any tread elements (slick). This simplifies the modeling process during this proof-of-concept stage as modeling tread elements will increase complexity and run times for the models.

2.5. FSAE Tire Test Consortium

The FSAE Tire Test Consortium was established in 2005 to provide FSAE teams with high-fidelity tire data to aid in tire selection and suspension/chassis design. The consortium operates on cost sharing, where participating teams are given access to the data. Five rounds of testing have been completed to date; the current most popular tire brands and sizes are selected by the consortium for testing when enough funds are available.

The TTC contracted with the Calspan Tire Research Facility (TIRF) to collect the tire data. The test machine at TIRF was created in the early 1970's and has been used for both major motorsport industries and passenger vehicle applications. The TIRF machine rolls the tire on a flat belt and can vary the normal load, road surface velocity, lateral slip angle, inclination angle, and inflation pressure. A test matrix of testing conditions was created based on the expected operation conditions of the FSAE race cars. The tests performed include static and dynamic spring rate tests, dynamic lateral sweeps, drive/braking sweeps, and appropriate warm-up and break-in procedures [14].

2.6. Summary

Finite element analyses are becoming increasingly more integral to the design and development of tires. Traditional analytical methods proved limited in their ability to model the tire as a system, while traditional experimental methods proved limited in their ability to measure and validate the tire micromechanics. This project will utilize proven global force measurement techniques in conjunction with a DIC system to ensure that the mechanics of the model are captured on both an elemental and global scale. A validated model will provide the basis for model optimization, where the dominant mechanics of the tire are captured and the model is efficient in terms of model preparation and run-times.

Both the TIRF fixture for the TTC data and the fixture designed for this project are the flat-surface type global force and moment machine due to the inherent advantages of flat surface testing. Experimentally measured wheel center loads are also valuable to the FSAE team to validate suspension component design and modeling, as well as establishing a correlation between control arm loads and wheel center loads.

3. Analysis of Tire Cornering Data

The intent of this chapter is present the methods used to analyze and normalize tire cornering data. The limitations associated with controlling the operating conditions during tire testing are also explored. In addition to providing normalized results, the method developed here can be used to analyze additional purchased data sets or data collected from the test fixture developed in Chapter 4.

The actual tire data analyzed cannot be disclosed due to a membership proprietary agreement with the TTC. The actual curves have been replaced with normalized representative curves for general publication.

3.1. Processing of Raw Data

Hysteresis loops inherently exist in the cornering behavior of tires. As shown in Figure 11, the positive and negative sweeps can be distinctly different curves that form a closed hysteresis loop. The magnitude of the disparity between these two curves is likely related to the slip angle sweep-rate used during testing and the rotational velocity of the tire. Based on a best practice recommended by an industry representative from Michelin, positive and negative sweeps must be separated in order to perform any further analysis. For the purposes of this study, only the data subsets including positive sweeps are further analyzed. Also, all tire data for this study will be plotted in quadrants I and III (relative to the lateral friction coefficient vs. slip angle plots) for clarity.

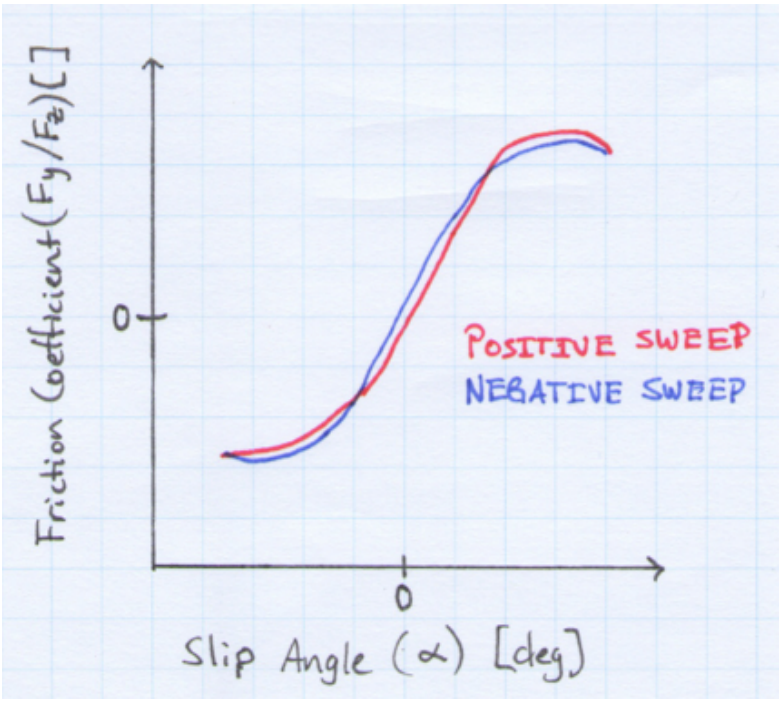

Figure 11: Variation Due to Sweep Direction

Magic Formula curve fits are required for data sets in order to obtain the cornering stiffnesses and peak friction coefficients needed in the normalization formulas. The MATLAB Curve Fit toolbox can be used to calculate the relevant Magic Formula coefficients. However, the quality

of such a curve fit is dependent on the consistency of the normal load control during the test. Figure 12 shows a representative test compared to its nominal normal load. The observed normal load is only close to nominal at the two extreme slip angles and at zero slip. Approximately 10% maximum error is observed in this example.

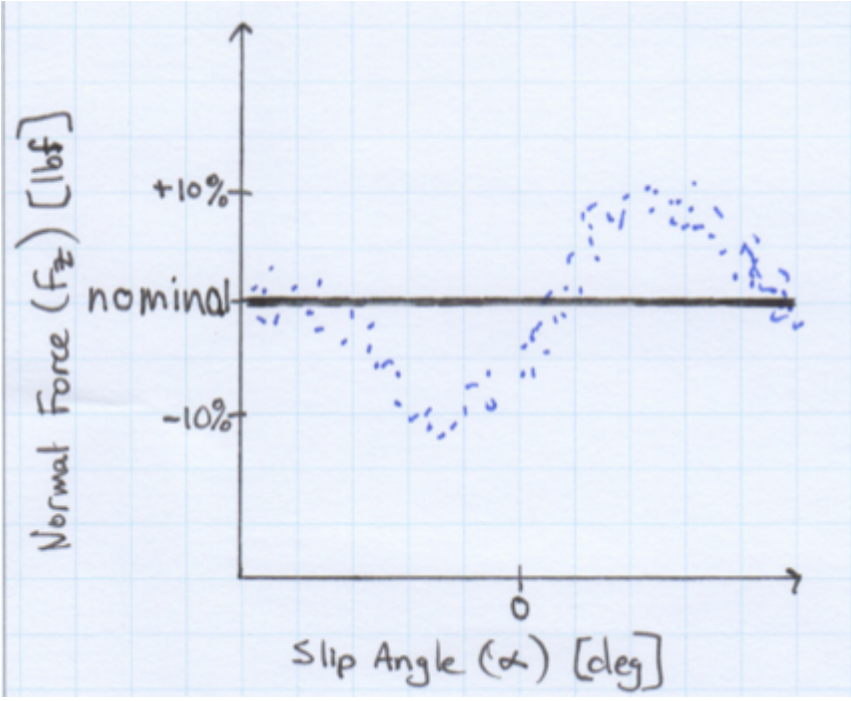

Figure 12: Normal Force Example

Figure 13 shows a representative test where the load noise range is relatively constant. Although the observed data points are well distributed around the nominal load and do not vary with slip angle, the magnitude of error is consistently around 10%.

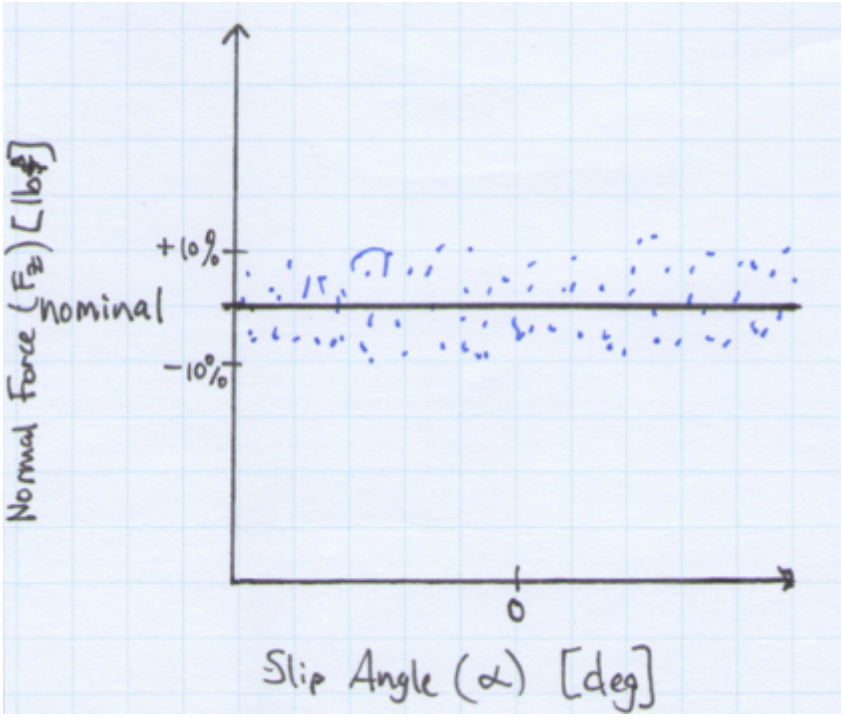

Figure 13: Normal Force Example 2

Figure 14 shows a representative test with significant load control error. The load is poorly controlled for this test across all slip angles, with errors of around 20%.

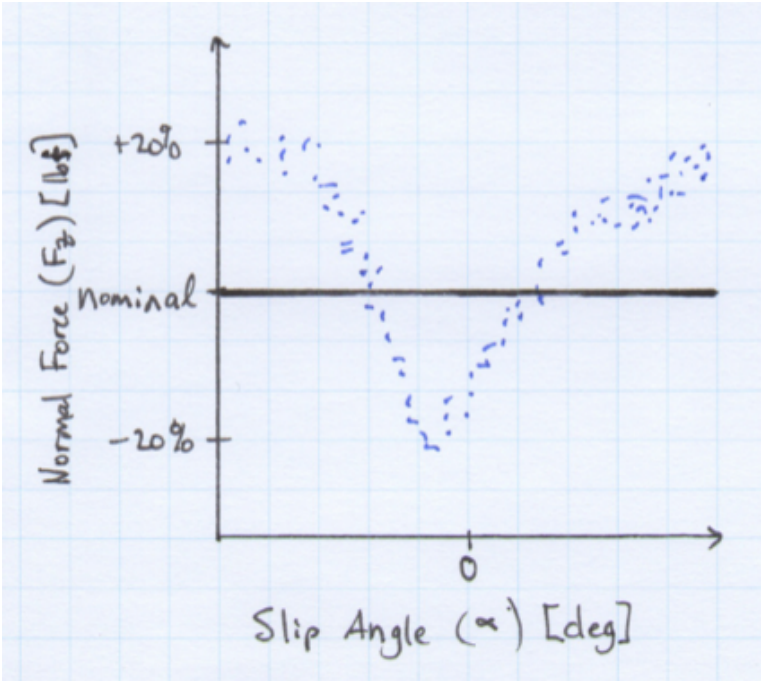

Figure 14: Normal Force Example 3

Noise may also be observed in the data, but the noise level may be independent of the nominal normal load. Figure 15 shows an example lateral response expected from the normal load shown

in Figure 13. The lateral force generated is changing based on the observed noise in the normal force. An FFT of both signals confirms that the noise in both signals are occurring at the same frequency. Due to the nature of purchased data, the cause of such noise is unknown. It is speculated, however, that the normal force variation is due to chatter in the machine or a limitation within the controls of the test machine. This noise level would be acceptable for a passenger or truck tire where the design loads are much larger. Since the noise is approximately constant across all of the observed tests, it should have a minimal effect on the accuracy of the curve fits.

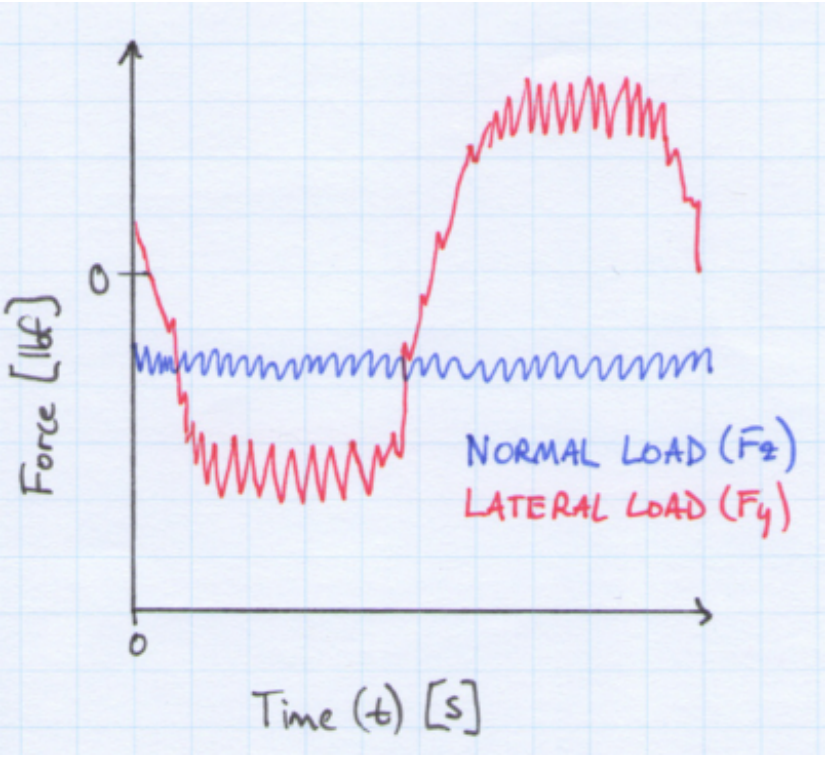

Figure 15: Coupled Vibrations

The normal force variations observed in Figure 12 and Figure 14 have a significant effect on the accuracy of the curve fit to predict lateral loads at the given nominal load, since many of the collected data points are not at the nominal load. Figure 16 shows the negative effect on quality of fit when the Magic Formula is fit to the data as is. In order to fit the curve to the sections where the normal load is not well controlled, the curve is forced to flare out at the ends where the curve should have the best agreement with the data points. In order to maximize use of the available data and preserve the quality of the data points that are close to the nominal normal force, the application of weights in the least-squares formulation is used. This is generally recommended if the data variance is not constant. An example weighting-scheme is shown in Figure 17.

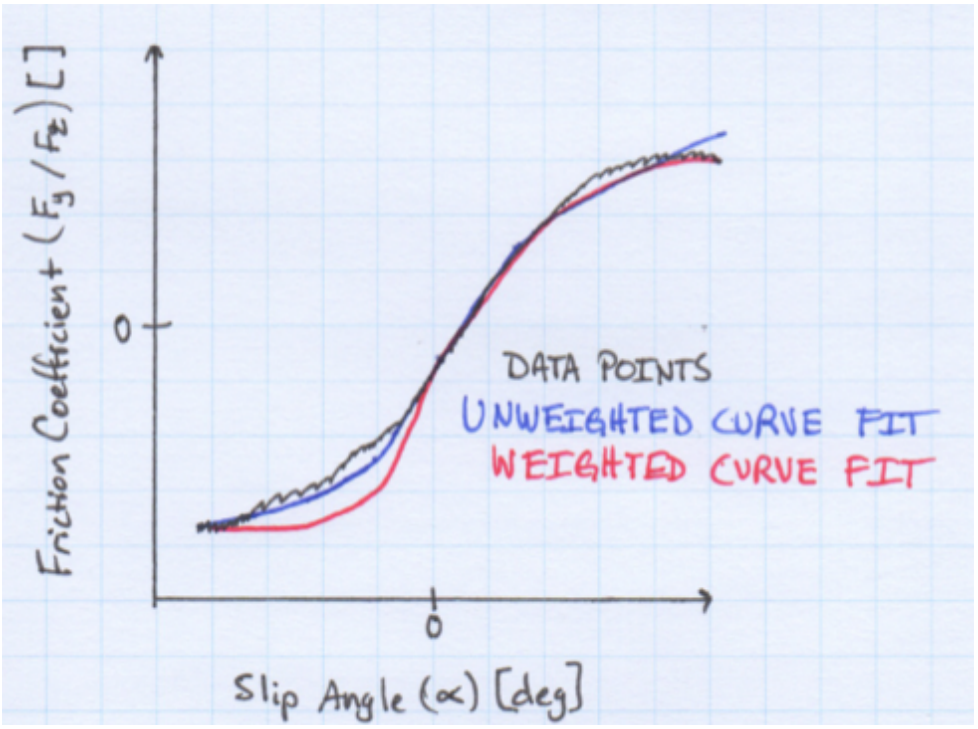

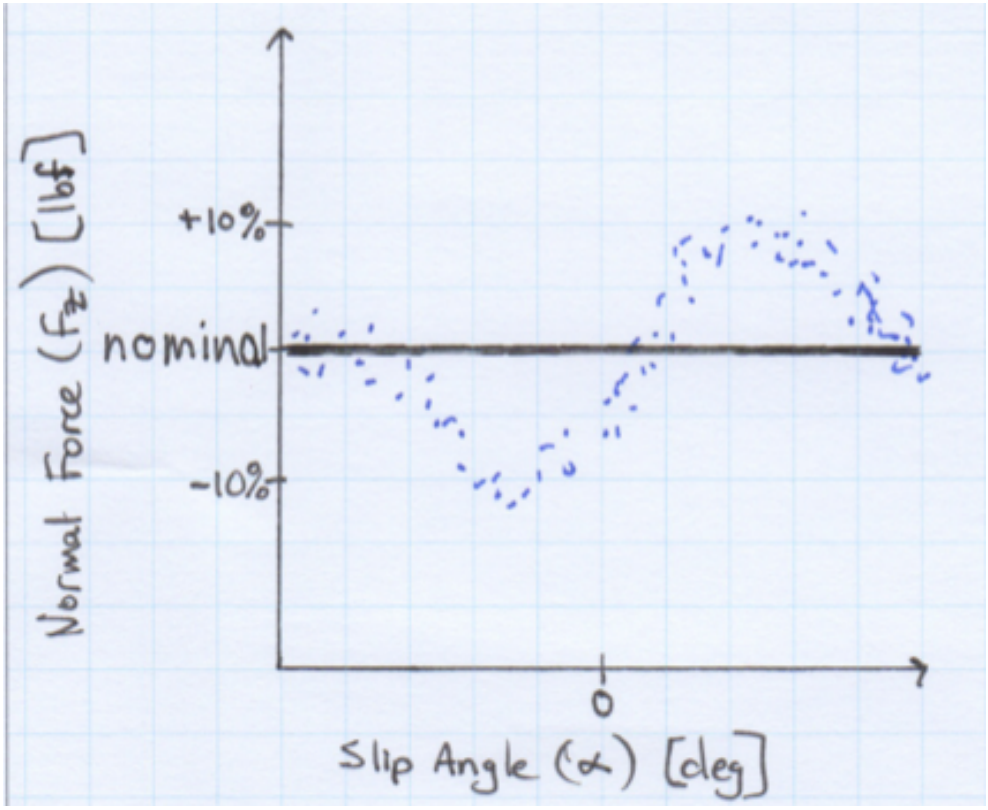

Figure 16: Curve Fitting Example

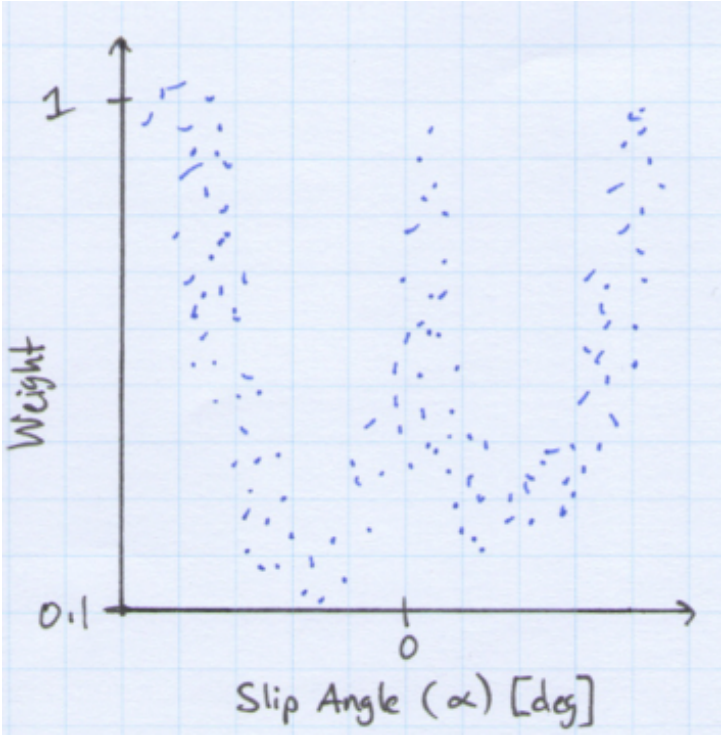

Figure 17: Curve Fitting Weights Example

Using a 0.1 - 1 scale, a 1 is given to a point whose normal load is equal to the nominal normal load, and 0.1 is given to the point in the data set that is farthest away from the nominal normal load. A power term was used to ensure greater weight on the nominally correct portions of poorly conditioned data sets. Calculation of the weights is shown in Eq. (2), where w is the weight, F_Z is the normal load, and F_{Z_Nom} is the absolute value of the nominal normal load. The numerator of the exponent calculates how far the given point is from the nominal value (the residual), and the denominator is the maximum deviation from the nominal load in the data set. These weights are then used in the least squares formulation for the curve fit as shown in Eq. (3), where SSE is the sum of squared errors, n is the number of data points in the set, $(F_y / F_Z)_i$ is the friction coefficient for the data point, and $\overline{(F_y / F_Z)_i}$ is the calculated friction coefficient from the curve fit. Other weighting schemes including linear and exponential functions were evaluated. The type of weighting scheme to apply may vary based on the data set.

$$w = 10^{\frac{-|F_Z + F_{Z\_Nom}|}{|\max(F_Z + F_{Z\_Nom})|}} \tag{2}$$

$$SSE = \sum_{i=1}^{n} w_i ((F_y / F_Z)_i - \overline{(F_y / F_Z)_i})^2 \tag{3}$$

A significant improvement in the quality of the weighted curve fit is observed in Figure 16. The curve agrees with the data points at the ends and center where the normal load is approximately the nominal normal load, and expected deviations are observed where the normal load departs

from nominal. Using this technique, the curve fits with improved representative behavior are created. Note that some data sets may not be salvageable due to extremely large deviations of the normal load relative to the nominal normal load. These data sets typically occur at high normal loads and low inflation pressures.

Tire inflation pressure also varied significantly during some of the tests. In a representative test the inflation pressure can vary around 10% from nominal. No distinct correlation can be seen between these fluctuations in inflation pressure relative to the slip angle or normal force, however it should be noted that changes in inflation pressure do affect the cornering characteristics of a tire. Greater control over inflation pressure is desired in these types of tests. The TIRF machine may be limited in its ability to keep a constant pressure in this type of tire, as the machine was designed for passenger and truck tires that have much larger air cavities and utilize higher inflation pressures.

The tire temperatures peak when the slip angle increases and then the tire is allowed to cool back to nominal for the next test. To ensure high quality data, inflation pressure and temperature profiles should be identical at the start of each test.

3.2. Normalization of Tire Data

Hundreds of tests are conducted as part of a full characterization for a tire. Although this large amount of discrete test points covers the anticipated operating conditions of the tire, it is desirable to normalize the data to generate a single master curve that accounts for the combined effects of slip and camber. Radt and Glemming [2] suggest that normalizing tire data provides the advantage of a reduced testing matrix to characterize a tire and associated costs/time along with a simpler input to vehicle dynamic simulations. It should be noted this normalization method has not been proven to work for all types of tires. The following sections detail the normalization methods and their effectiveness.

3.2.1. Normalized Slip

The first normalization to perform is normalized slip, which should collapse multiple curves for each tested normal force onto one curve for each pressure and inclination angle combination. Radt and Glemming [2] define the normalized slip angle $\bar{\alpha}$ in Eq. (4) as a function of cornering stiffness C, slip α, maximum lateral to normal force ratio μ, and vertical load Z. The normalized lateral force $\bar{F}$, is defined in Eq. (5) where F_y is the lateral load.

$$\bar{\alpha} = (C \tan\alpha) / (\mu Z) \tag{4}$$

$$\bar{F} = F_y / (\mu Z) \tag{5}$$

Using the cornering stiffnesses and maximum friction coefficients calculated from the curve fits and the raw data points, normalized slip points can be generated. A curve fit performed using the normalized points creates a normalized curve for each pressure and inclination angle combination. The curves for multiple inclination angles can be plotted together for each pressure.

This effect is consistent across all five inclination angles, and can be observed for both negative and positive extremes of the plots. A slight diminishing effect of inclination angle on cornering stiffness is also observed.

3.2.2. Combined Slip

The second normalization to perform is combined slip, which should collapse multiple curves for normal force and inclination angle onto one curve for each pressure. Equation (6) and Eq. (7) describe how to normalize the data based on combined slip, where β is the normalized slip/inclination angle, $\overline{\gamma}$ is the normalized inclination angle calculated in Eq. (8), FN is the normalized force for slip and inclination angles, and G is the camber stiffness calculated in Eq. (9) [2].

$$\beta = \overline{\alpha} / (1 - \overline{\gamma} Sgn(\alpha)) \tag{6}$$

$$FN = (\overline{F} - \overline{\gamma}) / (1 - \overline{\gamma} Sgn(\alpha)) \tag{7}$$

$$\overline{\gamma} = G \sin\gamma / (\mu Z) \tag{8}$$

$$G = (dF_y / d\gamma)_{\alpha=0} \tag{9}$$

Using raw data points and normalized data points, the combined slip points can be calculated. A curve fit performed using the combined normalized points creates a curve for each pressure. The curves for each pressure are then plotted together for comparison. The combined slip curves for each pressure highlight the effect of inflation pressure on tire response.

3.2.3. Normalization Summary

The normalized slip and combined slip methods can successfully consolidate some curve sets. The method for applying weights during curve fitting to compensate for poor normal load control is validated based on the consistent change in tire response due to changing inclination angle and/or pressure conditions.

4. TiSCTeF Design

This chapter describes the design for the Tire, Suspension, and Chassis Test Fixture (TiSCTeF). Design requirements, loads, subassembly details, finite element analyses, and instrumentation selection are discussed.

4.1. Test Fixture Requirements

The following list of requirements was created to ensure the fixture design would meet the technical and budget requirements of the project.

The design will:

- Roll the tire on one corner of the vehicle at low speed,
- Roll the tire on a flat conveyor surface,
- Measure normal (Z) reaction loads on all tires,
- Measure lateral (Y) and longitudinal (X) reaction loads for rolled tire,
- Accommodate multiple vehicles,
    - Varying front and rear track widths,
    - Varying wheelbase,
    - Varying positions of the front bulkhead and rear axle mounting,
    - Varying tire sizes,
- Apply adjustable, known normal loads to the sprung mass (up to 450 lbf per corner),
- Use strain gages to estimate loads,
- Utilize as much of the dynamic range of the strain gages as feasible,
- Incorporate load cells to validate strain gage data,
- Minimize coupling of reaction forces,
- Ability to reverse vehicle on fixture to test both front and rear car corners,
- Include uncoupled space for DIC.

4.2. Design Details

An initial design to meet these requirements was sketched by hand, and these drawings are available in the *TiSCTeF Design and Operation Guide* [15]. In order to reduce costs associated with instrumentation, the fixture was designed to measure loads using strain gages. Specific gage sections are the intended volumes where the loads will be measured. The gage sections are designed so the observed strain levels maximize the dynamic range of the strain gage sensors. In order to reduce complexity in post-processing of the data, the instrumented sections of the fixture were designed for axial loads only. Additional details regarding the strain gage selection are provided in Section 4.6.3.

The final design of the test fixture is displayed again in Figure 18. The mechanism for applying vertical loads to the vehicle is similar to the way an 8-post suspension shaker applies a simulated aerodynamic load to the vehicle. Four connection points are used to ensure that the applied load can be balanced from front-to-back and left-to-right. A roll moment can also be applied to simulate weight transfer, suspension articulation, and camber loss/gain. This fixture does not,

however, have actuators to actively control the vertical load or actuate the suspension components. Tie-ins to an existing steel baseplate are utilized where possible.

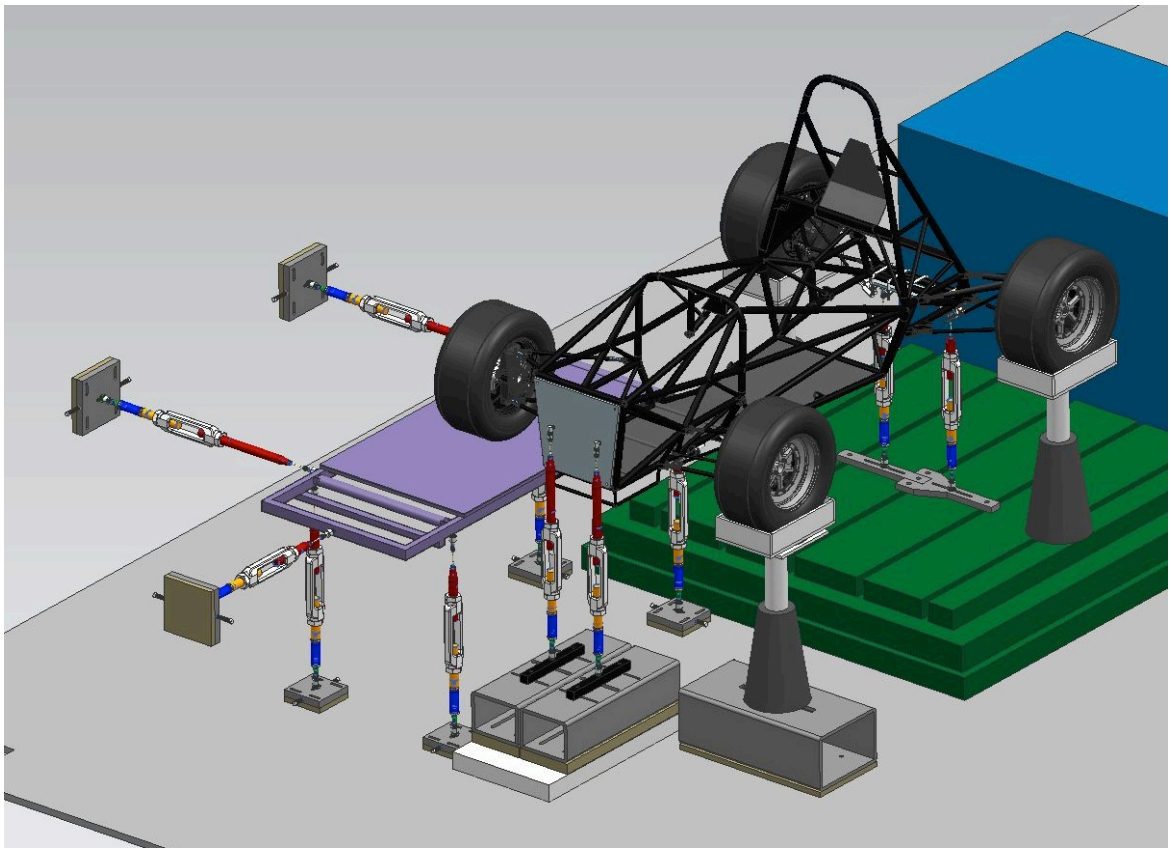

Figure 18: CAD Model of Test Fixture

The forces generated in the tire contact patch are measured via reaction forces exerted by the tire on the treadmill. The support system for the treadmill is comprised solely of seven two-force members (support axial forces only) that are arranged to ensure kinematic stability and direct measurement of the desired orthogonal reactionary forces.

Per the requirements outlined in Section 4.1, adjustability has been designed into the fixture to ensure that multiple vehicles of similar class can be tested. Specifications for the vehicle dimensions that the fixture can accommodate are listed in Table 2. The fixture has also been designed to test the vehicle with the rear wheels on the conveyor. In this configuration, the assemblies that apply a vertical load to the front and rear of the chassis are simply switched, and the conveyor is run in reverse.

Table 2: Test Fixture Vehicle Specifications

Feature	Adjustable Range
Front Track Width	38.2 – 57.2 in
Rear Track Width	38.6 – 52.6 in
Wheel Base	36.2 – 88.9 in
Front Bulkhead Load X Location from front wheel centers	8 – 16 in
Front Bulkhead Load Y Spacing	2.5 - 14 in
Rear Axle Load X Location from rear wheel centers	Practically unlimited
Rear Axle Load Y Spacing	2.5 – 18 in
Conveyor surface velocity	0 – 10 mph

4.3. Design Loads

The intended design loads for the test fixture are based on the maximum normal load that the tire is expected to experience while in service on the vehicle. In addition to static weight, aerodynamic loads and weight transfer during cornering and traction/braking loads must be considered. The FSAE TTC estimates that the highest normal loads seen by these types of tires are around 400 lbf. The TTC conservatively chose to test with loads up to 450 lbf [14]. The design load chosen for the fixture is 450 lbf to align with the TTC and ensure a direct comparison of data if larger tires are tested in the future.

Note that each corner is designed for a 450 lbf load, as the design of the fixture incorporates the entire vehicle chassis. Applied loads must be evenly distributed for the chassis to remain level, and the applied loads will be evenly distributed through the 4 contact patches. If it is desired to test the vehicle with a rolled chassis and additional static load, the reaction loads at the four wheels should be calculated to ensure that the design load is not exceeded. Additional modifications to the fixture may be required if a roll moment is applied in addition to a 450 lbf static load on each corner.

As mentioned in Section 4.2, the gage sections are designed so the observed strain levels maximize the dynamic range of the strain gage sensors. Design of the instrumented components is detailed in Sections 4.7.1 and 4.7.2.

4.4. Design of Sub-Assemblies

The support system for the treadmill and the components used to apply vertical loads to the chassis serve two fundamentally different purposes, however their designs are quite similar. The treadmill support columns must include adjustability to ensure proper alignment of the treadmill, and the vertical loading columns for the chassis must be adjustable to displace the chassis, thus applying a load on the suspension components. As a result, many of the common components in the treadmill support columns and loading columns for the chassis were standardized for a simplified design. For the purposes of this study, the components for the treadmill and chassis will both be referred to as ‘load columns.’ Assembly drawings for the fixture are provided in the

TiSCTeF Design and Operation Guide [15]. In the diagrams that follow in this Section, callouts are made for the individual components. These callouts refer to drawing titles for fabrication drawings that are included in the *TiSCTeF Design and Operation Guide* [15].

All of the components in the load columns are threaded for assembly, and nuts are used to fix the components to one another. When assembling a column, the thread engagement lengths listed in Table 3 should be used to ensure loads are properly transferred between the components and the overall column length is correct.

Table 3: Assembly Thread Engagement Lengths

Part 1	Part 2	Nominal Thread Engagement Length [in]
Lower Ball Joint	Adaptor 1	0.41
Adaptor 1	Load Cell	0.60
Load Cell	Adaptor 2	0.56
Adaptor 2	Turnbuckle	1.45
Turnbuckle	Adaptor 3	1.45
Adaptor 3	Instrumented Section	0.75
Instrumented Section	Top Ball Joint	0.50

4.4.1. Standardized Subassembly Components

Figure 19 shows the design of the load columns and the components that are standardized (identical) for all eleven columns. The baseplate for the column is specific to the mounting location. Two ball joints on either end of the column ensure that the column is acting as a two-force member and only supporting axial loads. A small adaptor is used to transition from the small threads of the ball joint to larger threads. The load cell component is typically a steel placeholder for a load cell, but it can be removed and replaced with the load cell when it is desired to validate the load measured in the instrumented section. A large turnbuckle is used along with a piece of right and left handed thread to provide adjustments to the column length while minimizing compliance. The length of the columns can be adjusted by approximately ± 1.25 in via the turnbuckle, which is sufficient to fully articulate the suspension of the vehicle along with associated compliances. The instrumented section (Treadmill_Lateral_Adaptor_4) is designed to experience an axial strain of approximately 1500 $\mu\varepsilon$, and strain gages are installed on this section to measure the axial deformation while rejecting any bending. The instrumented section could be replaced with a steel section if additional load cells are purchased and permanently installed in the fixture. Additional details about the design of the instrumented aluminum gage sections are provided in Section 4.7.2.

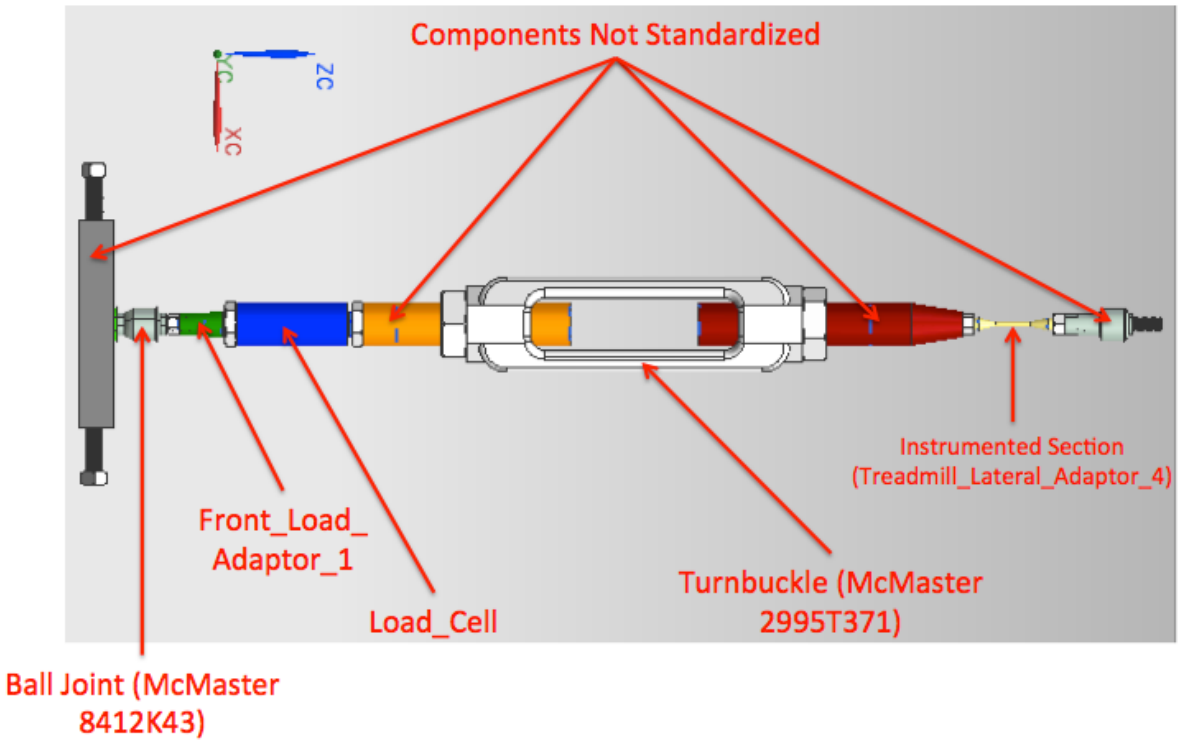

Figure 19: Standardized Components in Load Columns

4.4.2. Front Load Subassembly

The assembly that applies a vertical load to the front of the chassis is shown in Figure 20. Fairings and the impact attenuator must first be removed from the chassis. A plate bolts onto the chassis using the impact attenuator mounting points. Right-angle ball joints are used to connect the loading columns to the plate. A 3D finite-element analysis described in Section 4.5.1 was conducted to determine an appropriate thickness for the plate to ensure appropriate compliance and safety factor against yielding.

The columns mount onto bar stock that attaches to the bases made of structural steel. The stock is located in slots to provide lateral adjustment of the column location. Slots in the bottom of the bases provide longitudinal adjustment of the columns and plate. Two bases are used to decouple the load columns.

A 2D finite-element analysis described in Section 4.5.2 was conducted to determine an appropriate wall thickness for the structural steel bases to ensure appropriate compliance and safety factor against yielding.

The bases are seated on plywood gaskets to provide a compliant seating surface. The plywood is placed on a concrete slab, created to provide a level mounting surface due to an uneven floor in

the room. Bolts that are anchored through the plywood and concrete slab into the concrete floor of the room secure the bases and plywood onto the slab.

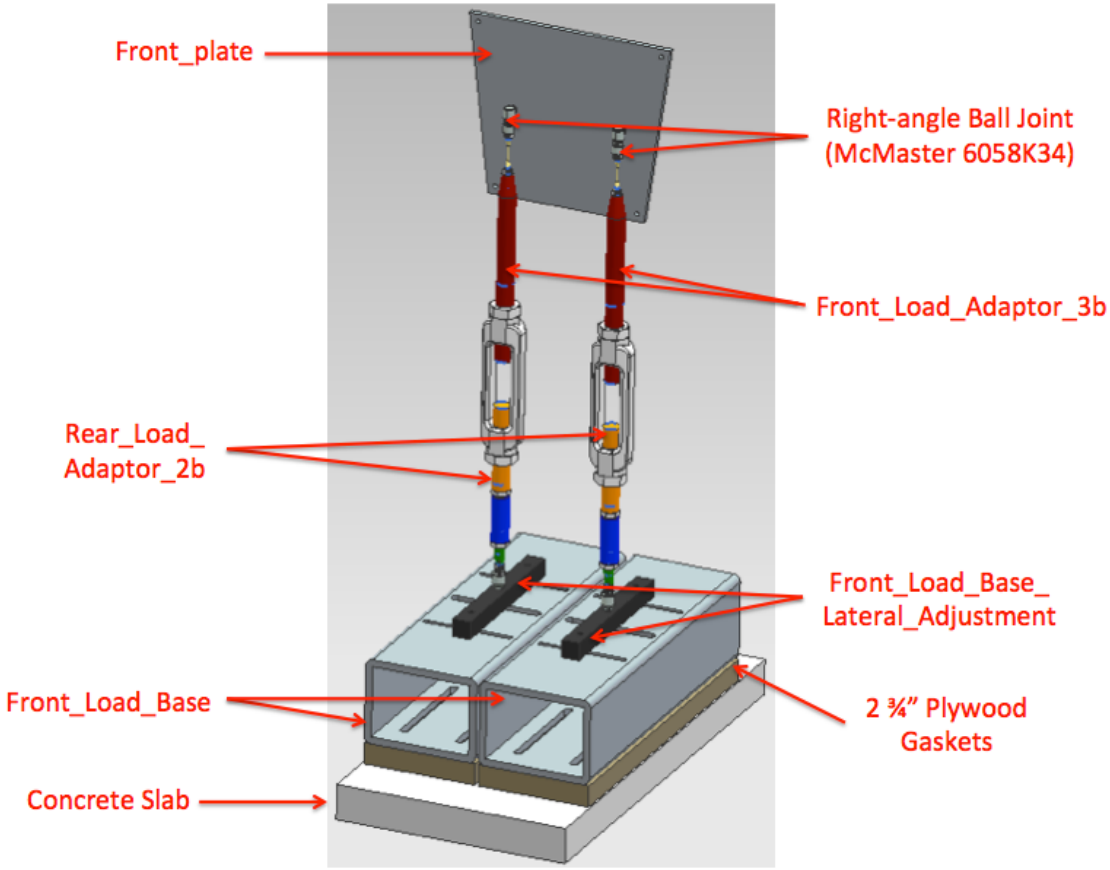

Figure 20: Front Load Assembly Diagram

4.4.3. Rear Load Subassembly

The assembly that applies a vertical load to the rear of the chassis is shown in Figure 21. The bases of the assembly mount to the existing steel baseplate in the laboratory. Slots in the baseplate allow for longitudinal adjustment of the rear load assembly. Slots in the two base pieces allow for lateral adjustment of the load columns. Two base pieces are used to decouple the load columns. The standardized load columns are used with appropriately sized thread stock to provide the correct assembly height. In-line ball joints are used to attach the top plate to the load columns. The plate at the top of the assembly is design to mount flush with a structural brace at the rear of the vehicle. Figure 22 shows how the rear load assembly is attached to the vehicle. Five U-bolts clamp the plate to the chassis frame.

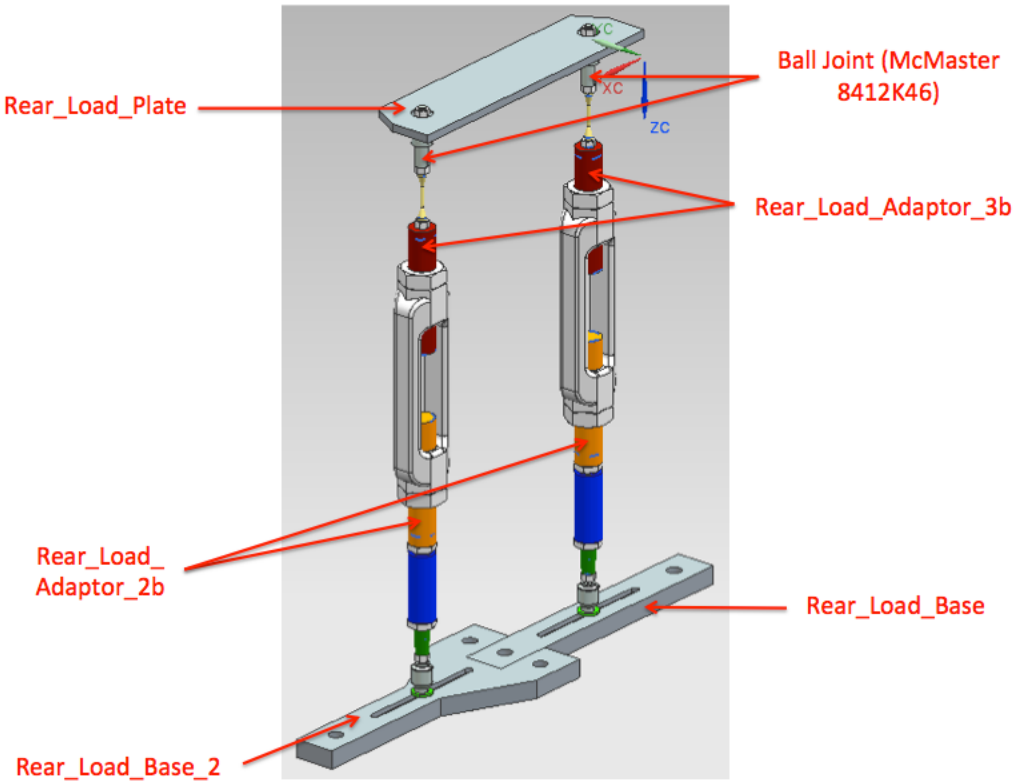

Figure 21: Rear Load Assembly Diagram

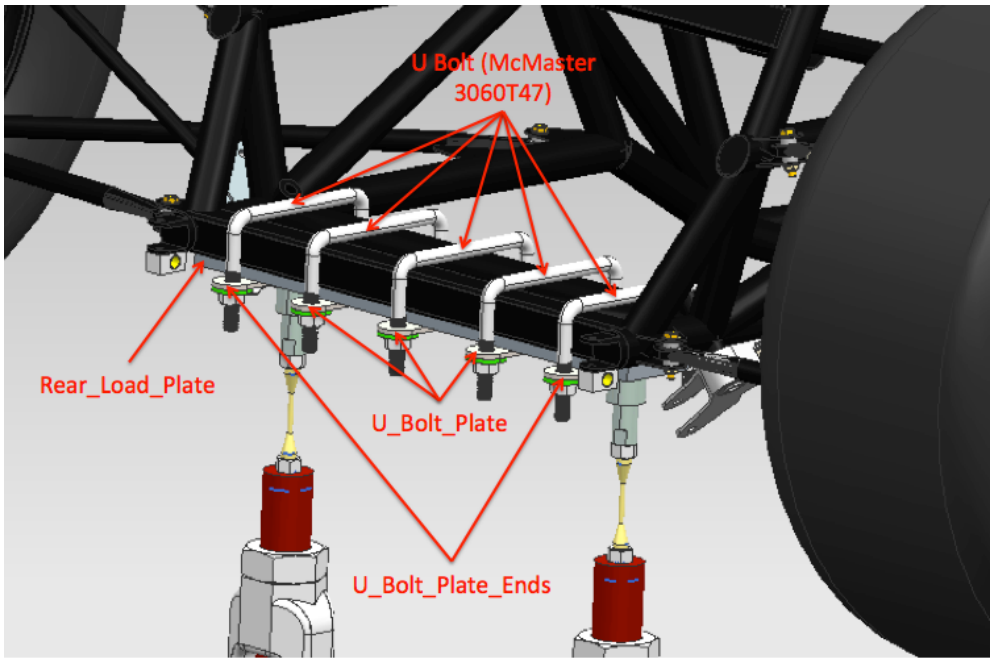

Figure 22: Rear Load to Vehicle Assembly Diagram

4.4.4. Left Front Wheel Support Subassembly

The assembly that supports the left front corner of the vehicle is shown in Figure 23. The base is another structural steel tube. Large longitudinal adjustments are not required for this component, as the longitudinal position of the wheel support is determined by the fixed treadmill location. A 2D finite-element analysis described in Section 4.5.3 was conducted to determine an appropriate wall thickness for the structural steel base to ensure appropriate compliance and safety factor against yielding.

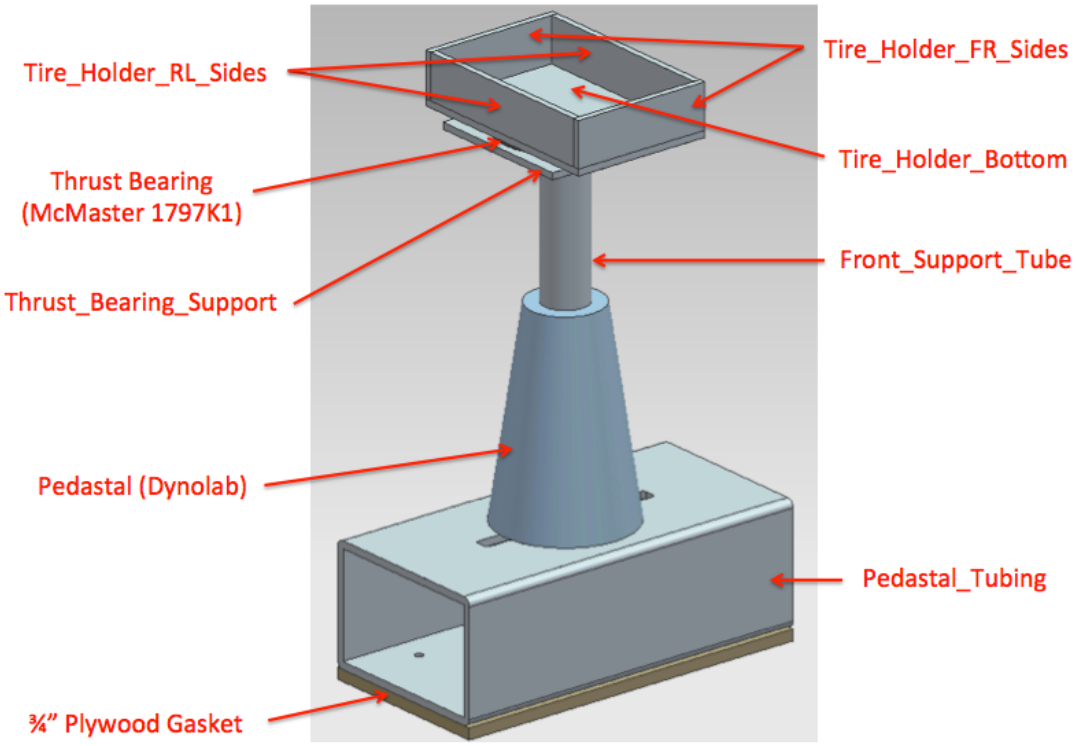

Figure 23: Left Front Wheel Support Column Assembly Diagram

The base is also mounted on a piece of plywood that acts as a gasket. Anchors placed in the concrete floor of the laboratory pass through the plywood and secure the assembly to the floor. A pedestal that was previously used as part of the dyno set up in the laboratory mounts to the base and is used to support the acrylic column. A slot cut in the base allows lateral adjustment of the column, and eccentricity in the pedestal (not pictured) allows for minor longitudinal adjustment. The acrylic tube is designed to support the tire holder where the tire is located. The acrylic tube is instrumented to provide a redundant measurement of the applied loads and understand how the load is distributed across the vehicle. Since the fixture is intended to support measurement of lateral cornering loads, the tire holder must be allowed to rotate on this corner. A thrust bearing is located between the tire holder and a bearing support plate. A 3D finite-element analysis described in Section 4.5.4 was conducted to determine an appropriate thickness for the acrylic tire holder bottom to ensure appropriate compliance and safety factor against yielding. The acrylic components are attached to each other using an acrylic solvent to create a chemical bond.

4.4.5. Rear Wheel Support Subassembly

The two assemblies that support the rear tires are shown in Figure 24. Pedestals that were previously used as part of the dyno set up in the laboratory mount to the baseplate and are used to support the acrylic columns. Slots in the baseplate provide longitudinal adjustment of the assemblies. Minor lateral adjustments can be made by rotating the assembly on the baseplate due to eccentricity in the pedestal (not pictured). The acrylic tube is designed to support the tire holder where the tire is located. The acrylic tubes are instrumented to provide a redundant measurement of the applied loads and understand how the load is distributed across the vehicle. The tire holder design for the rear wheels is identical to the design of the left front tire holder. The acrylic components are attached to each other using an acrylic solvent to create a chemical bond.

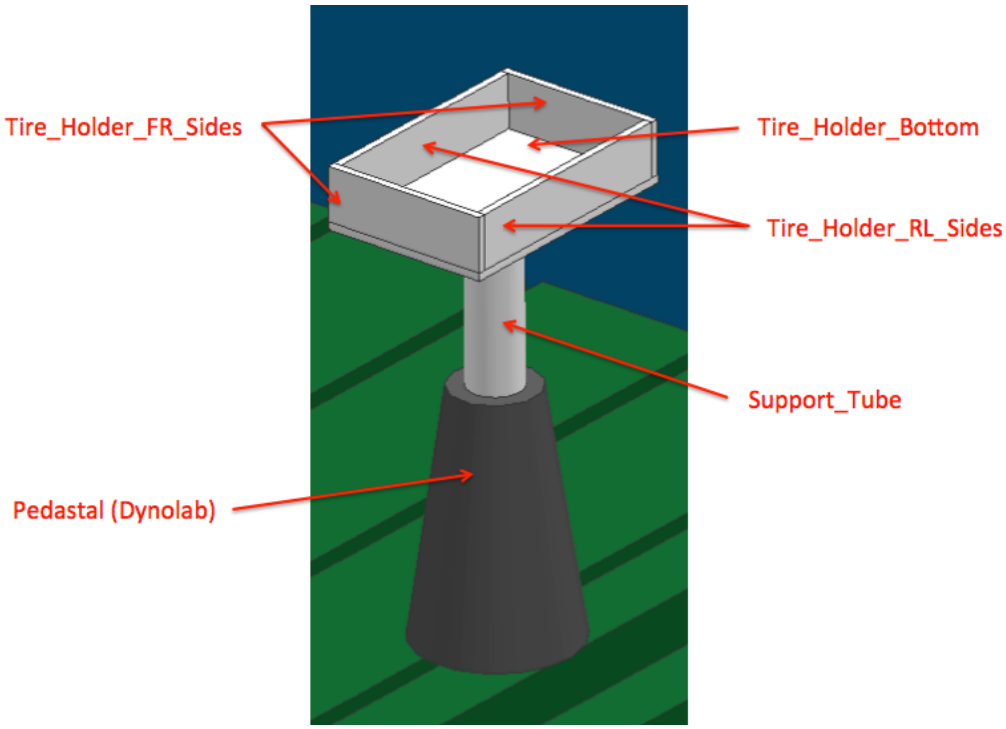

Figure 24: Rear Wheel Support Column Assembly Diagram

4.4.6. Treadmill Subassembly

The conveyor assembly that is used to roll the tire and measure the reactions to the forces generated in the contact patch of the tire is shown in Figure 25. The conveyor system is a treadmill that has been modified for use in the fixture. Two layers of carbon fiber were laid on both sides of the particleboard that supports the load applied to the treadmill. This carbon fiber 'sandwich' creates a flat surface for the tire to roll on that minimizes compliance of the structure. Nuts were welded onto the treadmill to provide attachment points for the various load columns. These load columns are positioned in a kinematically stable configuration, and they fully support the treadmill and any applied loads. The load columns directly measure the normal, lateral, and

longitudinal reaction forces. Assembly details for these three column types are displayed in Figure 26, Figure 27, and Figure 28.

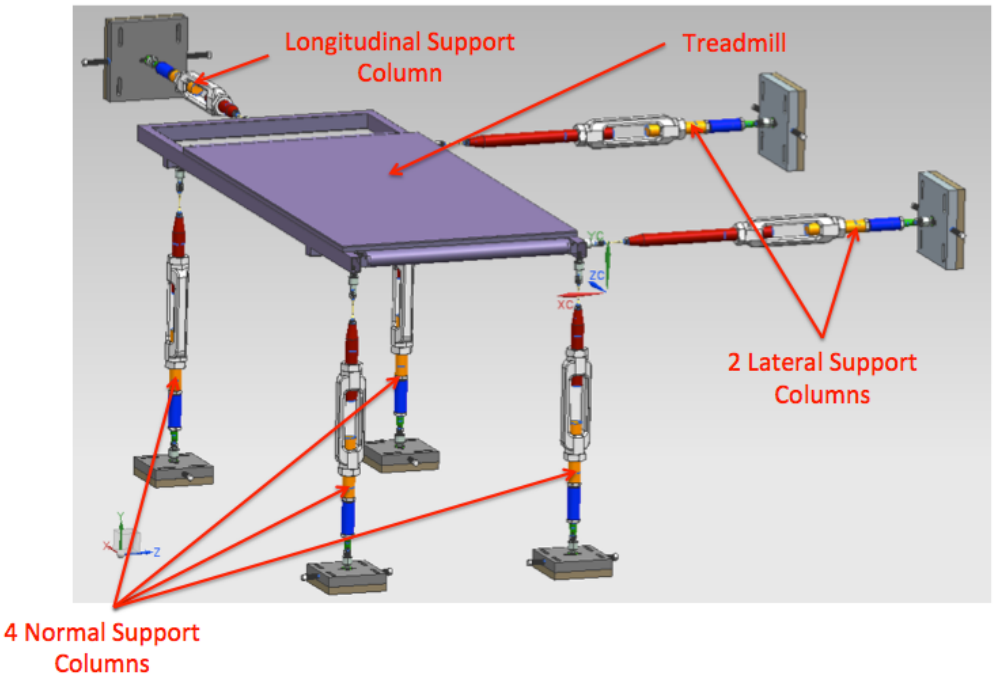

Figure 25: Treadmill Assembly Diagram

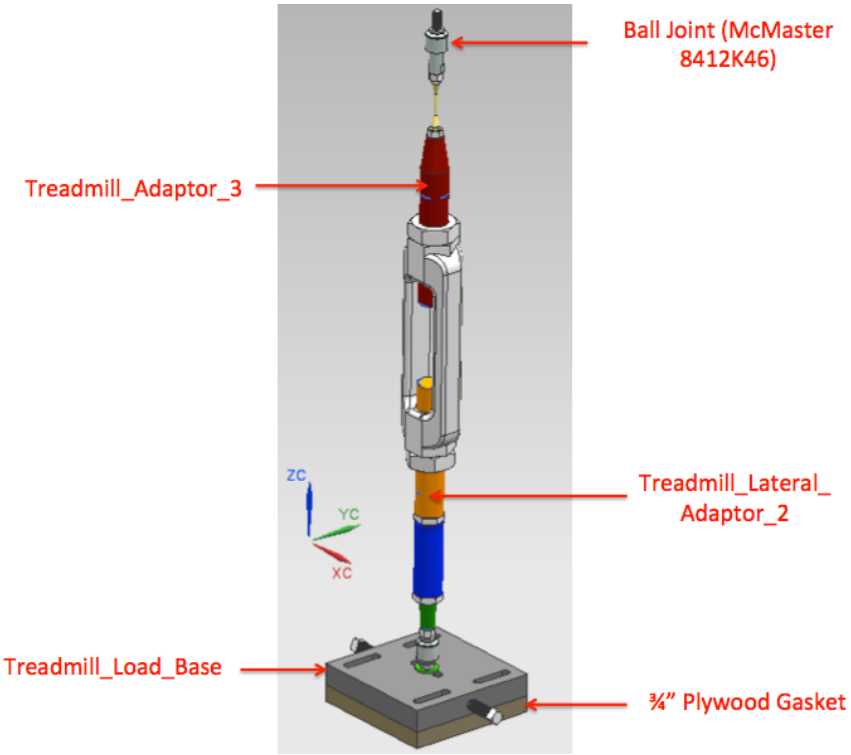

Figure 26: Normal Support Column Assembly Diagram

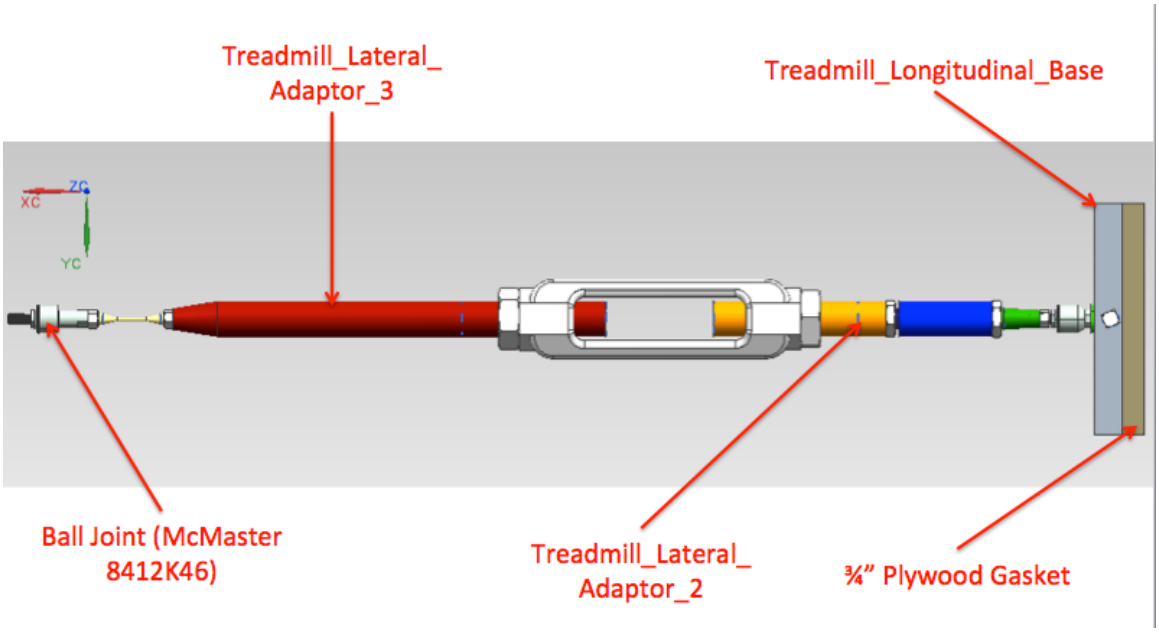

Figure 27: Lateral Support Column Assembly Diagram

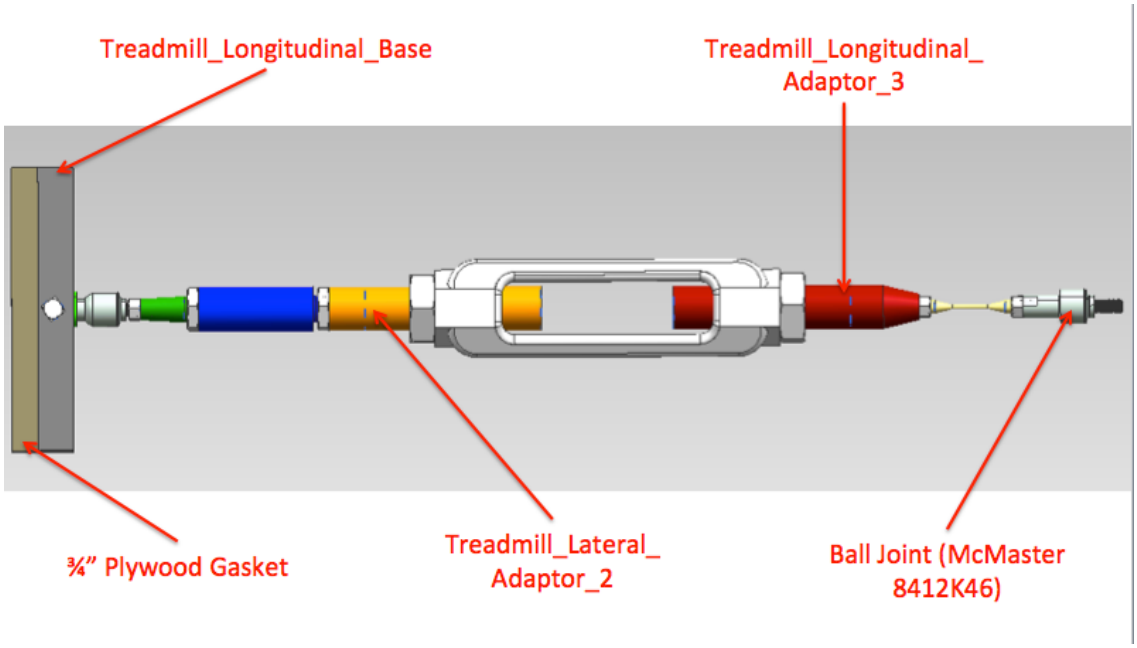

Figure 28: Longitudinal Support Column Assembly Diagram

4.5. Finite Element Analyses

The following finite element analyses were conducted to confirm that the subassembly components described in Section 4.4 were properly sized. All finite element analyses were conducted using ABAQUS v.6.12.

4.5.1. Front Load Plate FEA

The front load plate is used in the front load assembly to transfer normal loads from the load columns to the front bulkhead of the chassis and is made of mild steel. The load plate is clamped to the front bulkhead of the vehicle using existing mounting points with four cap screws and nuts. Analysis of the front load plate was conducted to confirm that the plate thickness (3/8") is appropriate for the expected loading scenarios detailed in Section 4.3.

A 3D model was selected to better approximate the stress distribution in a plate of finite thickness. The model utilized existing vertical symmetry in the plate. The boundary conditions and loads for the model are shown in Figure 29. Symmetry boundary conditions are applied along the centerline plane of the plate. Fixed boundary conditions are applied to the two bolting holes where the plate is clamped to the front bulkhead. A reference point and kinematic constraint were used to link the nodes of the hole where the load column mounts to the plate. A 375 lbf load is applied to the reference point in the negative Z-direction to simulate the application of load to the plate through the attached load column. The 375 lbf load was applied because the vehicle weight per corner without applying additional normal load is 75 lbf. These loads combined achieve the target 450 lbf normal force per corner.

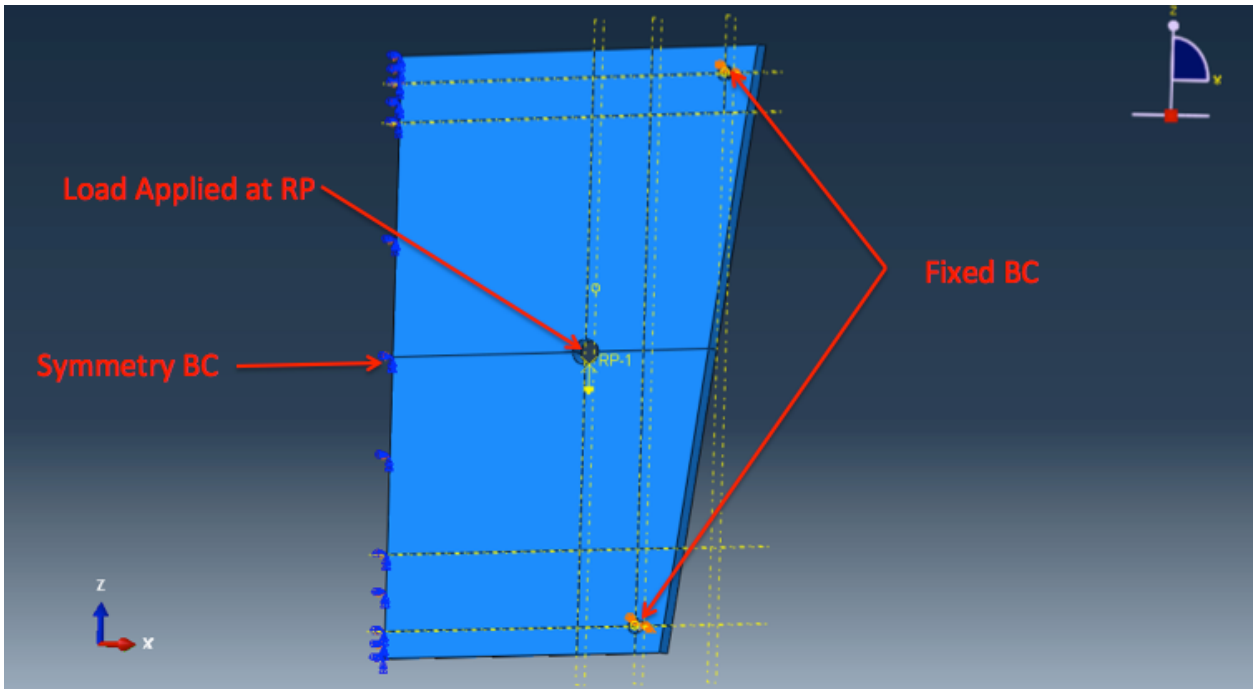

Figure 29: Front Load Plate FEA Boundary Conditions

Linear 8-node hexahedral elements (C3D8 elements) were used to mesh the part. Structured meshes were used where possible to uniformly distribute elements. Swept meshes were required in the regions near the bolt holes. The final analysis included 39,525 elements, with six elements distributed along the thickness (Y-direction) of the plate. The stress distribution in the plate under the defined loading scenario is given in Figure 30, and the displacement field is given in Figure 31. The maximum von Mises stress of 4.26 ksi, converged to within 5%, is well below the tensile yield strength of 1018 steel (53.7 ksi). The maximum observed deflection on the order of 10^{-4} inches is acceptable relative to the designed strains developed in the load columns.

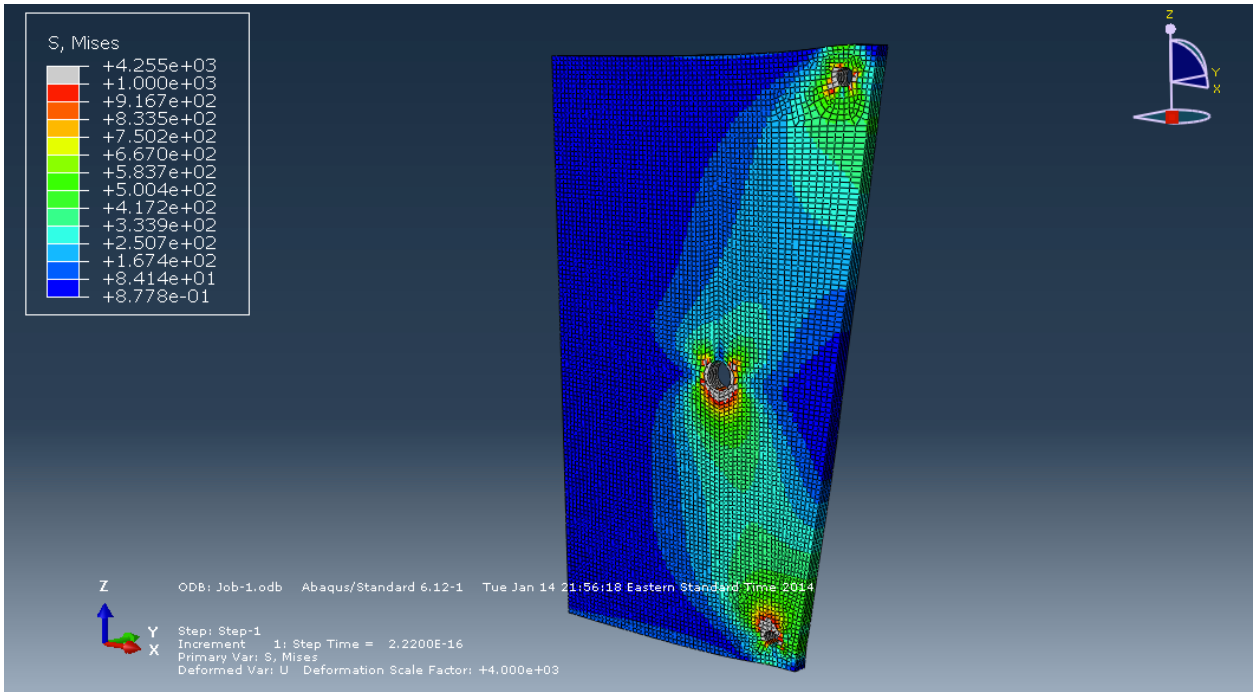

Figure 30: Front Load Plate FEA von Mises Stress Field

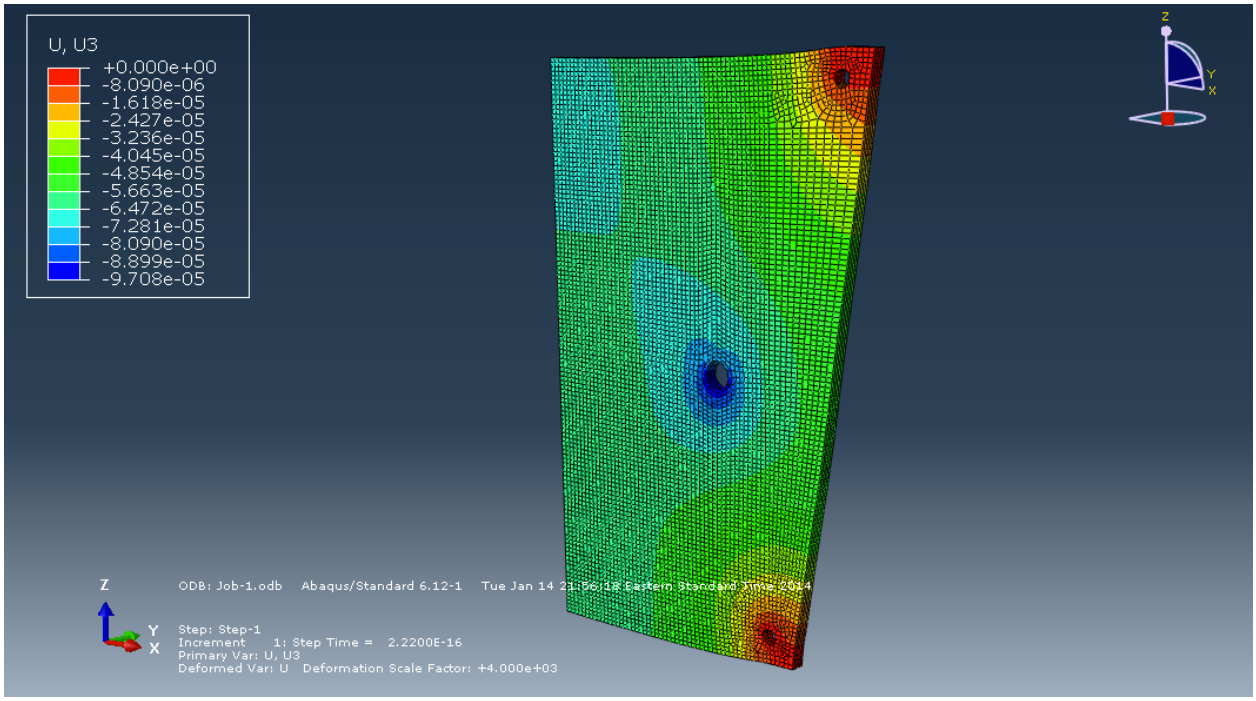

Figure 31: Front Load Plate FEA Z-Displacement Field

4.5.2. Front Load Base FEA

The front load bases are used in the front load assembly to anchor the load columns and to transfer loads into the concrete foundation of the dyno room. The bases are made of A36 structural steel tubing. The load bases are clamped to the concrete slab using anchors set into the concrete floor of the dyno room. Analysis of the front load bases was conducted to confirm that the tubing wall thickness (1/2") is appropriate for the expected loading scenarios detailed in Section 4.3.

A 2D model was selected to simplify the analysis. The tubing length (24") was entered into the section properties to account for the proper plane strain condition. The model utilized existing vertical symmetry in the tubing. The boundary conditions and loads for the model are shown in Figure 32. Symmetry boundary conditions are applied along the centerline plane of the plate. A fixed boundary condition is applied at the centerline plane on the bottom of the tubing to simulate an anchor holding the tubing on the concrete slab. A 187.5 lbf load is applied in the positive Y-direction at the top of the tubing to the to simulate the application of a tensile load from the load column. At the time of simulation, a 375 lbf load was expected to be the required maximum load in the load column. The vehicle weight per corner without applying additional normal load is 75 lbf. These loads combined achieve the target 450 lbf normal force per corner. Thus only 187.5 lbf is required in the model due to the symmetry condition.

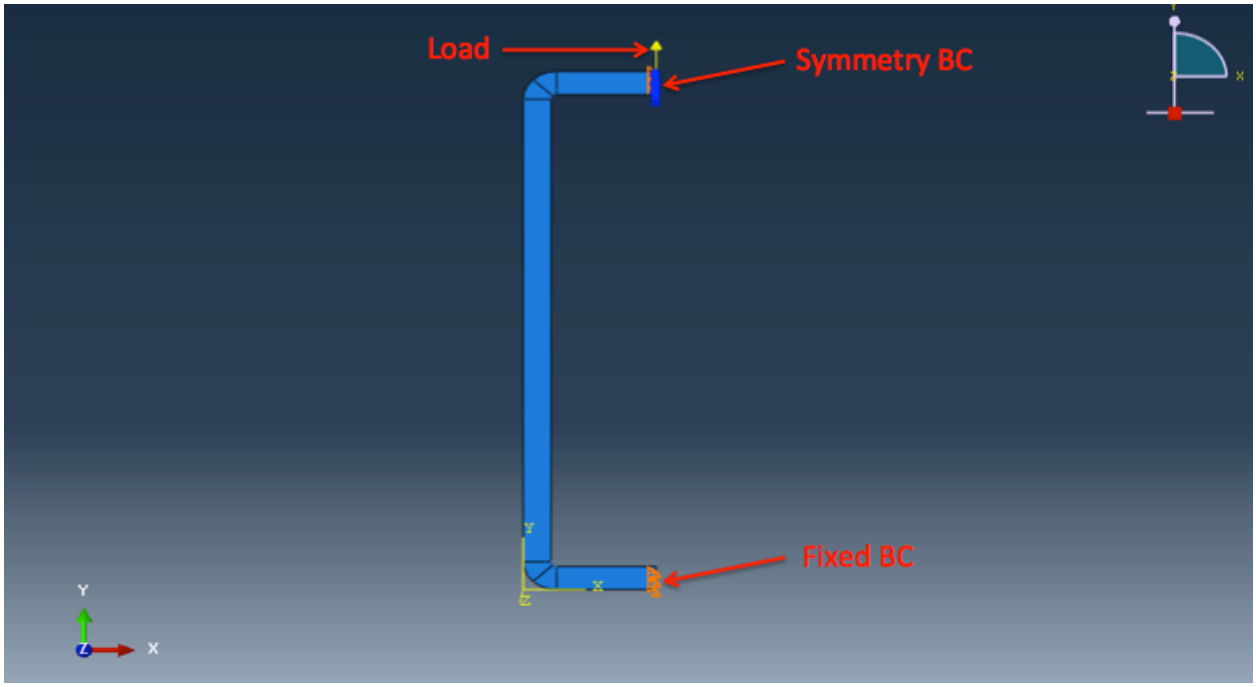

Figure 32: Front Load Base FEA Boundary Conditions

Linear 4-node quadrilateral plane strain elements with incompatible modes (CPE4I elements) were used to mesh the part. The incompatible modes feature prevents shear locking to improve the performance of linear elements under bending loads. A uniform structured mesh was used to mesh the part. The final analysis included 1,098 elements. The stress distribution in the plate

under the defined loading scenario is given in Figure 33, and the displacement field is given in Figure 34. The maximum von Mises stress of 0.38 ksi, converged to within 5%, is well below the tensile yield strength of A36 structural steel (36 ksi). The maximum observed deflection on the order of 10^{-4} inches is acceptable relative to the designed strains developed in the load columns.

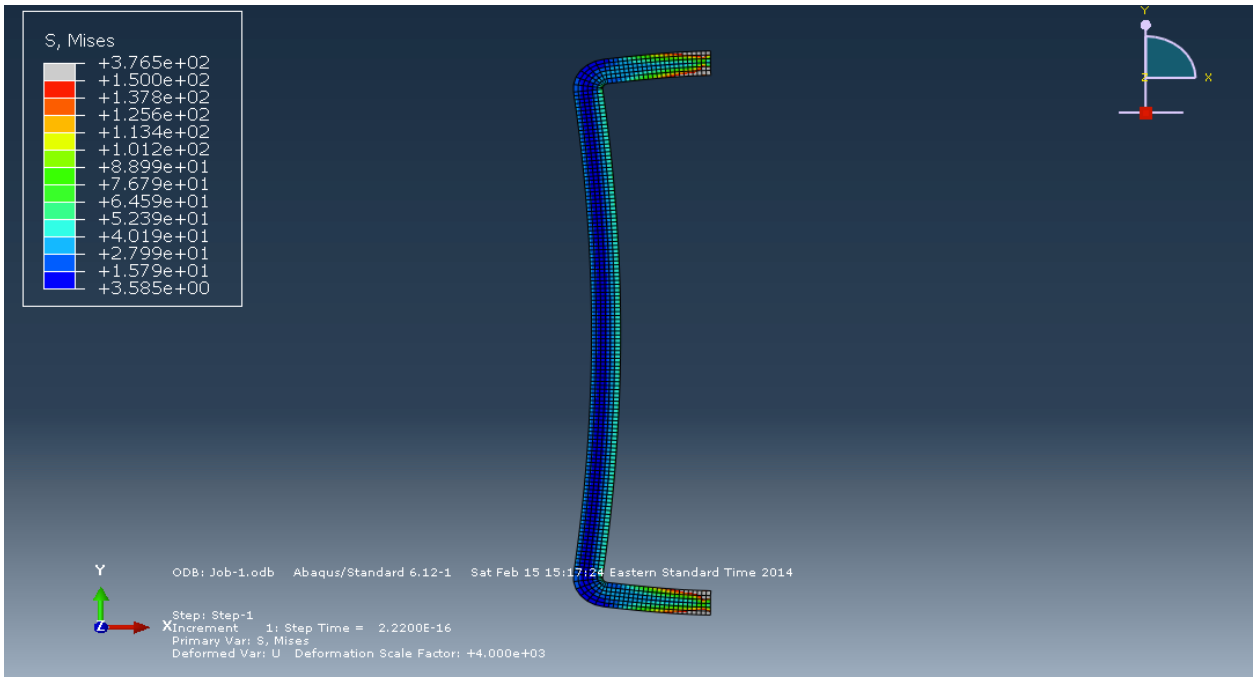

Figure 33: Front Load Base FEA von Mises Stress Field

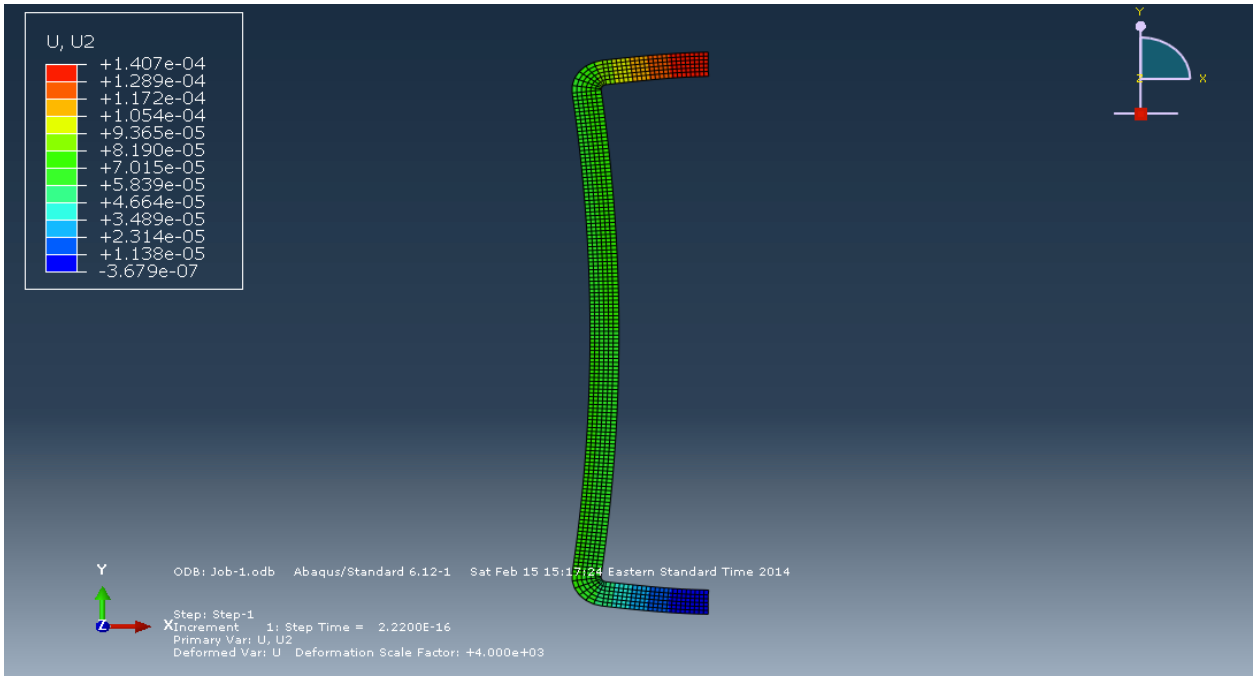

Figure 34: Front Load Base FEA Y-Displacement Field

4.5.3. Left Front Wheel Support Base FEA

The wheel support base is used in the left front wheel support assembly to support the left front wheel and transfer any reaction loads into the concrete foundation of the dyno room. The base is made of A36 structural steel tubing. The load base is clamped to the concrete slab using anchors set into the concrete floor of the dyno room. Analysis of the front load bases was conducted to confirm that the tubing wall thickness (1/2") is appropriate for the expected loading scenarios detailed in Section 4.3.

A 2D model was selected to simplify the analysis. The tubing length (24") was entered into the section properties to account for the proper plane strain condition. The model utilized existing vertical symmetry in the tubing. The boundary conditions and loads for the model are shown in Figure 35. Symmetry boundary conditions are applied along the centerline plane of the plate. A fixed boundary condition is applied on the bottom of the tubing to simulate an anchor holding the tubing on the concrete floor. A 225 lbf load is applied in the negative Y-direction at the top of the tubing to the to simulate the application of a compressive load from acrylic tube and pedestal. Due to the symmetry condition, this actually models the target 450 lbf normal force per corner.

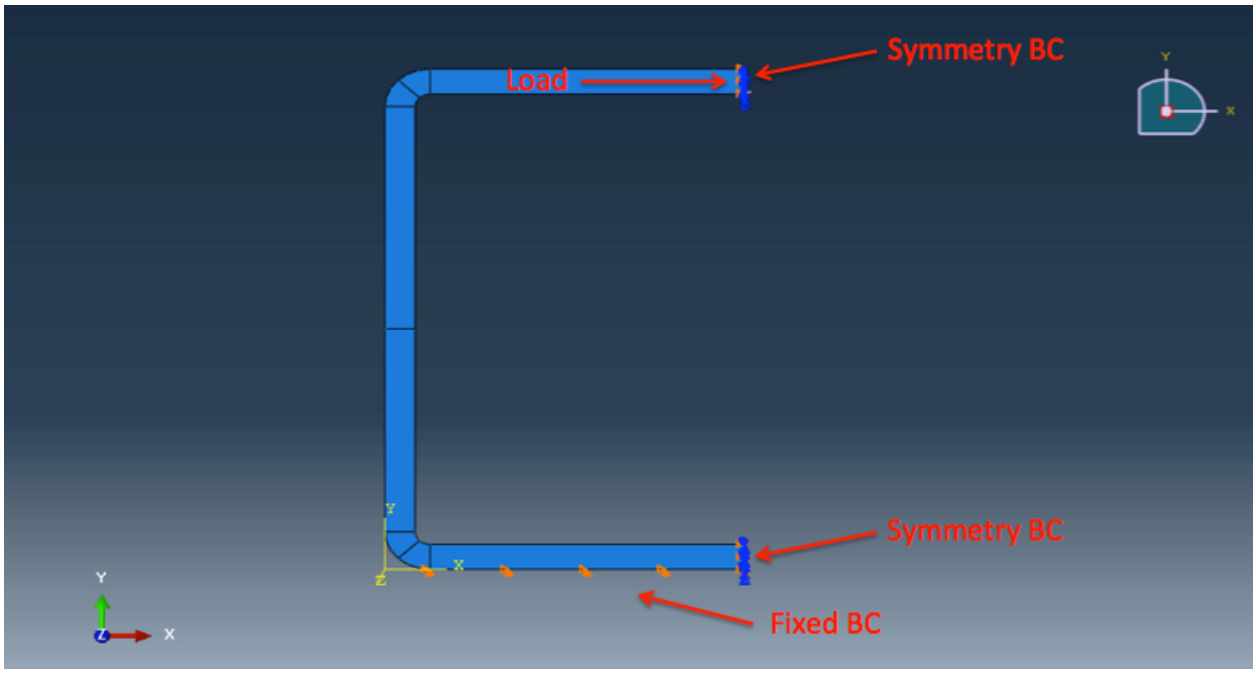

Figure 35: Left Front Wheel Support Base FEA Boundary Conditions

Linear 4-node quadrilateral plane strain elements with incompatible modes (CPE4I elements) were used to mesh the part. The incompatible modes feature prevents shear locking to improve the performance of linear elements under bending loads. A uniform structured mesh was used to mesh the part. The final analysis included 1,911 elements. The stress distribution in the plate under the defined loading scenario is given in Figure 36, and the displacement field is given in Figure 37. The maximum von Mises stress of 0.84 ksi, converged to within 5%, is well below the tensile yield strength of A36 structural steel (36 ksi). The maximum observed deflection on the order of 10^{-3} inches is acceptable relative to the designed strains developed in the acrylic columns.

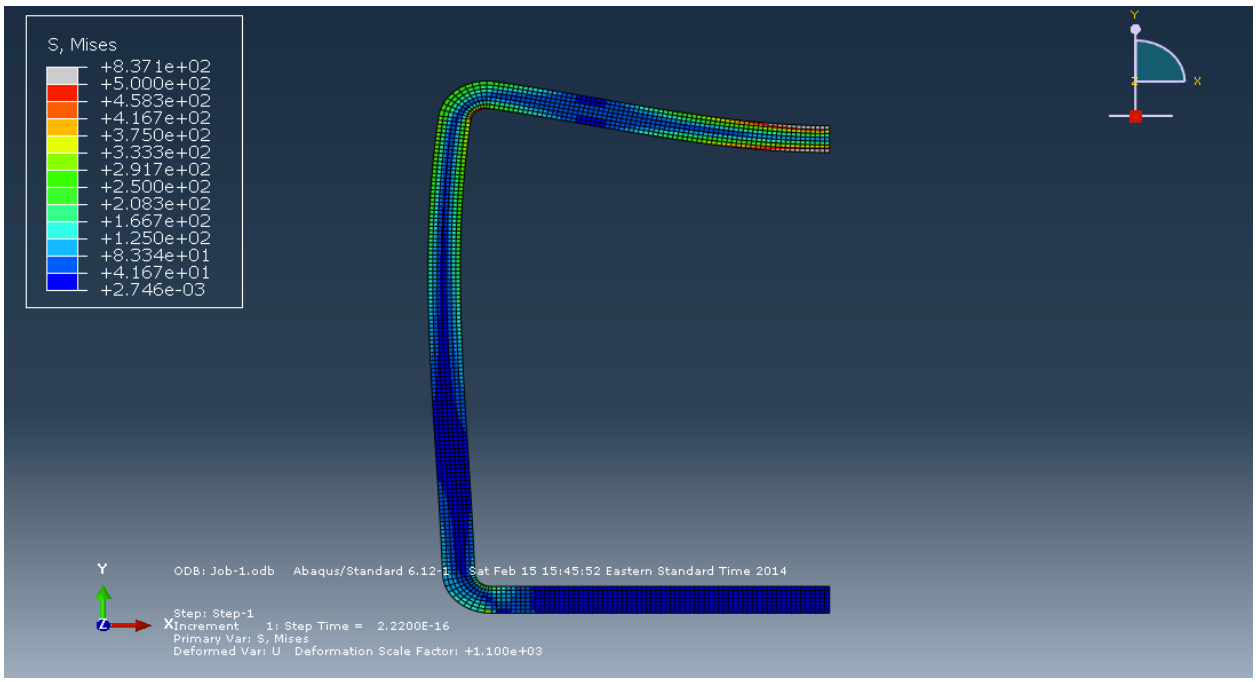

Figure 36: Left Front Wheel Support Base FEA von Mises Stress Field

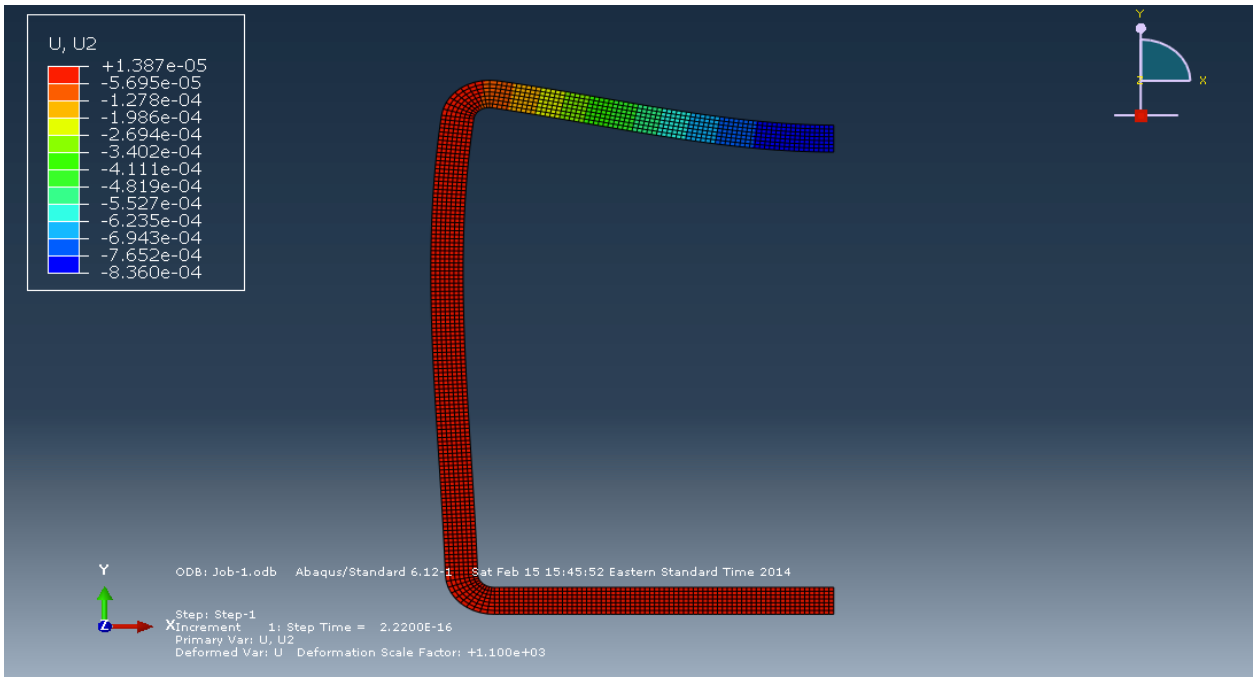

Figure 37: Left Front Wheel Support Base FEA Y-Displacement Field

4.5.4. Tire Holder Bottom FEA

The tire holder bottoms are used in the tire holder assemblies to constrain the three wheels that are not tested. All tire holder components are made of acrylic. The holder bottoms are bonded to

the acrylic tubes to transfer the reaction loads into the acrylic tubes. Analysis of the tire holder bottoms was conducted to confirm that the plate thickness (7/16”) is appropriate for the expected loading scenarios detailed in Section 4.3.

A 3D model was selected to better approximate the stress distribution in a plate of finite thickness. The model utilized existing vertical and horizontal symmetry in the plate. The boundary conditions and loads for the model are shown in Figure 38 and Figure 39. Symmetry boundary conditions are applied along both centerlines plane of the plate. Fixed boundary conditions are applied along a circumferential sector on the bottom of the plate where the acrylic tube is bonded to the plate. The tire tread width is approximately 6”, so the contact patch of the tire is assumed to be a circle 6” in diameter for the purposes of sizing the tire holder. A pressure load of 15.9 psi is applied in the negative Z-direction to a circumferential sector on the top of the plate to simulate the load applied by the contact patch of the tire. This corresponds to a 112.5 lbf load applied in the model and, due to the dual symmetry conditions, this represents a 450 lbf applied to the entire holder plate.

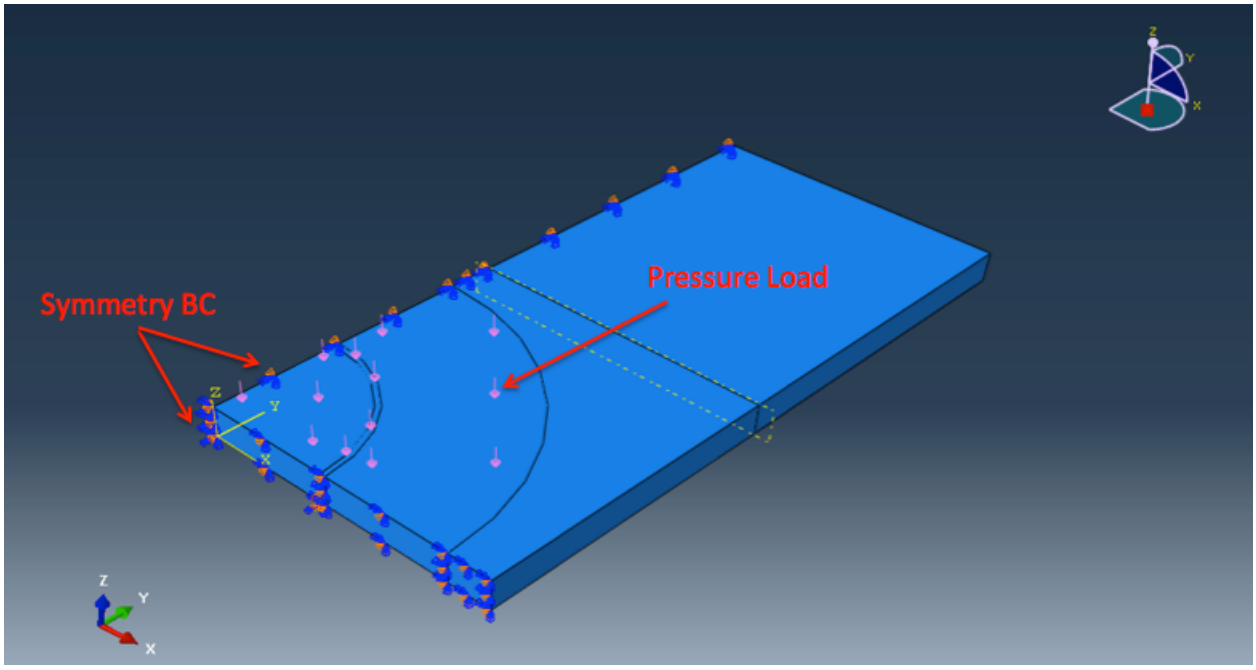

Figure 38: Tire Holder Bottom FEA Boundary Conditions

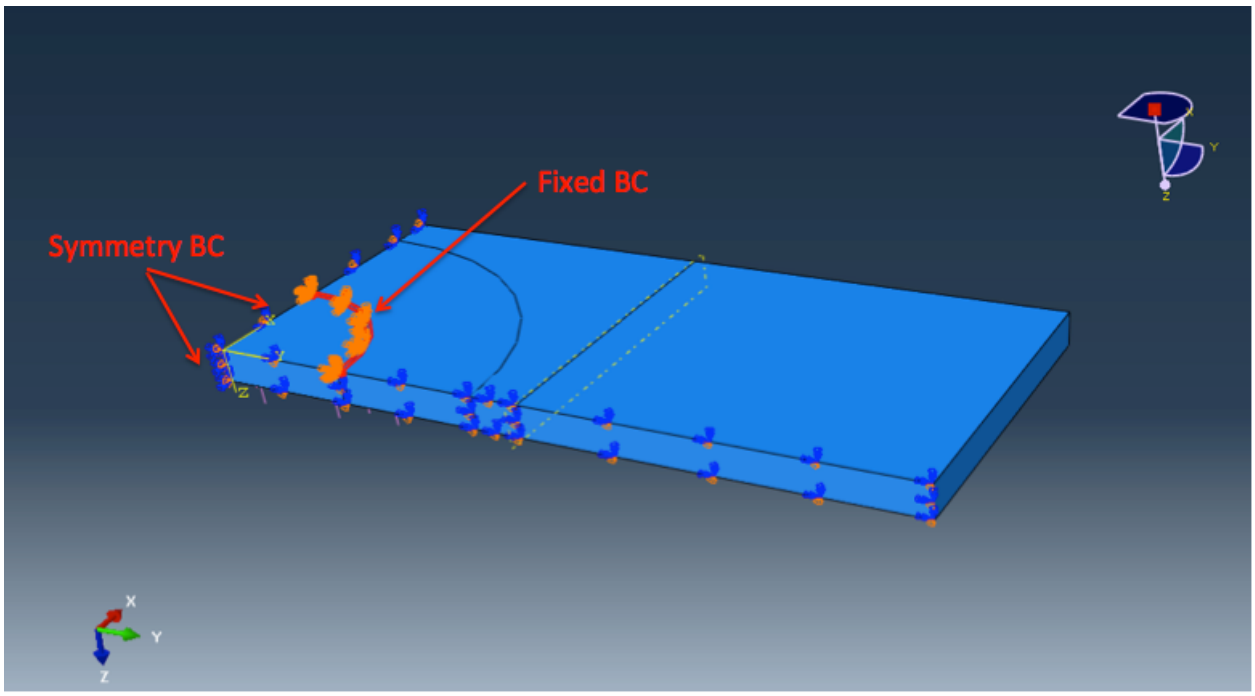

Figure 39: Tire Holder Bottom FEA Boundary Conditions Continued

Linear 8-node hexahedral elements with incompatible modes (C3D8I elements) were used to mesh the part. Structured meshes were used where possible to uniformly distribute elements. Swept meshes were required in the circular arc regions. A high concentration of elements was used in the fixed BC region to ensure accurate modeling of stress distribution near the boundary condition. The final analysis included 59,400 elements, with ten elements distributed along the thickness (Z-direction) of the plate. The stress distribution in the plate under the defined loading scenario is given in Figure 40, and the displacement field is given in Figure 41. The maximum von Mises stress of 3.23 ksi, converged to within 5%, is well below the tensile yield strength of acrylic (9 -12 ksi). The maximum observed deflection on the order of 10^{-2} inches is an acceptable deformation at the end of the plate. It should be noted that the tire holder sides were not considered in this analysis, however they will further constrain the deformation of the tire holder bottom once bonded together as an assembly.

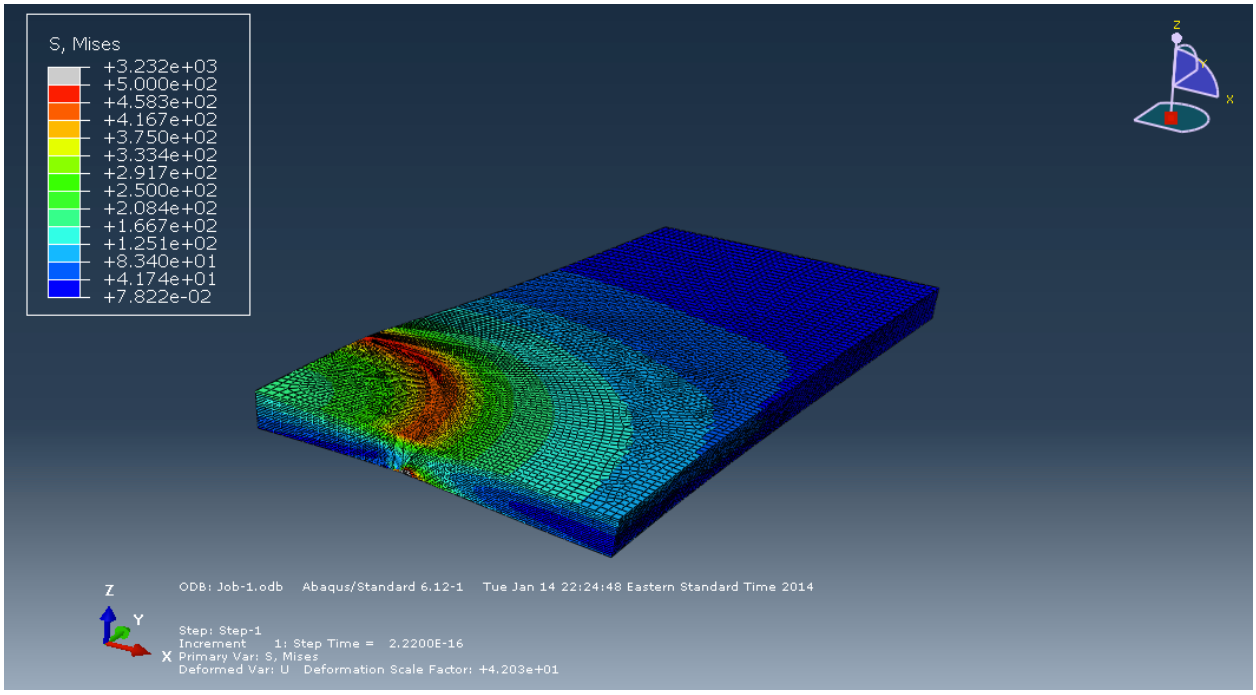

Figure 40: Tire Holder Bottom FEA von Mises Stress Field

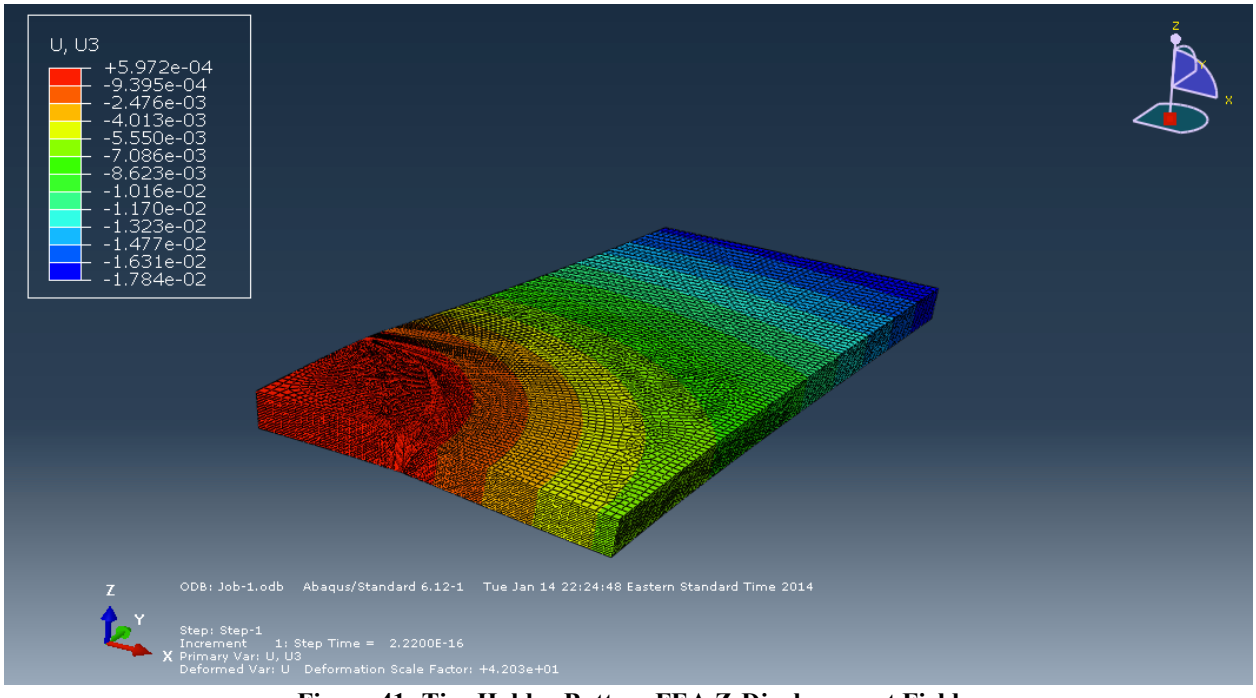

Figure 41: Tire Holder Bottom FEA Z-Displacement Field

4.6. Instrumentation

This section details the selected instrumentation components for use with the TiSCTeF. Required components include a load cell, data acquisition system, and strain gages.

4.6.1. Rod End Load Cell

Although not used in this test, the metal columns in the test fixture were designed with the option to incorporate a rod end load cell for calibration/validation and measurement purposes. A 500 lbf rod-end load cell was purchased for this project from PCB Piezotronics, along with its associated sensor cable and signal conditioner. The system was calibrated at PCB and its certifications were provided along with the unit. The signal conditioner has a display for a direct readout, however the output channel could be tied into the data acquisition system described in Section 4.6.2. A summary of the purchased components is provided in Table 4.

Table 4: Purchased PCB Load Cell Components

Item	Part No.
Rod End Load Cell, 500lbf	1380-01/LCS-2A
Cable Assembly for Sensors	8311-17-10A
Strain Gage Signal Conditioner	8159-0012A

4.6.2. NI DAQ

The data acquisition system used by the FSAE team was selected for use in this study to utilize a consistent measurement system across component, system, and full-vehicle testing. This data acquisition system will be used for both the calibration of the strain gage components as well as data collection for the test fixture. A summary of the data acquisition components used is given in Table 5.

Table 5: Components of Data Acquisition System

Type	Description
Cables	10-Position, 10-Conductor
Connectors	RJ50
Input Modules	NI 9237
Chassis	NI cDAQ-9178
Software	LabVIEW 12.0.1f5

A modular NI DAQ system is used, where a base chassis provides integrated power and timing to a series of swappable I/O modules. The system is thus highly customizable for the particular application. The NI CompactDAQ 8-slot USB chassis was used in conjunction with NI 9237 4-Channel Half/Full-Bridge Analog Input modules for this study. Five of these modules were available, providing access to twenty strain gages channels. The modules have built-in signal conditioning and filtering to provide an accurate representation of the observed signals. Three additional modules could be connected for future expansion to include temperature, load cell, conveyor motor control, or trigger inputs, for example.

The NI 9237 modules have a built in remote-sense mechanism to correct for error caused by wire resistances. Although the purpose of this study is to determine the relative strains caused by vehicle loadings and calibrations will be performed, the remote sense feature was wired to the gages for additional measurement confidence. Shunt calibrations were not performed.

LabVIEW is the software package that interfaces with the NI chassis and modules through a USB connection. LabVIEW uses a graphical programming interface and can write the collected data values to an Excel file for storage. Using LabVIEW's Front Panel, data displays can be created to view the system response in real-time. The computer used to run LabVIEW was located outside of the dyno area, however a second monitor with a duplicated display was placed in the dyno cell to easily view the system response.

Strain gage calibration results (strain vs. load) are used in the LabVIEW program to collect data from the fixture. The program calculates the applied load based on the measured strain using the calibration values, and the data that is saved and displayed will show the loads directly. No other operations are performed on the collected data except for a lowpass Butterworth filter to ensure instrumentation noise is eliminated. Operating parameters for the filter are provided in Table 6.

Table 6: Butterworth Filter Parameters

Type	Lowpass
Filter Order	1
Lower Cutoff Frequency	100 Hz
Upper Cutoff Frequency	200 Hz
Passband Ripple	1 dB
Stopband Attenuation	60 dB

4.6.3. Strain Gages

Proper selection of strain gages is important to ensure high fidelity data is collected. The components described in Sections 4.7.1 and 4.7.2 were designed to maximize the available strain range of the instrumentation where practical to increase the resolution of the fixture. The specific strain gages to be used were selected after the component design was complete. Vishay Micro-Measurements was selected as the supplier of strain gages. Technical support from Vishay was utilized during the gage selection process described further in this section.

Vishay Technical Note TN-505-4 provides recommendations for the proper selection of strain gages. Important parameters to consider include the strain-sensitive alloy material, backing material, grid resistance, gage pattern, self-temperature compensation number, gage length, and various options [16]. The EA gage series (general purpose) was recommended for this application. These gages are for use in static and dynamic stress analysis up to 3% strain, with acceptable fatigue life (10^5 cycles) achieved at strain levels of ±1800με. No special temperature requirements exist for this application.

Selection of the gage resistance is determined by cost, heat dissipation requirements, selected excitation voltage, and power limits of the bridge amplifier. Generally, higher resistance gages are more expensive, but reduce the amount of heat generated in the grid for the same applied

voltage. The 150 mW power limitation of the NI 9237 data acquisition modules was the main driver for 350 Ω gages in this project. This would allow four 350 Ω full bridges to operate on each module with a bridge excitation of 3.3V.

Recommendations for optimizing bridge excitation levels are provided in Vishay Technical Note TN-502. The charts provided therein confirm that 3.3V is an appropriate excitation level for the gages bonded to both the aluminum and acrylic sections, given the high-accuracy requirements and appropriate heat-sink conditions. A calculator is also provided on the Vishay Micro-Measurements website for the purpose of determining optimal excitation levels.

Gage lengths were determined using the geometry of the components. Since a constant uniaxial stress field is expected in the instrumented components, there was no concern about a large strain gage 'averaging' the observed strain field.

Recommendations for selecting the proper self-temperature compensation for a gage are provided in Vishay Tech Note TN-504-1. A commonly available compensation is available for aluminum alloys, however the thermal conductivity of acrylic requires a compensation number on the order of 50, which is not commonly available and relatively expensive. As an alternative, a large grid was selected with an aluminum alloy compensation number. It is noted that the acrylic gages require a warm-up period to achieve thermal stability and exhibit some nonlinearities due to this selection. A calculator is also provided on the Vishay Micro-Measurements website for the purpose of determining grid power density.

Gage layout considerations were also driven by ease of installation. 90-degree rosettes were selected to decrease the number of bonding operations by one-half. Rosettes also ensure that the neighboring gages are accurately oriented relative to each other, eliminating a potential source of error.

Encapsulated gages are preferred, as they protect the strain sensitive alloy during bonding and soldering operations. In many cases, trade-offs exist and must be considered when selecting the optimal strain gage for a given application. The strain gages selected for this project, described in Table 7, were the best fit from Vishay's stock availability that met the project requirements.

Table 7: Selected Strain Gage Specifications

	Aluminum Gage	Acrylic Gage
Vishay Part Number	EA-13-062TJ-350	EA-13-125TB-350/E
Strain Range	± 3%	± 3%
Temperature Range	-100° to +350° F	-100° to +350° F
Strain Sensitive Alloy	Constantan	Constantan
Backing Material	Polyimide	Polyimide
Grid Resistance	350 Ω	350 Ω
Gage Pattern	90° tee rosette	90° tee rosette
Self-Temperature Compensation Number	13 (Aluminum)	13 (Aluminum)
Gage Length	0.062 in	0.125 in
Gage Width	0.080 in	0.125 in
Options	None	Encapsulated

Instructions for the application of strain gages specific to this study are summarized in the *TiSCTeF Design and Operation Guide* [15].

4.7. Design of Instrumented Sections

The following subsections detail the mechanical design for the instrumented sections of the TiSCTeF. The components are designed to achieve specific strain levels for instrumentation purposes, ensure elastic deformations only, and to resist buckling.

4.7.1. Acrylic Tubing Mechanical Design

The acrylic tubing is used to support the remaining three corners of the vehicle that are not supported by the treadmill. Measurement of the axial forces in the tubes provides a redundant method for measuring the applied load to the chassis. It also provides a means of determining how the applied load is distributed across the vehicle. The selected design for the acrylic tubes is given in Table 8.

Table 8: Acrylic Tubing Design Specifications

Outer Diameter	3.000 in
Inner Diameter	2.875 in
Cross Section Area	0.5768 in^2
Material	Cast Acrylic
Compressive Yield Strength (σ_Y)	17.0 ksi
Young's Modulus (E)	443 ksi

The maximum uniaxial stress developed in the cross section of the acrylic tubes are calculated in Eq. (10). The maximum strain developed is calculated in Eq. (11), and the safety factor against yield is provided in Eq. (12).

$$\sigma = \frac{F}{A} = \frac{450lbs}{0.5768in^2} = 780psi \quad \textbf{(10)}$$

$$\varepsilon = \frac{\sigma}{E} = \frac{780psi}{443000psi} = 0.001760 \quad \textbf{(11)}$$

$$SF = \frac{\sigma_Y}{\sigma} = \frac{17000psi}{780psi} = 21.8 \quad \textbf{(12)}$$

These columns must also be designed to ensure resistance against buckling. The buckling criteria are calculated in Eq. (13), Eq. (14), Eq. (15), and Eq. (16). End conditions for the column are assumed to be one end pinned and one end fixed, since the bottom of the acrylic tube is fixed in the pedestal. The length of tube considered is the length of tube above the top of the pedestal. The theoretical length is calculated as 0.7 times the tube length.

$$I_x = \frac{\pi}{4}(r_o^4 - r_i^4) = 0.6224in^4 \quad \textbf{(13)}$$

$$r_g = \sqrt{\frac{I_x}{A}} = \sqrt{\frac{0.6224in^4}{0.5768in^2}} = 1.039in \quad \textbf{(14)}$$

$$\frac{l_e}{r_g} = \frac{0.7(9.6in)}{1.039in} = 6.46 \quad \textbf{(15)}$$

$$\left(\frac{l_e}{r_g}\right)_T = \sqrt{\frac{2\pi^2 E}{\sigma_Y}} = \sqrt{\frac{2\pi^2 443000psi}{17000psi}} = 22.7 \quad \textbf{(16)}$$

Since $\frac{l_e}{r_g} < \left(\frac{l_e}{r_g}\right)_T$, the JB Johnson equation applies. The critical load is calculated in Eq. (17), and the safety factor for the critical load is given in Eq. (18).

$$P_{cr} = \left(\sigma_Y - \frac{\sigma_Y^2}{4\pi^2 E}\left(\frac{l_e}{r_g}\right)^2\right)A = \left(17000psi - \frac{(17000psi)^2}{4\pi^2 443000psi}(6.46)^2\right)0.5768in^2 = 9407lbs \quad \textbf{(17)}$$

$$SF = \frac{P_{cr}}{P} = \frac{9407psi}{450psi} = 20.9 \quad \textbf{(18)}$$

4.7.2. Aluminum Gage Mechanical Design

The gage sections are used to measure the loads applied to the chassis and the reactionary loads imparted to the treadmill by the tire. The selected design for the metallic gage sections is given in Table 9.

Table 9: Aluminum Gage Design Specifications

Diameter	0.200 in
Cross Section Area	0.031 in^2
Material	6061-T6511 Aluminum
Compressive Yield Strength (σ_Y)	35.0 ksi
Young's Modulus (E)	10.0e+3 ksi

The maximum uniaxial stress developed in the cross sections of the aluminum gages are calculated in Eq. (19). The maximum strain developed is calculated in Eq. (20), and the safety factor against yield is provided in Eq. (21).

$$\sigma = \frac{F}{A} = \frac{450lbs}{0.0314in^2} = 14331psi \tag{19}$$

$$\varepsilon = \frac{\sigma}{E} = \frac{14331psi}{10^7 psi} = 0.001433 \tag{20}$$

$$SF = \frac{\sigma_Y}{\sigma} = \frac{35000psi}{14331psi} = 2.44 \tag{21}$$

These gage sections must also be designed to ensure resistance against buckling. The buckling criteria are calculated in Eq. (22), Eq. (23), Eq. (24), and Eq. (25). End conditions for the instrumented section are assumed to be both ends pinned. Although this is not the actual setup, the necked geometry at the ends will provide for some compliance, and this assumption is a conservative estimate. The theoretical length is then equal to the actual length.

$$I_x = \frac{\pi}{4}(r_o^4) = 7.854 * 10^{-5} in^4 \tag{22}$$

$$r_g = \sqrt{\frac{I_x}{A}} = \sqrt{\frac{7.854 * 10^{-5} in^4}{0.0314in^2}} = 0.0500in \tag{23}$$

$$\frac{l_e}{r_g} = \frac{(1in)}{0.0500in} = 20 \tag{24}$$

$$\left(\frac{l_e}{r_g}\right)_T = \sqrt{\frac{2\pi^2 E}{\sigma_Y}} = \sqrt{\frac{2\pi^2 10^7\, psi}{35000\, psi}} = 75.1 \quad \textbf{(25)}$$

Since $\frac{l_e}{r_g} < \left(\frac{l_e}{r_g}\right)_T$, the JB Johnson equation applies. The critical load is calculated in Eq. (26), and the safety factor for the critical load is given in Eq. (27).

$$P_{cr} = \left(\sigma_Y - \frac{\sigma_Y^2}{4\pi^2 E}\left(\frac{l_e}{r_g}\right)^2\right)A = \left(35000\, psi - \frac{(35000\, psi)^2}{4\pi^2 10^7\, psi}(20)^2\right)0.0314 in^2 = 1060 lbs \quad \textbf{(26)}$$

$$SF = \frac{P_{cr}}{P} = \frac{1060\, psi}{450\, psi} = 2.36 \quad \textbf{(27)}$$

4.8. Design Summary

The TiSCTeF has been designed to allow for phased approach, where future upgrades can be made to further increase the rated capacities or capabilities of the fixture. A summary of the current fixture design parameters is provided in Table 10.

Table 10: TiSCTeF Design Summary

Design Loads	450 lbf per corner
Number of Load Cells	1 @ 500 lbf rated
Placeholders for Additional Load Cells	10
Target Strain Level in Aluminum Gage Sections	1433 $\mu\varepsilon$
Target Strain Level in Acrylic Gage Sections	1760 $\mu\varepsilon$
Strain Gage Resistance	350 Ω
Bridge Excitation	3.3 V
No. of Strain Gage Channels	14
Total Suspension Articulation	± 1.5 in
Conveyor Speed	0 - 10 mph
Test Types	Load-Deflection, Free Rolling

5. Calibration of TiSCTeF Components

Calibration of the test fixture components was conducted according to the guidelines given in the *TiSCTeF Design and Operation Guide* [15]. The measurement error caused by misalignment of a strain gage is dependent upon the material's Poisson ratio and the stress state of the object. As a reference given in Vishay TN-511 [17], strain errors in a biaxial stress field can be on the order of 6% for up to 10° of misalignment. Estimates of measurement error specific for this project are not calculated, as measurement errors due to strain gage misalignments will be accounted for in the calibrations. This does not, however, relieve any requirement for accurately mounting the strain gages.

Details of the specific curve fits for the calibration data sets are described in Sections 5.1 and 5.2. The curve fit coefficients for the calibrated fixture components are given in Section 5.3. The calibration coefficients can be applied to strain data obtained from the TiSCTeF fixture post-testing, or they can be implemented directly in the data acquisition code to calculate loads from the measured strains during testing. Section 5.4 describes the calibration of the linear potentiometer used to determine the wheel center displacement during testing.

5.1. Calibration of Acrylic Gage Sections

The acrylic column gages are calibrated in compression only, as they will not experience tensile loads. The load-strain relationship for the acrylic column gages deviated slightly from linear. This is likely due to small geometrical/machining errors and some strain gage misalignment. Higher order polynomials and exponential terms (to capture any thermal effects) were analyzed to best capture the observed data points. The statistical performance of curve fits for a representative data set is summarized in Table 11, where R-square is the goodness of fit indicator, the sum squared error (SSE) represents a measure of the overall error, and the root mean squared error (RMSE) represents a measure of the error variance. Error is defined here as the difference between the measured data points and the curve fit. The optimal curve fit will minimize SSE and RMSE with evenly balanced residuals. This provides confidence that the curve fit accurately represents the observed behavior and is not influenced by noise in the data.

Table 11: Typical Acrylic Column Curve Fit Statistical Indicators

	R-square	SSE	RMSE
Linear	0.9999	9.78E+04	1.42
Quadratic	1.0000	2.61E+04	0.735
1-term Exponent	0.9311	6.40E+07	36.4
2-term Exponent	1.0000	1.30E+04	0.518
Cubic	1.0000	1.31E+04	0.522

The cubic and 2-term exponential functions achieved the lowest error variance and overall error. Although both functions are essentially identical from a statistical viewpoint, the cubic function was chosen because it best represents the expected behavior with a dominant linear term. Linear-elastic behavior is expected from the acrylic column based on the material properties and applied loads. Calibration and operational procedures described in the *TiSCTeF Design and Operation Guide* [15] should mitigate any major thermal effects, removing any exponential behavior from

the observed response. The cubic curve fit for the Front Left Acrylic Tube, Test 1 is shown in Eq. (28), where x represents microstrain and f(x) represents the load in pounds-force.

$$f(x) = -0.7253\,x^3 + 1.567\,x^2 - 137.6\,x - 213.4 \quad \textbf{(28)}$$

Note that the coefficients of Equation 28 differ from the coefficients provided in Section 5.3, because a center and scale operation was performed to clearly show the dominant linear term. The cubic fit is plotted against the collected data in Figure 42, and the error is shown in Figure 43. The load shown in Figure 42 is compressive but is displayed in quadrant I for clarity. The residuals are well distributed over the range of data points, with mostly constant error variation. Note that actual value of the residuals is lower than the ±1 lbf shown in Figure 43 due to a known step-function like output from the load frame.

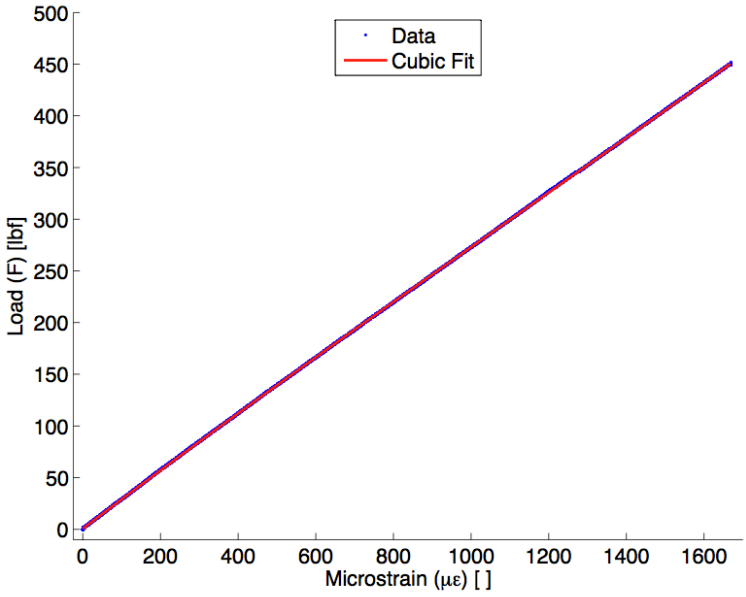

Figure 42: Acrylic Column Calibration Example (FL Test 1)

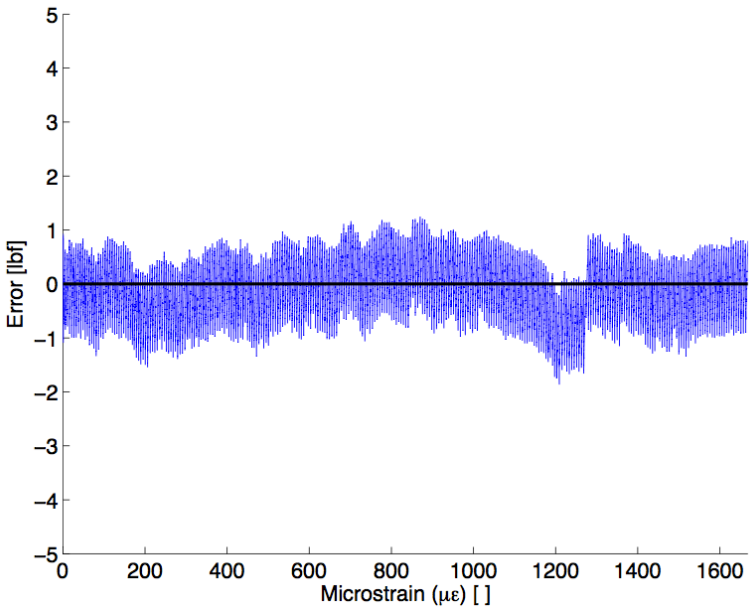

Figure 43: Acrylic Column Calibration Error Example (FL Test 1)

5.2. Calibration of Aluminum Gage Sections

The aluminum gage sections are calibrated after assembly into a load column as an assembly. The location of the aluminum gage in the fixture determines the type of calibration performed. Suggested calibration limits based on the design loads in Section 4.3 are given in Table 12.

Table 12: Aluminum Gage Calibration Load Limits

Treadmill Column	Compression Calibration Load [lbf]	Tensile Calibration Load [lbf]
Normal	-112.5	N/A
Lateral	-200	200
Longitudinal	-100	100
Front and Read Load	-75	375

The aluminum gages exhibited the expected linear load-strain response, with little to no deviation. The material lends itself to better machining precision and accuracy, and the strain gage application is simpler, reducing the chance of misalignment errors. The linear curve fit for the Treadmill Normal 1, Test 1 is shown in Eq. (29), where x represents microstrain and f(x) represents the load in pounds-force.

$$f(x) = 3.293e{+}05\ x - 0.0835 \tag{29}$$

The linear fit is plotted against the collected data in Figure 44, and the error is shown in Figure 45. The load shown in Figure 44 is compressive but is displayed in quadrant I for clarity. The residuals are well distributed over the range of data points, with mostly constant error variation. Note that actual value of the residuals is lower than the ±1 lbf shown in Figure 45, due to a known step-function like output from the load frame.

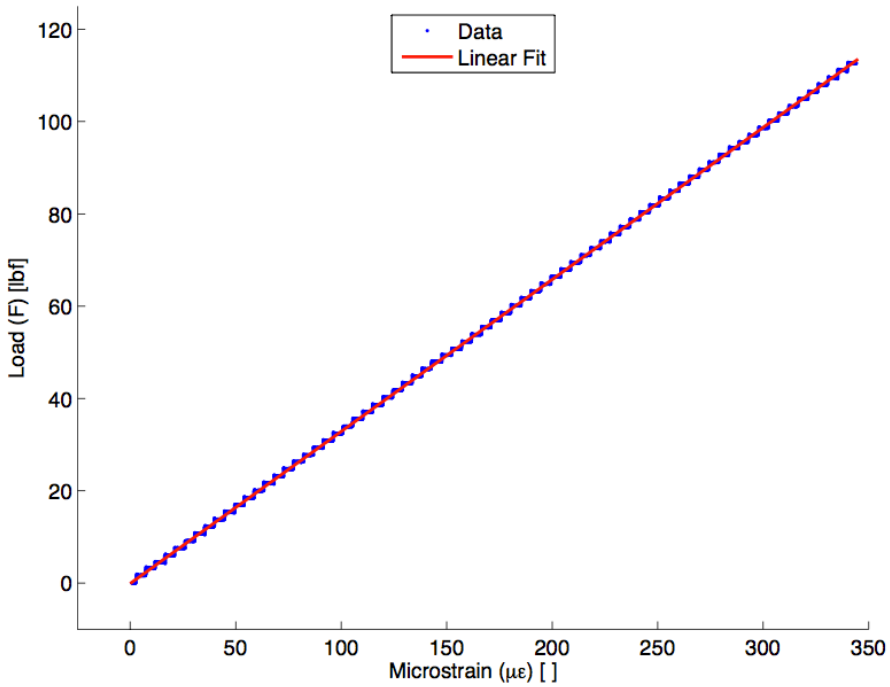

Figure 44: Aluminum Gage Calibration Example (TR Normal 1, Test 1)

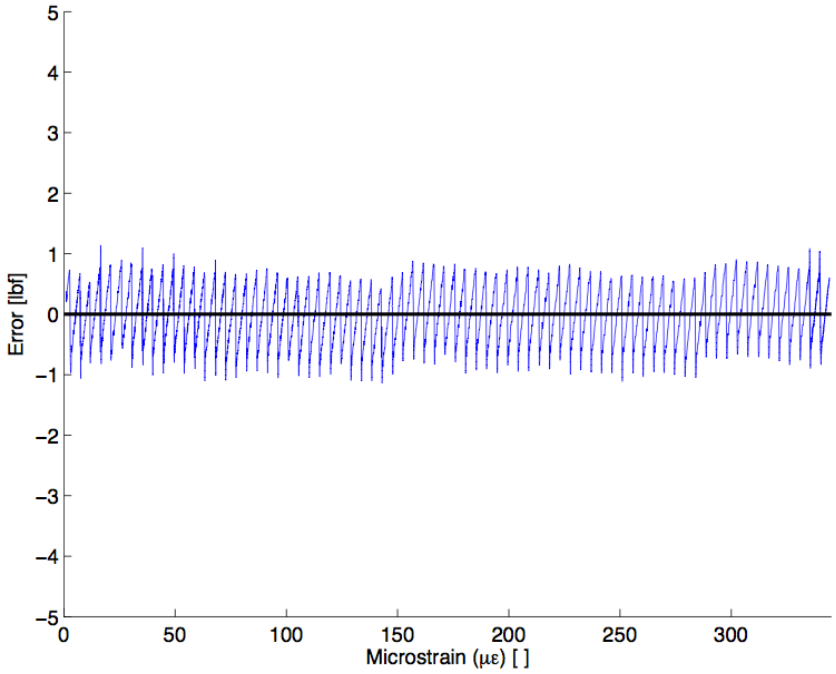

Figure 45: Aluminum Gage Calibration Error Example (TR Normal 1, Test 1)

5.3. Fixture Calibration Summary

The curve fit coefficients for the calibrated fixture components are provided in Table 13, Table 14, Table 15 and Table 16. These calibrations should be performed regularly to ensure measurement accuracy.

Table 13: FL Acrylic Column Calibration Results

Date of Calibration		Coefficient	Cubic Coef (lbf/microstrain)		Best Fit Values
7/30/13	Test 1	p1	-5.2780E+09		
		p2	1.8160E+07		
		p3	-2.8520E+05		
		p4	-6.6800E-01		
	Test 2	p1	-5.5700E+09		**-6.376E+09**
		p2	2.0680E+07		**2.173E+07**
		p3	-2.8820E+05		**-2.882E+05**
		p4	-9.7660E-01		**0.000E+00**
	Test 3	p1	-8.2800E+09		
		p2	2.6360E+07		
		p3	-2.9130E+05		
		p4	-1.4270E+00		

Table 14: RL Acrylic Column Calibration Results

Date of Calibration		Coefficient	Cubic Coef (lbf/microstrain)		Best Fit Values
7/30/13	Test 1	p1	-6.9470E+09		
		p2	2.5200E+07		
		p3	-2.7720E+05		
		p4	-8.5040E-01		
	Test 2	p1	-3.9270E+09		**-5.545E+09**
		p2	1.8070E+07		**2.186E+07**
		p3	-2.7440E+05		**-2.763E+05**
		p4	-1.1590E+00		**0.000E+00**
	Test 3	p1	-5.7610E+09		
		p2	2.2300E+07		
		p3	-2.7730E+05		
		p4	-1.4740E+00		

Table 15: RR Acrylic Column Calibration Results

Date of Calibration		Coefficient	Cubic Coef (lbf/microstrain)		Best Fit Values
7/30/13	Test 1	p1	-7.8210E+09		
		p2	2.6560E+07		
		p3	-2.9030E+05		
		p4	-1.1450E+00		
	Test 2	p1	-6.4680E+09		**-7.914E+09**
		p2	2.3440E+07		**2.689E+07**
		p3	-2.8880E+05		**-2.909E+05**
		p4	-1.6310E+00		**0.000E+00**
	Test 3	p1	-9.4520E+09		
		p2	3.0660E+07		
		p3	-2.9360E+05		
		p4	-8.0610E-01		

Table 16: Metal Column Calibration Results

	Date of Calibration		Slope (lbf/microstrain)	Average Value
TR Normal 1	8/6/13	Test 1	0.3293	0.329
		Test 2	0.3291	
		Test 3	0.3297	
TR Normal 2	8/6/13	Test 1	0.3233	0.323
		Test 2	0.3229	
		Test 3	0.3238	
TR Normal 3	8/5/13	Test 1	0.3125	0.312
		Test 2	0.3124	
		Test 3	0.3124	
TR Normal 4	8/5/13	Test 1	0.3306	0.331
		Test 2	0.3307	
		Test 3	0.3304	
TR Longitudinal (Compression)	8/6/13	Test 1	0.3093	0.309
		Test 2	0.3092	
		Test 3	0.3090	
TR Longitudinal (Tension)	8/6/13	Test 1	0.3086	0.309
		Test 2	0.3087	
		Test 3	0.3094	

5.4. Calibration of Spring Linear Potentiometer

A linear potentiometer is used to measure the spring deflection on the corner of interest when a load is applied to the vehicle. The spring deflection is then related to the wheel center displacement through the suspension kinematics. A Penny+Giles SLS 095/75 Linear Displacement Sensor was mounted to the spring/shock assembly as shown in Figure 46. The sensor ends are threaded caps that screw over the nuts onto the bolts holding the spring assembly. Spherical rod-end bearings between the mounting points and the sensor itself allow the unit to self-align.

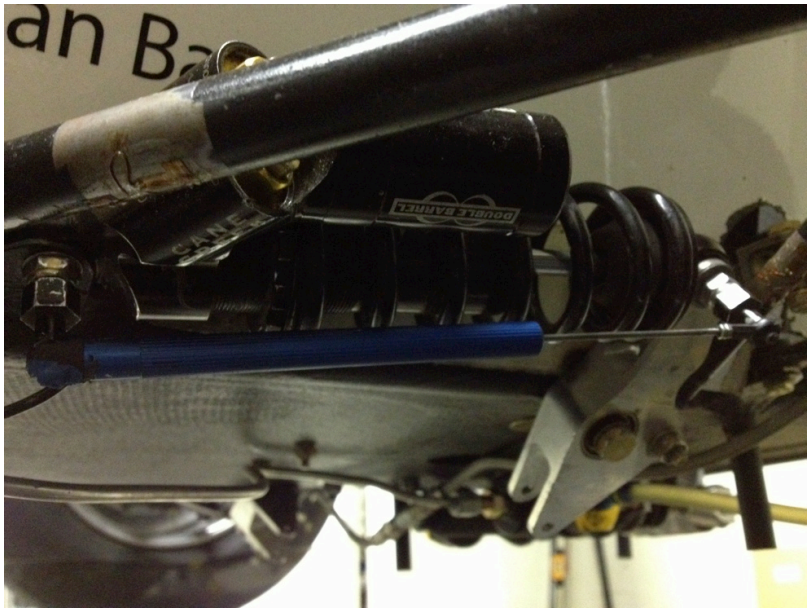

Figure 46: Linear Potentiometer Mounted to Spring Assembly

Due to instrumentation issues at the time of testing, an adjustable DC power supply and voltmeter were used to power the sensor and measure the voltage output (Figure 47). The values were simply recorded by hand. If future testing is conducted with the displacement sensor, it is highly recommended to tie the sensor in with the data acquisition system.

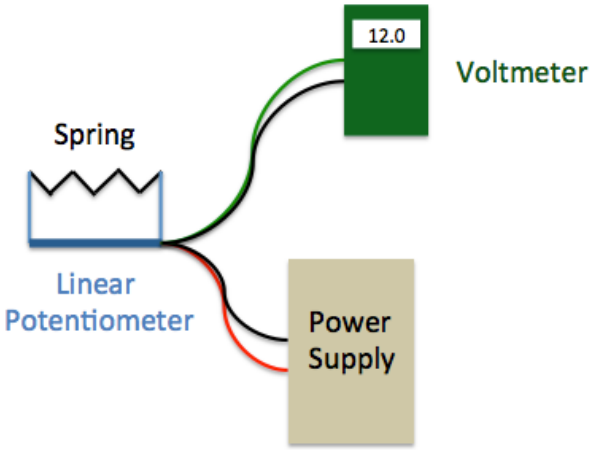

Figure 47: Linear Potentiometer Wiring Diagram

Due to the geometry of the suspension system, the displacement sensor is aligned on a different axis than the spring. Therefore, the sensor does not directly measure the displacement of the spring. The 3-D CAD model of the chassis and bell crank shown in Figure 48 was used to determine a displacement relationship between the sensor and the spring. The length of the spring was varied, and the corresponding sensor length was measured.

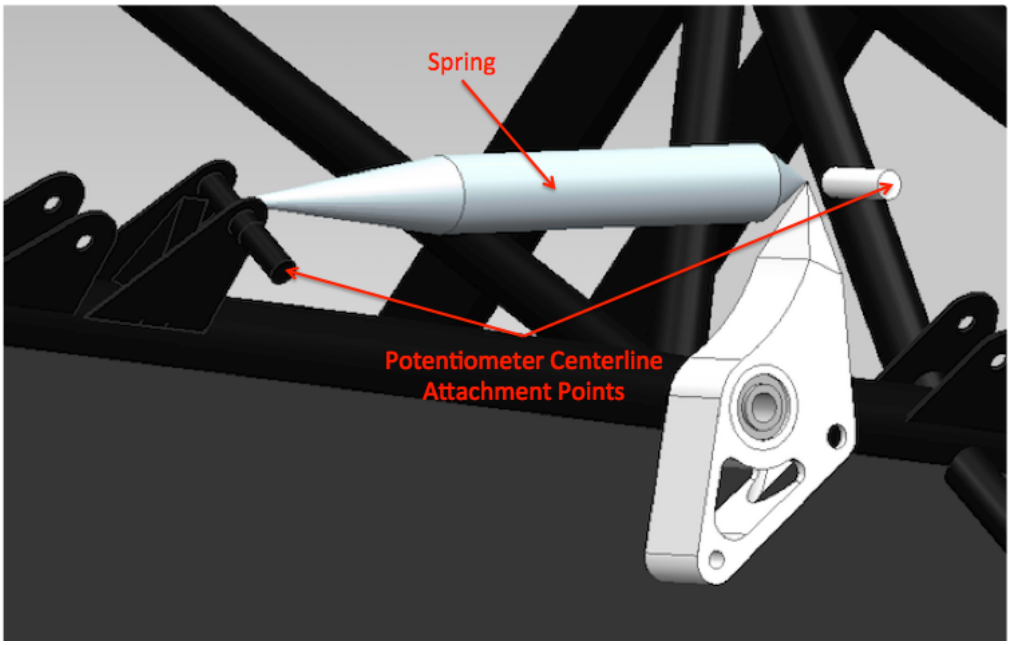

Figure 48: Spring to Potentiometer Deflection Model

Fourteen data points were collected, and the quadratic fit shown in Eq. (30) was chosen to best represent the data, where x is the sensor length and f(x) is the spring length.

$$f(x) = 0.01823x^2 + 0.7562x + 0.7621 \quad \textbf{(30)}$$

The quadratic fit is plotted with the CAD-generated data points in Figure 49, and error is plotted in Figure 50. Error due to the curve fit is negligible (~ 10^{-3} in) relative to vehicle geometric/manufacturing errors, sensor/voltmeter resolution, and overall displacement range (~ 0.25 in) during the test. The accuracy of the overall system (± 0.001 in) is limited to the resolution of the voltmeter (± 0.005 V).

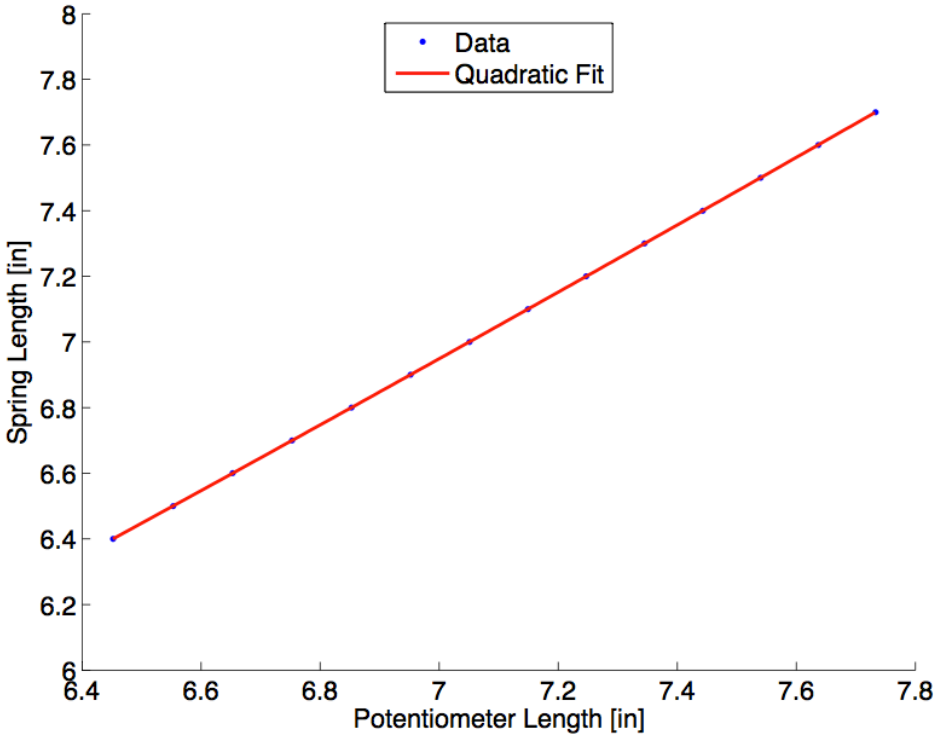

Figure 49: Spring to Potentiometer Deflection Relationship

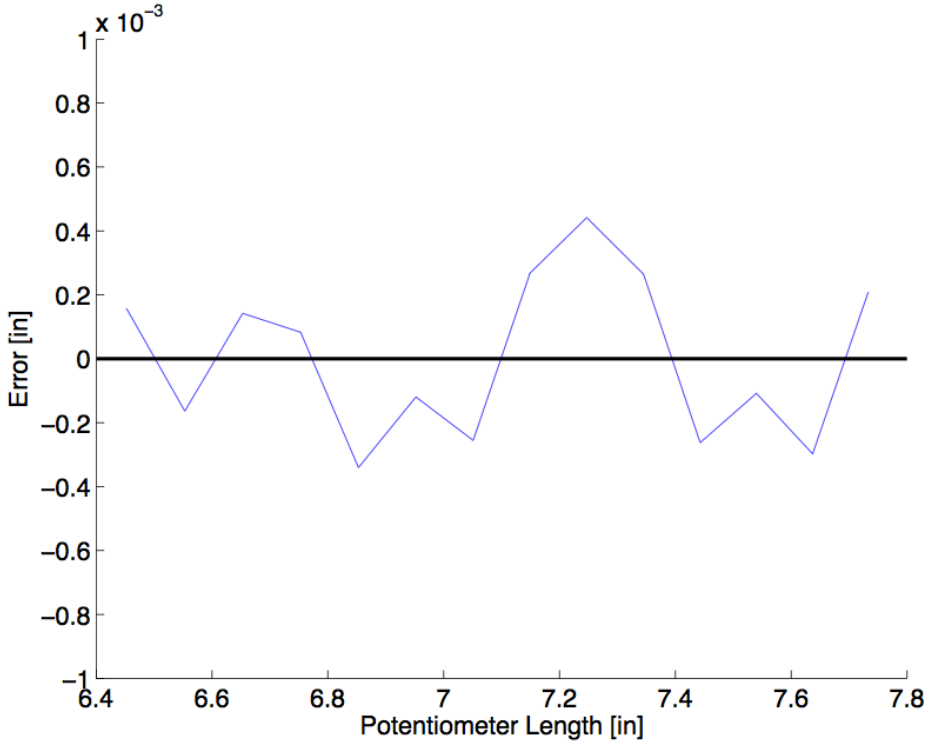

Figure 50: Spring to Potentiometer Deflection Relationship Error

Once the spring deflection is known, it can be related to the wheel center displacements using the suspension kinematics. The free end of the spring is connected to a bell crank with a motion ratio of 2.46:1. Bell crank motion displaces the pull rod that is connected to the wheel hub through the suspension corner upright. Motion of the wheel hub is constrained by the upper and lower control arms and tie rod.

6. Hoosier LC0 TiSCTeF Load-Deflection Test

This chapter describes the testing procedures and results for a load-deflection test using the TiSCTeF. A static load-deflection test is the first step in an incremental model validation process. The intent of this test is to validate the TiSCTeF design and to gain insight into the operation and use of the fixture.

This test measures the load-displacement relationship for a range of tire pressures. The tire pressures selected for testing (8, 10, 12 and 14 psi) correspond with the tire pressures selected by the TTC. The inclination angle for the front wheels is 2 degrees, as this is the standard suspension setup for this vehicle. The deflection of the right front wheel is of interest for this test, as this is the wheel located on the treadmill.

6.1. Test Procedures

After calibration of the instrumented TiSCTeF components (see Chapter 5), the fixture was assembled and the FSAE vehicle was placed on the fixture. A picture of the assembled fixture with vehicle is shown in Figure 51. Detailed instructions for installation of the treadmill and instructions for placing the vehicle on the fixture and operational guidance for the data acquisition system are provided in the *TiSCTeF Design and Operation Guide* [15].

Figure 51: Assembled Test Fixture with FSAE Vehicle

At the time of testing, an issue was identified with the purchased ball joints. Ball joints placed in compression operated as expected, however ball joints placed in tension separated under loads greater than approximately 100 lbf. As a result, the front and rear load assemblies could not be utilized to apply a normal load to the chassis. Ball joints rated for higher tensile loads could be purchased or a modification to the existing ball joints could be made to support the design loads, however neither was available at the time of testing. In order to still conduct the test, typical gym weights were brought into the lab and stacked in the driver's seat of the vehicle to increase the normal load on the tires. Figure 52 shows the vehicle with weights stacked in the driver's seat. Note that the tow straps are placed around the vehicle and attached to the crane to support the vehicle in the event of a fixture component failure.

Figure 52: Weights Added to Vehicle to Increase Normal Load

Also at the time of testing, RJ50 connectors were not available to attach to the ends of the instrument cables. Typically the connectors would be placed on the end of the cables, and the cable/connector assemblies would connect directly to the NI modules. NI 9949 RJ50 to Screw Terminal Blocks were used to facilitate the connection of the instrument cables to the NI modules for this test.

The data acquisition sample rate in LabVIEW was set to 10 Hz for the test. The LabVIEW program is intended to continuously collect data over the duration of the test. Weights were individually placed in the driver's seat, and the system was allowed to reach equilibrium for approximately 30 seconds. As previously mentioned, the linear potentiometer to measure the spring displacement was unable to be integrated into the data acquisition system at the time of testing. A manual measurement of the multi-meter voltage reading was documented along with the time at each equilibrium state.

Ten 45 lbf weights, one 35 lbf weight, and one 25 lbf weight were used for a total maximum applied normal load of 510 lbf to the sprung mass. Once all of the weights were placed in the driver's seat, the weights were individually removed while continuing to document the multi-meter voltages at each equilibrium state. At the end of the test, the LabVIEW program was stopped and the instrumentation data from the test was saved. The test was repeated for each of the selected tire pressures.

6.2. Test Results

The measured load-deflection curves for the four, tested tire inflation pressures are displayed in Figure 53. The normal load displayed is the sum of the loads in the four treadmill normal support columns. Note that the unloading data points are omitted for clarity.

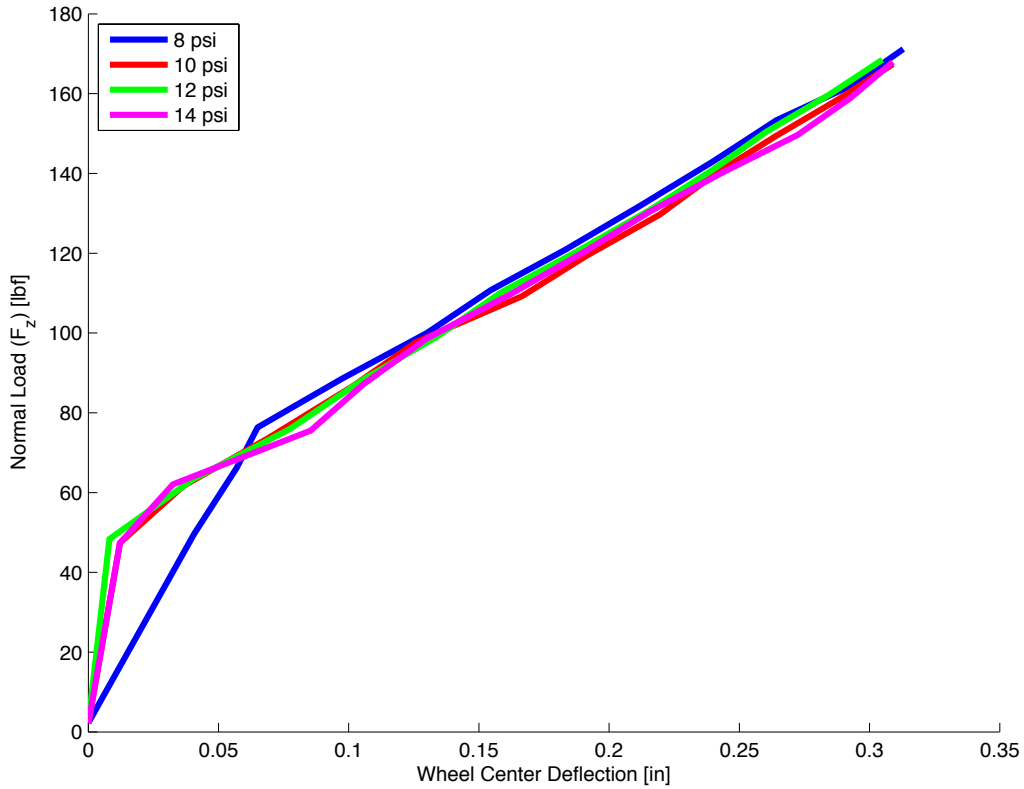

Figure 53: LC0 Load-Deflection Curves

It was expected to see a distinct stiffening of the tire and decreased wheel center deflection for increasing tire pressure curves. A distinct stiffening effect can be observed at lower normal force loads (0 - 80 lbf). A large increase in stiffness is observed between 8 and 10 psi, and a slight increase is observed between 10 and 12 psi. The 14 psi curve does not follow the expected trend.

The distinct change in slope, observed for each inflation pressure at approximately 50 lbf, was not expected. Although the load-deflection curves are not necessarily linear in nature, abrupt changes do not reflect the physical mechanics of the tire. The load measurement of

approximately 50 lbf when the vehicle is initially placed on the stand is representative of expected vehicle load, and this is consistent across all tested inflation pressures. Therefore, the magnitude of the spring deflection, which is directly related to wheel center deflection, is likely affected by an inaccuracy associated with the potentiometer. A 'sticking' effect is a common issue with this type of sensor, and the observed behavior is consistent with the potentiometer suddenly moving a large distance after a threshold load is reached.

The suspension joints, although spherical bearings, also have a finite amount of friction. This could also be contributing to the observed 'sticking' effect, and is a limitation of measuring wheel center displacement via suspension travel.

The behavior observed from 80 lbf applied load and above does not follow the expected trend of increased stiffness with increased inflation pressure. The observed curves display an inconsistent, but slightly inverse trend. The previously mentioned sticking of the potentiometer is a probable cause of this behavior.

The maximum load observed in each test was consistent, at approximately 170 lbf, indicating that the strain gage instrumentation is precise. Good confidence in strain gage accuracy can also be deduced, as the maximum expected load per corner during testing was approximately 175 lbf. The maximum loads for each test are not expected to be exactly equal, due to the car being re-placed on the fixture for each test and slight variations in the locations of the weights placed in the vehicle.

Figure 54 displays the individual loads in the treadmill normal support columns for the 10 psi inflation pressure test. The layout of the treadmill instrumentation is provided in Figure 55. Note that this figure is representative of the measured data for all pressures, and all data points are shown in this figure. The loads are slightly different in each column, but they are all within a similar range. The variation in the load levels is likely due to the wheel being placed slightly off-center on the treadmill and/or slight compliance differences in the columns. The overall curve shape similarities suggest that the applied load is distributed to and sensed in each column. The lack of anomalies in the curves gives confidence that the instrumentation is working as designed. A significant closed-loop hysteresis effect is also observed. The magnitude of the hysteresis loop was unexpected and, when considered with the results in Figure 53, the accuracy and reliability of the potentiometer again seem questionable.

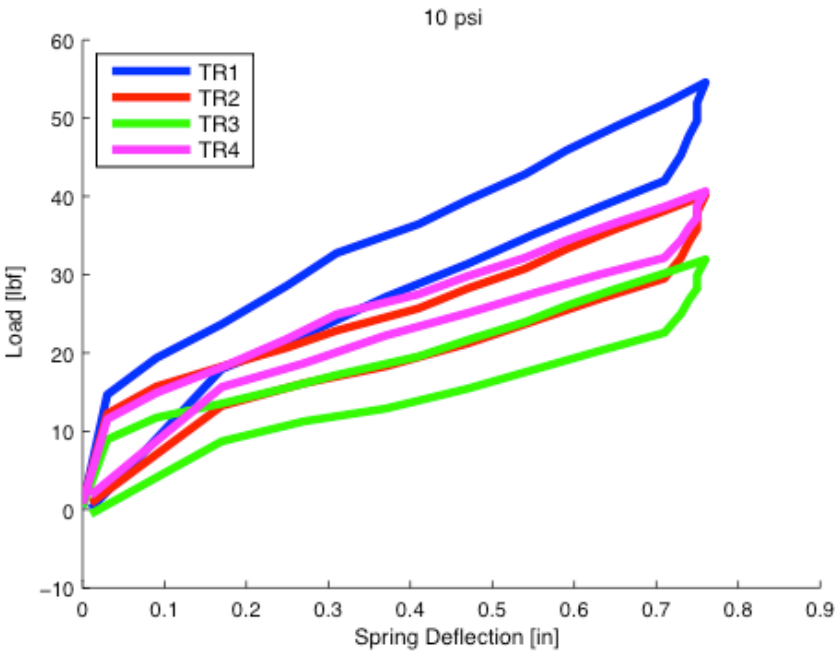

Figure 54: Treadmill Normal Support Column Loads

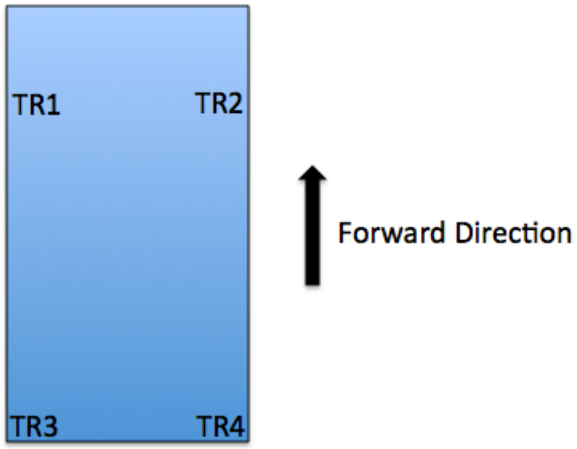

Figure 55: Treadmill Instrumentation Diagram (Overhead View)

The treadmill response as a function of applied load is given in Figure 56. The normal load displayed is the sum of the loads in the four treadmill normal support columns. Note that the unloading data points are omitted for clarity. A consistent, highly linear relationship is observed between the applied load to the vehicle and the measured load at the front right corner. The observed relationship should not vary based on inflation pressure, however slight differences in the vehicle loading and vehicle setup for each test are the cause for slight vertical shifts in the curves. The measured static vehicle loads are consistent with the known vehicle load, and the maximum measured load is consistent with 510 lbf being equally distributed across the vehicle. Good confidence in the design and instrumentation of the treadmill to produce repeatable data sets is observed.

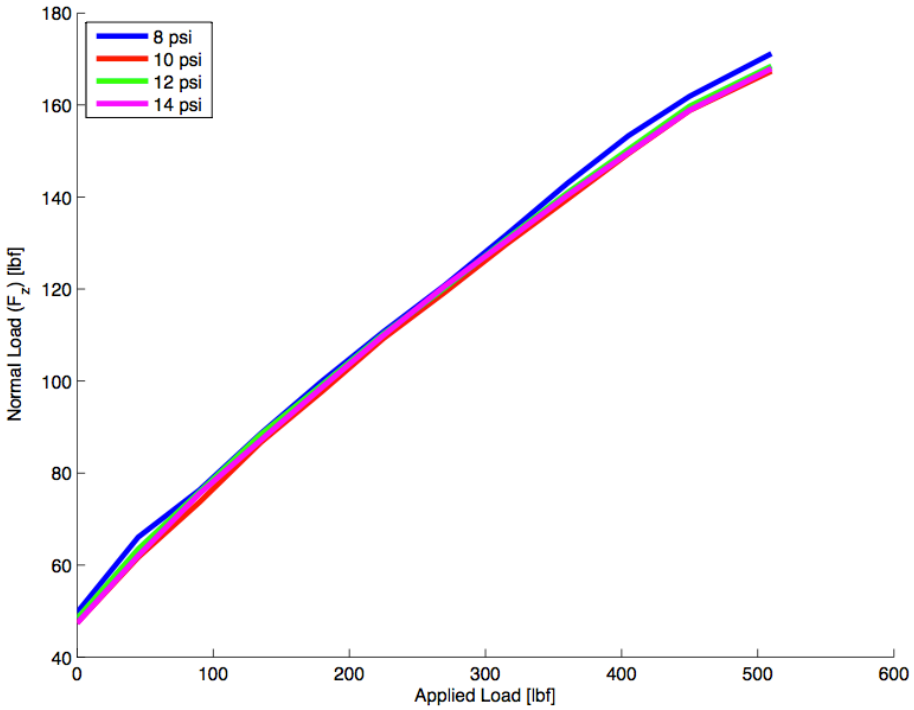

Figure 56: Treadmill Response to Applied Load

Figure 57 displays the measured normal loads at each corner during the test. The front right curve, shown in red, is the sum of the loads in the four treadmill normal support columns. Note that the unloading data points are omitted for clarity. A large variation in loads is observed across the fixture. The load-deflection relationship for the treadmill corner (front right) remained linear during the test, but the acrylic column curves deviate from linear and consistently curve upwards at increased loads.

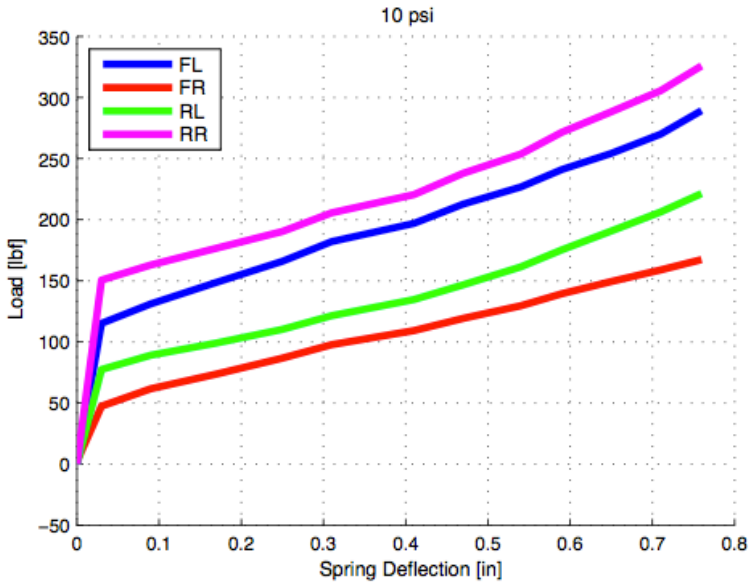

Figure 57: Fixture Normal Loads During Load-Deflection Test

The total load measured by the fixture and the expected loads are compared in Figure 58. Although some variation is expected front-to-rear since the vehicle has slightly offset static weight distribution and the weights placed in the vehicle are not centered, the difference between the total load and expected total load curves shows some significant error. As previously discussed, the magnitude of the loads measured by the treadmill for the front right corner are consistent with the applied loads, therefore the source of error is in the acrylic columns. The error is roughly constant across the range of applied loads.

A thermal expansion coefficient gradient between the strain gage and the acrylic could be affecting the acrylic column instrumentation. Although the operational procedures account for a warm-up period to achieve thermal stability, the gage resistance is constant during this time. The compressive loads applied to the column decrease the resistance in the gage and, for the same applied voltage, the current increases through the circuit. Expansion of the gage caused by heat relative to the acrylic column will create the appearance of additional strain.

Some additional calibration will be required to ensure accuracy of the acrylic columns. The load frame calibrations performed in Section 5.1 were run over a 2 - 3 minute period, whereas the tests considered in Section 6.2 were conducted over 10 - 15 minutes. The inability of the instrumentation to achieve thermal stability during the calibration would explain the observed deviations from linear behavior in the calibration. In order to better account for any thermal effects, it is suggested to place the column under multiple discrete loads and to allow the column to reach thermal stability at each load. A calibration curve can then be fitted to the discrete data points. In-situ calibration using scales or known loads may also be performed.

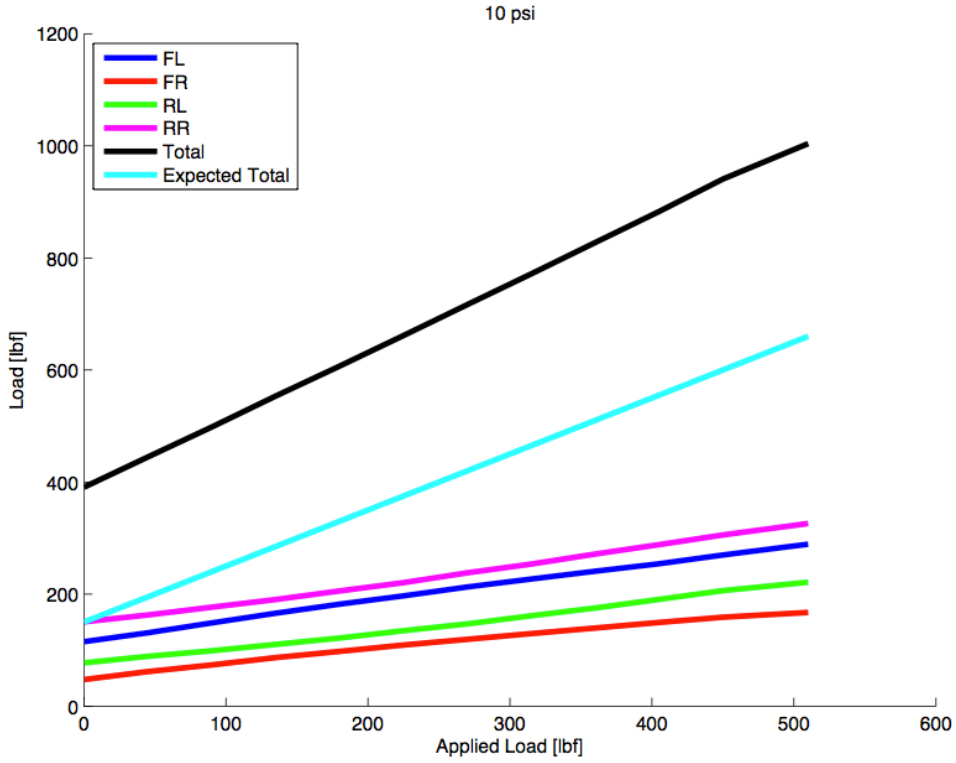

Figure 58: Observed Total Load and Expected Total Load

Despite the observed error in the acrylic column loads, appropriate load distribution across the fixture is observed. It is expected that as weights were loaded into the vehicle, that the weight distribution front-to-rear would change. This is observed by the slight upward bend in the front-left and front-right measurements and a corresponding downward bend in the rear-left and rear-right measurements.

The data presented in the section is representative for all tested inflation pressures. The complete set of data collected during the load-deflection test is available in Appendix A.

7. Conclusions and Recommendations

This section contains a brief summary of the concept solution, conclusions drawn from the observed behavior, and recommendations for improvements.

7.1. Summary

This thesis presents a concept solution and testing platform for validating the models along with supporting the development of suspension and chassis models for the Virginia Tech FSAE team. Inspiration for the concept solution comes from an 8-post shaker designed for suspension tuning, durability, and acoustic testing.

The solution concept, reproduced in Figure 59, utilizes four independent actuators to control the vertical loading of the vehicle. A basic treadmill is used as the conveyor system to roll the right-front tire. The treadmill provides a flat surface on which to roll the tire, and is capable of rolling the tire at low speeds without any modifications. The treadmill is supported by seven support columns, configured to create a kinematically stable structure. Each actuator and support column includes a gage section where strain gages are mounted to measure the axial loads. An off-the-shelf load cell design was integrated into the actuator and support column designs as a means of calibration for the strain gages. The remaining three corners of the vehicle are supported and constrained to prevent vehicle movement. Vertical (normal) loads are also measured at the untested corners for load-distribution verification purposes.

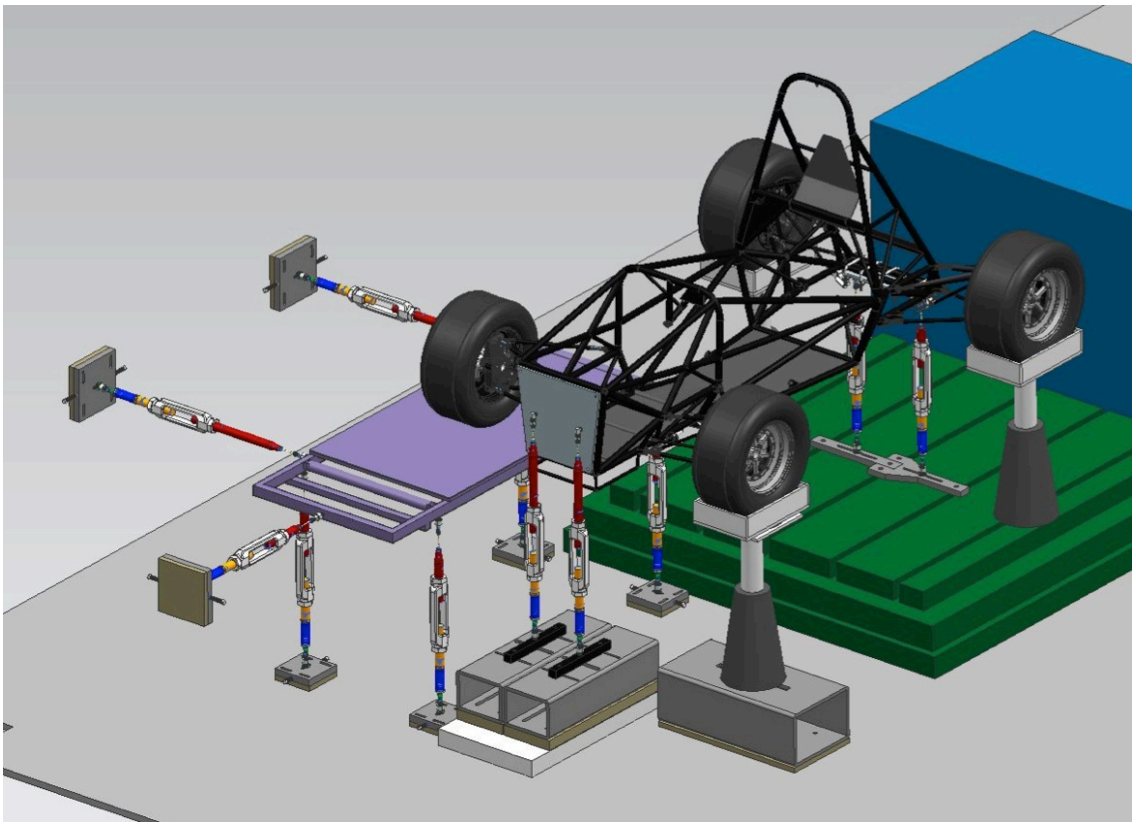

Figure 59: CAD Model of Test Fixture

The TiSCTeF is envisioned to:

- Load the tire under specific operating conditions to validate finite element models,
- Capture the relationship between wheel center loads and control arm strains,
    - Knowledge of control arm strains under specific wheel center loads will provide a basis to validate the current FSAE method for control arm and suspension component modeling.
    - This relationship will also allow for the prediction of wheel center loads by measuring control arm strains on the track. Knowledge of both the available tire load capability and the utilized capability creates the space for optimization.
- Collect cornering data for a set of representative conditions, normalize the data, and create 'master curves' for use in FSAE vehicle dynamics simulations. This would allow for the creation in-house tire data for tires not tested under the FSAE TTC,
- Roll the chassis for torsional chassis analysis.

Initial tests using the TiSCTeF indicate that, although some instrumentation upgrades and additional calibrations are required, the fixture is capable of creating reproducible data sets. These issues are considered typical in the initial shakedown of a new test fixture. Once the proper upgrades have been made to support lateral loads, the outlined process for analyzing and normalizing cornering data can be applied.

7.2. Research Conclusions and Recommendations

This section presents the conclusions of this study and specific recommendations for future work. Details are organized in reference to the Research Scope defined in Section 1.4.

7.2.1. Analyze Tire Test Consortium Data

This study analyzed the cornering data from tests performed by Calspan as part of the FSAE Tire Test Consortium. In order to normalize cornering data, first a curve fit must be made to the raw data to determine the cornering stiffness and maximum friction coefficient. A weighting method was presented to account for significant normal load variations that occurred during the tests. Weights determined by the power term in Eq. (2) (reproduced here for convenience) were incorporated into the sum of squared errors term during curve fitting. As a result, the curve fit was forced to better adhere to the data portions that exhibit the nominally correct normal load. The weighting used for this study may not be the most effective weighting for all data sets.

$$w = 10^{\frac{-\left|F_Z + F_{Z\_Nom}\right|}{\left|\max(F_Z + F_{Z\_Nom})\right|}} \quad \textbf{(2)}$$

The normalizations presented by Radt and Glemming [2] were applied to the TTC cornering data. These normalizations, if successful, collapse the data sets into sets of master curves. Decreased quality of the normalization effort was observed before applying the weighting scheme to the curve fits, however good consistency of curve collapse was observed when the weighting scheme was applied. The normalized slip and combined slip normalization methods were proved feasible for Hoosier LC0 cornering data. Distinct and consistent effects due to changes in inclination angle and pressure were observed.

These 'master curves' can be incorporated into future vehicle dynamics simulations for accurate representation of the tire behavior while maintaining efficiency of the simulation. It is suggested that future data sets collected from the TiSCTeF be analyzed, weighted for curve fitting, and normalized as shown in this study to best understand the effects of inclination angle and pressure on tire performance. The TTC data analyzed in this study will provide a baseline comparison for future cornering data collected from the TiSCTeF.

7.2.2. Create a Test Fixture to Roll the Tire

Base design, fabrication, installation, and calibration of the TiSCTeF (Tire, Suspension, and Chassis Test Fixture) were conducted as part of this study. The fixture successfully supports the FSAE vehicle and is capable of load-deflection tests and free rolling tests with no slip angle at tire speeds up to 10 mph. The treadmill system was shown to be a design capable of producing repeatable data sets.

A summary of the vehicle specifications that the fixture can accommodate (Table 2) and summary of important fixture design values (Table 10) are reproduced here for convenience.

Table 2: Test Fixture Vehicle Specifications

Feature	Adjustable Range
Front Track Width	38.2 – 57.2 in
Rear Track Width	38.6 – 52.6 in
Wheel Base	36.2 – 88.9 in
Front Bulkhead Load X Location from front wheel centers	8 – 16 in
Front Bulkhead Load Y Spacing	2.5 - 14 in
Rear Axle Load X Location from rear wheel centers	Practically unlimited
Rear Axle Load Y Spacing	2.5 – 18 in
Conveyor surface velocity	0 – 10 mph

Table 10: TiSCTeF Design Summary

Design Loads	450 lbf per corner
Number of Load Cells	1 @ 500 lbf rated
Placeholders for Additional Load Cells	10
Target Strain Level in Aluminum Gage Sections	1433 $\mu\varepsilon$
Target Strain Level in Acrylic Gage Sections	1760 $\mu\varepsilon$
Strain Gage Resistance	350 Ω
Bridge Excitation	3.3 V
No. of Strain Gage Channels	14
Total Suspension Articulation	± 1.5 in
Conveyor Speed	0 - 10 mph
Test Types	Load-Deflection, Free Rolling

At the time of publication, the following actions are identified as required modifications to the TiSCTeF to achieve full initial design functionality:

- The purchased ball joints are not able to support tensile loads above 100 lbf without excessive compliance and the possibility of complete separation. Ball joints intended for tensile loads must be replaced or modified to enable the use of the front and rear load columns. This will allow the applied load to be continuously adjustable (as opposed to applying discrete loads), provides the capability of achieving the design load of 450 lbf per corner, provides flexibility to properly distribute the normal load across the vehicle, and will support the application of a roll moment to the chassis.

- A linear potentiometer is not a sufficient means of estimating wheel center deflection for the purposes of this project. More information about the performance of the potentiometer during testing is provided in Section 7.2.3. Integrate the DIC system with the TiSCTeF to most accurately measure the wheel center deflection or surface strains for validation purposes.

The following actions are identified as upgrades to extend the functionality of the TiSCTeF:

- Fabricate a steel or steel-reinforced treadmill belt to support the lateral tire forces without buckling. The current rubber belt cannot support more than a degree or two of slip angle before severe buckling of the belt occurs. Emory cloth can be glued to the steel belt to increase the friction coefficient between the belt and the tire.

- Replace the existing motor for the treadmill for a larger motor to support higher conveyor speeds and higher loads. As the normal force on the test tire increases, the friction between the belt and belt support increases. A larger motor and/or proper gearing will ensure that the treadmill can be run at moderate speeds under high loading conditions.

- Additional support structure is required to constrain the acrylic support columns during cornering. Due to the generation of lateral forces in the tire, the car naturally wants to rotate. A stiff, collar-like structure around the acrylic tubes will prevent them from

excessive displacement, while utilizing their instrumented capability to measure axial forces.

7.2.3. Measure Load-Deflection Relationships

Testing using the TiSCTeF was limited to static load-deflection studies for this thesis. Due to the ball joint limitation described in Section 7.2.2, weights placed in the chassis were used as load for the load-deflection tests. The conducted tests represent the first step in an incremental process to obtain dynamic wheel center loads and to validate the tire finite element model with the experimental data.

It was observed that a linear potentiometer measuring spring displacement is not a sufficient means of estimating wheel center deflection for the purposes of this project. During testing, large hysteresis loops were observed for the load-displacement relationships. High confidence in the treadmill load measurements was deduced, indicating that the error is most likely due to 'sticking' of the potentiometer and potentially the suspension joints. No consistent separation of the load-deflection curves at different tire inflation pressures also indicates that the potentiometer is the source of error. Sticking is a known limitation for this type of sensor, especially during a quasi-static (not dynamic) loading scenario with small displacements. The FSAE team is currently evaluating additional types of technologies to measure spring displacements with improved quality.

The measured loads in the acrylic columns were observed to be consistently higher than expected. The inability of the instrumentation to achieve thermal stability during the calibration would explain the observed deviations from linear behavior in the calibration. In order to better account for any thermal effects, it is suggested to re-calibrate under multiple discrete loads and to allow the column to reach thermal stability at each load. It is suggested to also perform an in-situ calibration of the acrylic columns to reconcile the observed loads with the actual applied loads on the acrylic columns. Known loads or scales used by the FSAE team can be placed on top of each wheel support to create in-situ calibration curves for the acrylic supports. The purchased load cell should also be used for in-situ verification of the instrumented aluminum gage sections. This activity will also confirm that the large observed hysteresis loops in the load-deflection curves are due to the potentiometer, and not the fixture instrumentation.

It is recommended that the measured load-deflection curves only be used as reference, and that the test should be repeated using the DIC to visually measure the wheel center deflection for maximum accuracy.

References

[1] Gent, A. N., and Walter, J. D., 2006, "The Pneumatic Tire," U.S. Department of Transportation: National Highway Traffic Safety Administration, (DOT HS 810 561).

[2] Radt, H. S., and Glemming, D. A., 1993, "Normalization of Tire Force and Moment Data," Tire Science and Technology, 21(2), pp. 91-119.

[3] Gall, R., Tabaddor, F., Robbins, D., Majors, P., Sheperd, W., and Johnson, S., 1995, "Some Notes on the Finite Element Analysis of Tires," Tire Science and Technology, 23(3), pp. 175-188.

[4] Olatunbosun, O. A., and Bolarinwa, O., 2004, "FE Simulation of the Tire Design Parameters on Lateral Forces and Moments," Tire Science and Technology, 32(3), pp. 146-163.

[5] Borg, L. T., 2009, "An Approach to Using Finite Element Models to Predict Suspension Member Loads in a Formula SAE Vehicle," Masters Thesis, Virginia Tech, Blacksburg, VA.

[6] Pottinger, M. G., Marshall, K. D., and Arnold, G. A., 1976, "Effects of Test Speed and Surface Curvature on Cornering Properties of Tires," Society of Automotive Engineers, (760029).

[7] Milliken, W. F., and Milliken, D. L., 1995, "Race Car Vehicle Dynamics," Society of Automotive Engineers, Warrendale, Pa.

[8] Bakker, E., Pacejka, H. B., and Lidner, L., 1989, "A New Tire Model with an Application in Vehicle Dynamics Studies," Society of Automotive Engineers, (890087).

[9] Ojala, J. K., 2005, "Using ABAQUS in tire development process," 2005 ABAQUS Users' Conference.

[10] Nakajima, Y., 2011, "Application of Computational Mechanics to Tire Design - Yesterday, Today, Tomorrow," Tire Society and Technology, 39(4), pp. 223-244.

[11] Taheri, S., 2012, "Tire Modeling," ME 5674 Lecture, Virginia Tech, Blacksburg, VA.

[12] Moser, R. A., Sube, H. J., Turner, J. L., and Zakelj, P., 2010, "3D Digital Imaging Correlation: Applications to Tire Testing," Tire Science and Technology, 38(2), pp. 100-118.

[13] VT Motorsports, 2010, "Conceptual Design Review," FSAE Presentation, Virginia Tech, Blacksburg, VA.

[14] Kasprzak, E. M., and Gentz, D., 2006, "The Formula SAE Tire Test Consortium - Tire Testing and Data Handling," Society of Automotive Engineers, (2006-01-3606).

[15] Cauthen, R.K., 2014, "TiSCTeF Design and Operation Guide," unpublished, 1.0.

[16] 2010, “Strain Gage Selection: Criteria, Procedures, Recommendations,” Vishay Micro-Measurements, Tech Note TN-505-4.

[17] 2010, “Errors Due to Misalignment of Strain Gages,” Vishay Micro-Measurements, Tech Note TN-511.

Appendix A. Hoosier LC0 Load-Deflection Test Raw Data

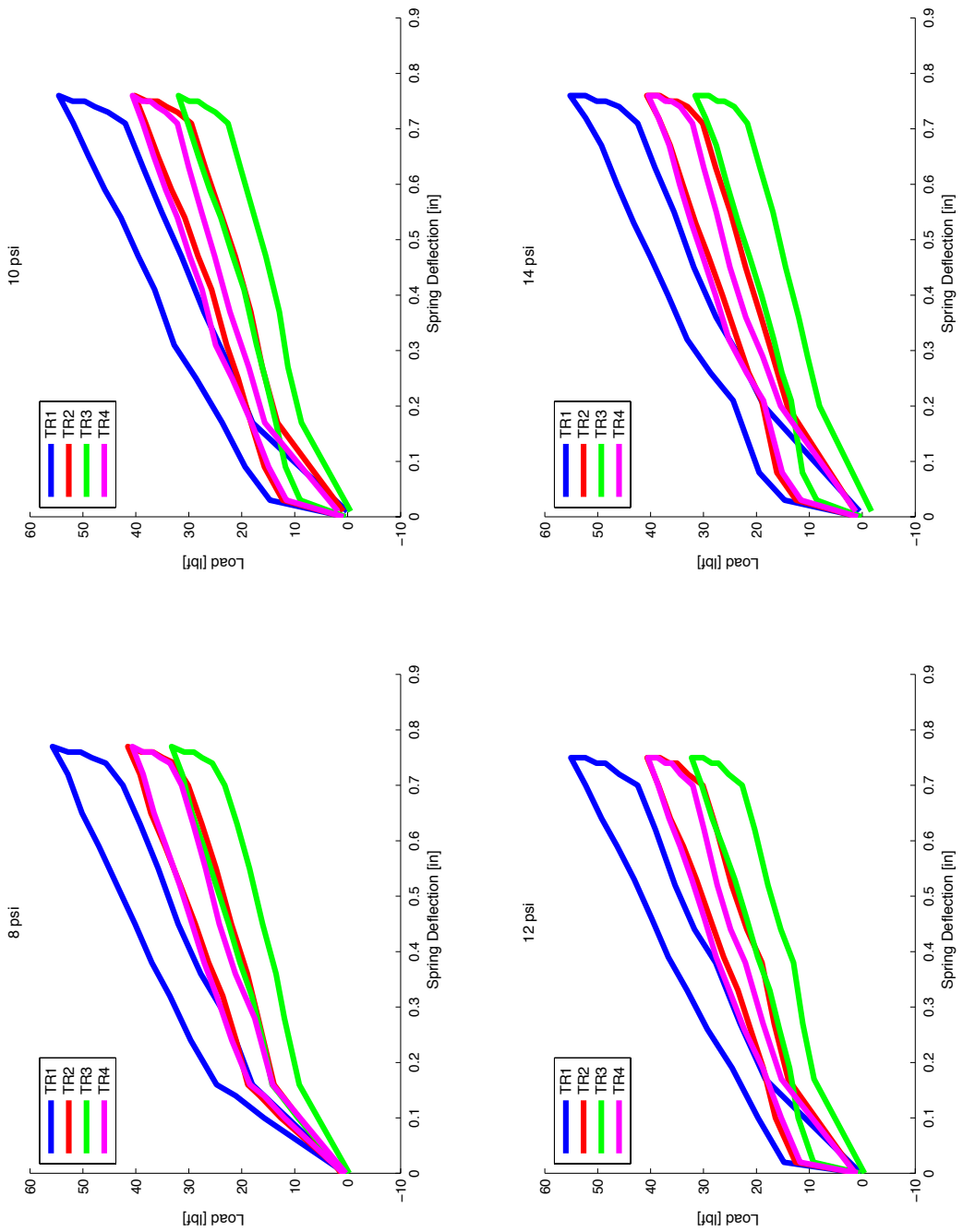

Figure 60: LC0 Load-Deflection Raw Data, Treadmill Loads

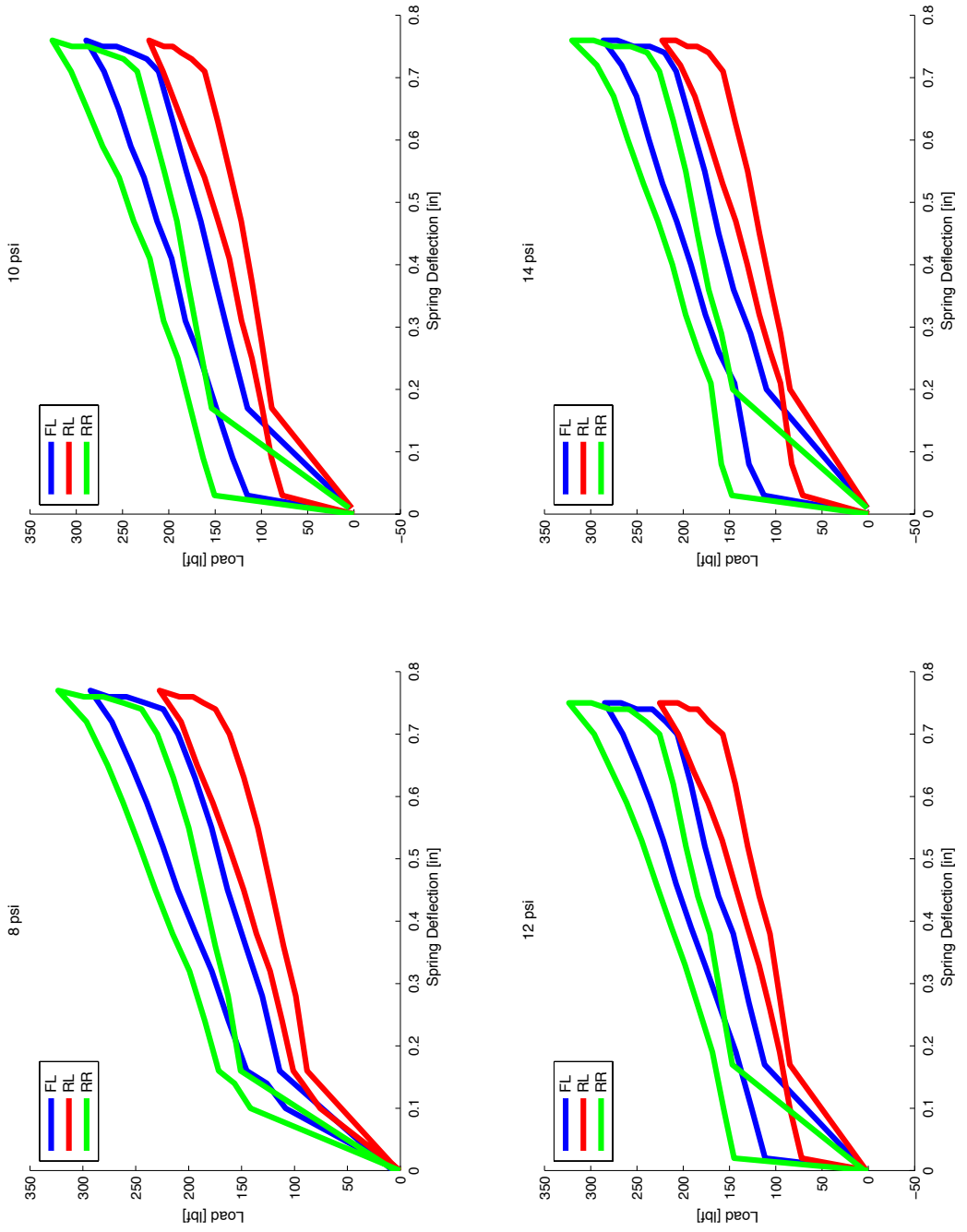

Figure 61: LC0 Load-Deflection Raw Data, Acrylic Supports

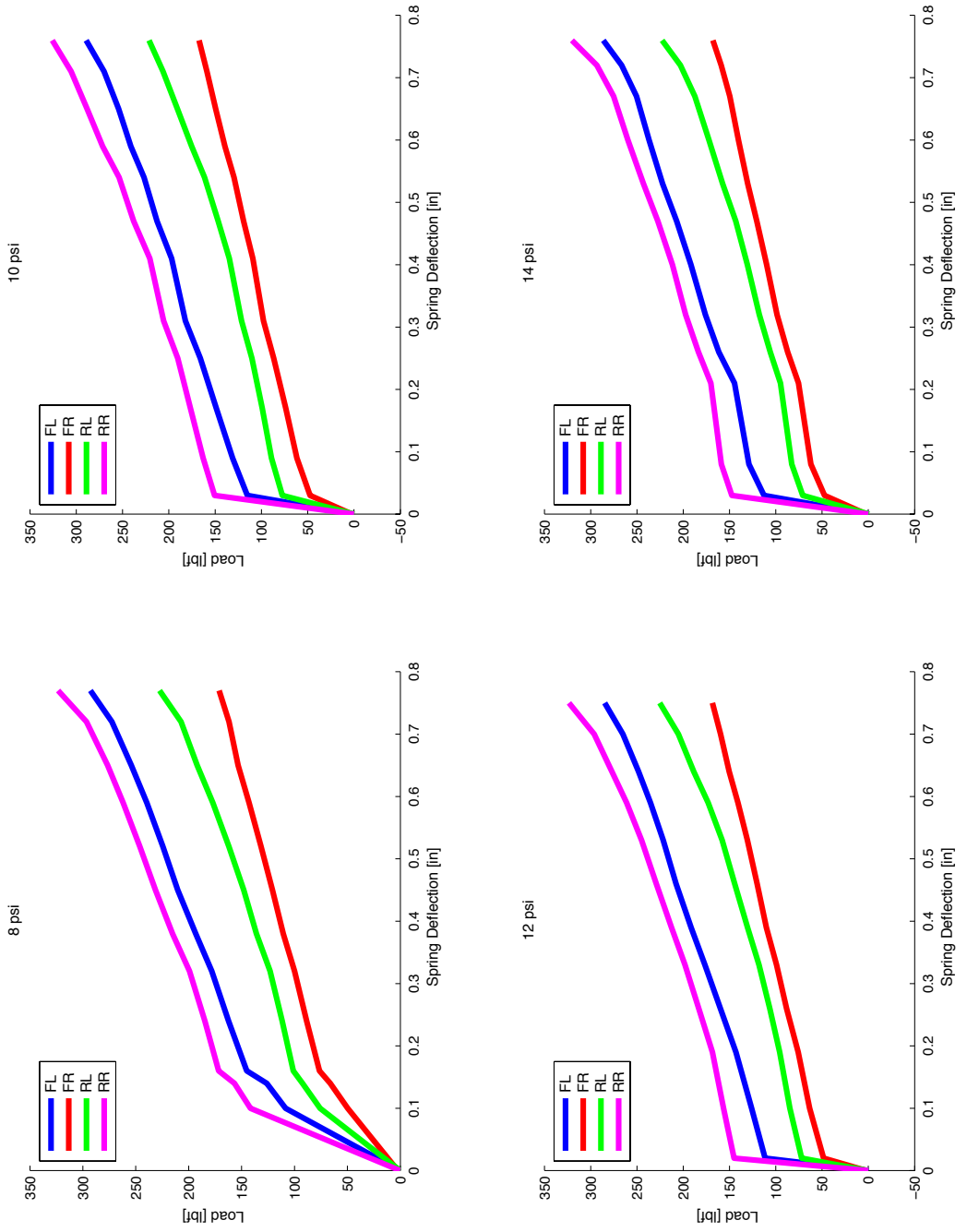

Figure 62: LC0 Load-Deflection Raw Data, Combined Treadmill Loads